The Dissertation Committee for Yong June Shin
certifies that this is the approved version of the following dissertation:

Theory and Application of Time-Frequency Analysis to Transient Phenomena in Electric Power and Other Physical Systems

Committee:

Edward J. Powers, Supervisor

William Mack Grady, Supervisor

Hao Ling

Mircea D. Driga

Kenneth H. Stokoe

Theory and Application of Time-Frequency Analysis to Transient Phenomena in Electric Power and Other Physical Systems

by

Yong June Shin, B.S.; M.S.

DISSERTATION

Presented to the Faculty of the Graduate School of

The University of Texas at Austin

in Partial Fulfillment

of the Requirements

for the Degree of

DOCTOR OF PHILOSOPHY

THE UNIVERSITY OF TEXAS AT AUSTIN

August 2004

Dedicated to my wife Kiwon Lim.

Acknowledgments

Theory and Application of Time-Frequency Analysis to Transient Phenomena in Electric Power and Other Physical Systems

Yong June Shin, Ph.D.
The University of Texas at Austin, 2004

Supervisors: Edward J. Powers
                William Mack Grady

This dissertation provides a new theoretical scheme of signal processing: cross time-frequency analysis. The proposed cross time-frequency analysis is applied to various types of real-world signals and systems in order to verify the feasibility and applicability of the proposed theory. The application of time-frequency analysis is focused on electric power and other physical systems.

Unfortunately, classical Fourier-based methodologies and power quality indices are not directly applicable for the assessment and localization of transient power quality phenomena. Hence, in this dissertation, application of time-frequency analysis is discussed for the assessment and localization of transient power quality events. Through the use of joint time and frequency localized "energy" distributions, a set of time-frequency based transient power quality indices are presented and applied to real-world disturbance signals. Also, a solution for the spatial localization of transient disturbances is presented. It rests upon calculating a time and frequency localized "phase difference" via cross time-frequency analysis. By evaluating the phase difference

of voltage and current at the time and frequency of interest and at different spatial points, one can identify the direction of transient disturbance energy flow in order to pinpoint the location of the transient disturbance source.

In addition, applications of time-frequency theory have been extended to various types of real-world physical signals and systems. A new reflectometry methodology, time-frequency domain reflectometry, is proposed and demonstrated with experimental results. Also, cross time-frequency analysis has been utilized for the characterization of ocean wave group propagation, and applied to transient postural sway signals to identify the effects of aging and sensory systems on human postural control systems.

Table of Contents

x

List of Tables

List of Figures

xvii

Chapter 1

Introduction

For the analysis of nonstationary signals, classical Fourier analysis cannot provide time-localized information of the time-varying signatures of the signals. Recent research in signal processing is focusing on the analysis of nonstationary signals and nonlinear systems, classes that most real-world physical signals and systems belong to. Time-frequency analysis started from the short time Fourier transform and the Wigner-Ville distribution in 1932, both of which have contributed to various application fields of engineering and science with aid of advances in digital computing technology. Time-frequency analysis is based on a philosophy that represents a nonstationary signal in terms of a time and frequency localized energy-like density function in a joint manner.

Time-frequency analysis has been well defined in a mathematical sense by L. Cohen via the generalization of a variety of types of time-frequency distribution in terms of kernels, which is called Cohen's class. The biggest short coming of the time-frequency distribution for the application to real-world signals involves cross terms or interference effects, which are associated with multiple signal components. W.J. Williams has contributed a great deal to the development of high resolution time-frequency kernels which overcome the limits of the interference effects including the Choi-William distribution, and the reduced interference distribution. Hence, time-frequency analysis provides a strong tool for the analysis of transient or nonstationary signals in a quanti-

tative way. Many fields of application have been investigated and interpreted with the aid of time-frequency analysis.

However, another important factor for the representation of a signal, namely, phase, cannot be treated in a proper manner via the classical definition of the time-frequency distribution. An investigation of the phase difference for an input and output signal pair will often reveal valuable information aiding the interpretation of the associated system of interest. If the input and output signal pair is transient or nonstationary, it is necessary to investigate time and frequency localized phase difference. Hence, in this dissertation, a new theory of signal processing, cross time-frequency analysis, is proposed for the determination of the time and frequency localized phase difference.

In this chapter, we briefly review the fundamental concepts on time-frequency analysis with an emphasis on its history. The spectrogram, Wigner-Ville distribution, Choi-Williams, and RID, all members of Cohen's class, will be introduced. The properties of time-frequency distributions associated with various kernels will be treated. At the end of the chapter, the structure and organization of the dissertation will be introduced.

1.1 Time-Frequency Analysis: Cohen's Class

Time-frequency analysis was motivated by the need to analyze nonstationary signals whose spectral characteristics change in time [1]. The first trial in time-frequency analysis was the short-time Fourier transform (STFT): take the Fourier transform of the nonstationary signal for a short time duration specified by a time localization window. The absolute value squared STFT is called the spectrogram. When the signal is $x(t)$, and its localization window is $h(t)$, then the definition of the spectrogram, $SP_x(t, \omega)$, is as follows [2]:

$$SP_x(t, \omega) = |S_x(t, \omega)|^2 = |\frac{1}{\sqrt{2\pi}} \int_{-\infty}^{\infty} x(\tau)h(\tau - t)e^{-j\omega\tau}d\tau|^2 \qquad (1.1)$$

However, the uncertainty principle [3] inhibits the use of the STFT, and indeed all types of time-frequency distributions. The uncertainty principle is defined by product of time resolution, Δt, and frequency resolution, $\Delta \omega$, as follows:

$$\Delta t \Delta \omega \geq \frac{1}{2} \qquad (1.2)$$

The inequality implies that the product of time resolution and frequency resolution has a lower bound: therefore we cannot achieve arbitrarily high resolution simultaneously in both time and frequency. In other words, there exists a trade-off relation between time resolution and frequency resolution. The equality holds for a Gaussian whose Fourier transform is another Gaussian.

In 1932, Wigner proposed an instantaneous auto-correlation based distribution in an application to quantum mechanics, then in 1948, Ville derived the distribution [4]. Therefore, the distribution is called the Wigner-Ville distribution. The definition of the Wigner-Ville distribution, $WV_x(t, \omega)$, is as follows:

$$WV_x(t, \omega) = \frac{1}{2\pi} \int_{-\infty}^{\infty} x_H^*(t - \frac{\tau}{2})x_H(t + \frac{\tau}{2})e^{-j\tau\omega}d\tau \qquad (1.3)$$

Strictly speaking, $x_H(t)$ in (1.3) is the analytic signal representation associated with real signal $x(t)$ as follows:

$$x_H(t) = x(t) + j\hat{x}(t) \qquad (1.4)$$

where $\hat{x}(t)$ is the Hilbert transform of the signal $x(t)$. The Hilbert transform is defined as follows:

$$\begin{aligned} \hat{x}(t) &= x(t) \otimes \frac{1}{\pi t} \\ &= \frac{1}{\pi} \int_{-\infty}^{\infty} \frac{x(\tau)}{t - \tau}d\tau \qquad (1.5) \end{aligned}$$

The purpose of the Hilbert transform and analytic signal representation is to consider positive frequency parts in the time-frequency distribution. In the remaining of this dissertation, for convenience, $x(t)$ implies the analytic signal representation of real signal via the Hilbert transform.

However, the Wigner-Ville distribution suffers from severe interference effects for multi-component signals, even though it was the first time-frequency distribution to provide localized information of signals such as the instantaneous frequency, and group delay etc.[1] The application of the Wigner-Ville distribution is quite restricted by interference effects.

Consider a signal $x(t)$ as a sum of two sinusoids,

$$x(t) = A_1 e^{j\omega_1 t} + A_2 e^{j\omega_2 t} \tag{1.6}$$

Then the Wigner-Ville distribution of the signal $x(t)$, $WV_x(t, \omega)$ is [1]

$$WV_x(t,\omega) = A_1^2 \delta(\omega - \omega_1) + A_2^2 \delta(\omega - \omega_2) + 2A_1 A_2 \delta(\omega - \frac{1}{2}(\omega_1 + \omega_2)) \cos(\omega_2 - \omega_1)t \tag{1.7}$$

Note that the last term on the RHS is an interference term that is actually does not exist in the original signal, but is produced by the interference of the two different frequencies. For more realistic signals containing many frequency components, the interference terms make it difficult to interpret the time-frequency distribution function.

In the 1990's, Choi and Williams suggested the Choi-Williams distribution [5], and Jeoung and Williams provided the reduced interference distribution (RID) [6] to mitigate the problems of interference effects. The definition of the Choi-Williams distribution, $CW_x(t, \omega : \sigma)$, is as follows:

$$CW_x(t, \omega : \sigma) = \frac{1}{4\pi^{3/2}} \int_{-\infty}^{\infty} \int_{-\infty}^{\infty} \frac{1}{\sqrt{\tau^2/\sigma}} x^*(u - \frac{\tau}{2}) x(u + \frac{\tau}{2}) e^{-\sigma(u-t)^2/\tau^2 - j\tau\omega} du d\tau \tag{1.8}$$

4

Compared with the Wigner-Ville distribution, $WV_x(t, \omega)$, we find that the Choi-Williams distribution added a Gaussian window. The objective of the Choi-Williams distribution is to suppress the interference terms in the Wigner-Ville distribution. For example, take a signal composed of two sinusoids,

$$x(t) = A_1 e^{j\omega_1 t} + A_2 e^{j\omega_2 t} \tag{1.9}$$

then, the Choi-Williams distribution of the signal is

$$CW_x(t, \omega : \sigma) = A_1^2 \delta(\omega - \omega_1) + A_2^2 \delta(\omega - \omega_2) + 2A_1 A_2 \cos[(\omega_2 - \omega_1)t]\eta(\omega, \omega_1, \omega_2, \sigma) \tag{1.10}$$

where $\eta(\omega, \omega_1, \omega_2, \sigma)$ is

$$\eta(\omega, \omega_1, \omega_2, \sigma) = \sqrt{\frac{1}{4\pi(\omega_1 - \omega_2)^2/\sigma}} \exp[-\frac{(\omega - \frac{1}{2}(\omega_1 + \omega_2))^2}{4(\omega_1 - \omega_2)^2/\sigma}] \tag{1.11}$$

We find that the interference term can be suppressed dramatically with a small value of σ, even though the interference term cannot be eliminated completely. If we take a very large value of σ, the interference term will converge to

$$\lim_{\sigma \to \infty} \eta(\omega, \omega_1, \omega_2, \sigma) = \delta(\omega - \frac{1}{2}(\omega_1 + \omega_2)) \tag{1.12}$$

Therefore, the Choi-Williams distribution converges to Wigner-Ville distribution.

Besides the Choi-Williams distribution, a variety of different types of time-frequency distributions have been suggested for various applications. L. Cohen [2] generalized various types of time-frequency distribution, $C_x(t, \omega; \phi)$ in terms of a kernel as follows:

$$C_x(t, \omega; \phi) = \frac{1}{4\pi^2} \int \int \int x^*(u - \frac{\tau}{2})x(u + \frac{\tau}{2})\phi(\theta, \tau)e^{-j\theta t - j\tau\omega + j\theta u} d\theta d\tau du \tag{1.13}$$

5

Table 1.1: Kernels of Cohen's class

Name	Kernel $\phi(\theta, \tau)$
Wigner-Ville	1
Spectrogram	$\int h^*(u - \frac{\tau}{2})h(u + \frac{\tau}{2})e^{-j\theta u}du$
Choi-Williams	$e^{-\frac{\theta^2 \tau^2}{\sigma}}$
RID	2D Symmetric Low pass filter

where $\phi(\theta, \tau)$ is the kernel of the time-frequency distribution, $x(t)$ is the signal to be analyzed, and θ and τ are frequency and time dummy variables of integration. The definition of the spectrogram in (1.1) and the Wigner-Ville distribution in (1.3) are also the member of the Cohen's class that can be expressed in terms of equation (1.13) with their own definition of kernel. Some representative examples of kernels of Cohen's class are provided in Table 1.1.

All the various trials in time-frequency distribution functions are explained within the context of Cohen's class and the definition of the kernels. By this bilinear transformation, a nonstationary time series may be expressed as a distribution function of time, frequency and kernel. The kernel of the time-frequency distribution plays an important role in the characteristics of the corresponding distribution.

Cohen's class can be expressed from another point of view, i.e., in terms of a generalized ambiguity function [1]:

$$C_x(t, \omega; \phi) = \frac{1}{2\pi} \int \int \int A_x^G(\theta, \tau)e^{-j(\omega\tau + \theta t)}d\tau d\theta \qquad (1.14)$$

where $A_x^G(\theta, \tau)$ is called a generalized ambiguity function and equals the product of the kernel and the ambiguity function $A_x(\theta, \tau)$ of the signal $x(t)$ [4]:

$$A_x^G(\theta, \tau) = \phi(\theta, \tau)A_x(\theta, \tau) \qquad (1.15)$$

where $A_x(\theta, \tau)$ is given by [7]

$$A_x(\theta, \tau) = \frac{1}{2\pi} \int x(u + \frac{\tau}{2}) x^*(u - \frac{\tau}{2}) e^{j\theta u} du \qquad (1.16)$$

In addition, the instantaneous autocorrelation is defined as follows [6]:

$$R_x(t, \tau) = x(u + \frac{\tau}{2}) x^*(u - \frac{\tau}{2}) \qquad (1.17)$$

Therefore, the phase information of the signal will be removed by the conjugation operation in the instantaneous autocorrelation in (1.17).

1.2 Reduced Interference Distribution

In this section we will discuss the reduced interference distribution proposed by Jeong and Williams [6]. The reduced interference distribution often exhibits the "best" performance compared with other distributions in terms of time-frequency resolution. In later chapters, the applications will utilize the reduced interference distribution. However, remember that even the reduced interference distribution is a member of Cohen's class.

Cohen's definition can be rewritten in terms of the instantaneous autocorrelation function as follows:

$$C_x(t, \omega; \psi) = \frac{1}{2\pi} \int_{-\infty}^{\infty} R_x^G(t, \tau) e^{-j\omega\tau} d\tau \qquad (1.18)$$

where the definition of $R_x^G(t, \tau)$ is,

$$R_x^G(t, \tau) = \frac{1}{2\pi} \int_{-\infty}^{\infty} \psi(t - t', \tau) R_x(t', \tau) dt' \qquad (1.19)$$

where $\psi(t, \tau)$ is the Fourier transform of the kernel, $\phi(\theta, \tau)$

$$\psi(t, \tau) = \int \phi(\theta, \tau) e^{-j\theta t} d\theta \qquad (1.20)$$

Jeoung and Williams suggested time-frequency distribution function in discrete domain without aliasing (AF-GDTFD: Alias-Free Generalized Discrete-Time TFD) to eliminate periodicity caused by sampling:

$$GDTFD_x(n, \omega; \psi) = \sum_m R_x^G(n, m)e^{-jm\omega} \qquad \text{for} \quad n \in Z \qquad (1.21)$$

where

$$R_x^G(n, m) = \sum_{(l,m) \in S} \psi(n - l, m)R_x(l, m) \qquad \text{for} \quad n, m \in Z \qquad (1.22)$$

and

$$S = \{(n, m) : n + \frac{m}{2} \in Z, n - \frac{m}{2} \in Z\} \qquad (1.23)$$

is the non-rectangular support of $R_x(n, m) = x(n+\frac{m}{2})x^*(n-\frac{m}{2})$, and $R_x(n, m)$ is the discrete instantaneous autocorrelation of $x(n)$ which is a sampled signal of $x(t)$.

As indicated in Table 1.1, the kernel of the reduced interference distribution is defined by a 2D lowpass filter. However, the original kernel of the reduced interference distribution was the binomial kernel as follows:

$$\psi(n, m) = \frac{1}{2^{|m|}} \sum_{k=0}^{|m|} \binom{|m|}{k} \delta(n + \frac{|m|}{2} - k) \qquad (1.24)$$

Note that the expression of Cohen's class is based on the analog integration, however, the real calculation of the time-frequency distribution is based on digital signal processing routines, especially, the FFT for digitized time series.

The reduced interference distribution is not a panacea for all the cases of nonstationary signal analysis. For example, for a chirp signal whose "single" frequency changes linearly over a wide bandwidth, the Wigner-Ville distribution will have better performance. However, the reduced interference distribution appears to be best for the analysis of multi-component signals in terms of

8

mitigating interference effects in time-frequency analysis. In addition, the reduced interference distribution shows desirable properties to extract parameter information from the time-frequency distribution. Details of such properties will be discussed in the next section in terms of the kernels.

1.3 Distribution Properties and Associated Kernel Requirements

In this section, we discuss desirable properties of the time-frequency distribution such as nonnegativity, realness, time-shift, frequency-shift, time marginal, frequency marginal, instantaneous frequency, and group delay etc. Those properties are very important information available from the time-frequency analysis. These properties are closely connected to the definitions of the kernels [2], [6]. In this section, we will discuss standard properties of time-frequency distribution which is associated with the kernel requirements. In each description of the item, "P" stands for "Property" of time-frequency distribution and "Q" stands for "Requirement" of kernel in Cohen's class.

1. **Nonnegativity**

P1. $C_x(t, \omega; \phi) \geq 0, \forall t, \omega$

Q1. $\phi(\theta, \tau)$ is the ambiguity function of some function

The nonnegativity properties are desirable for physical interpretation, however, except for the spectrogram, all of the Cohen's class definition of kernels do not strictly meet this requirement. This phenomenon comes from the interference phenomenon of multi-component signals that can produce cross negative terms in the time-frequency distribution.

2. **Realness**

9

P2. $C_x(t, \omega; \phi) \in \mathbb{R}$

Q2. $\phi(\theta, \tau) = \phi^*(-\theta, -\tau)$

The realness of the distribution is guaranteed with real and symmetric kernels, because Cohen's bilinear definition is based on the instantaneous autocorrelation function. This property is the main difference between the cross time-frequency distribution discussed in the next section.

3. Time shift

P3. $y(t) = x(t - t_0) \rightarrow C_y(t, \omega; \phi) = C_x(t - t_0, \omega; \phi)$

Q3. $\phi(\theta, \tau)$ does not depend on t

4. Frequency modulation

P4. $y(t) = x(t)e^{j\omega_0 t} \rightarrow C_y(t, \omega; \phi) = C_x(t, \omega - \omega_0; \phi)$

Q4. $\phi(\theta, \tau)$ does not depend on ω

If the kernel is independent of a signal in time variable t and frequency variable ω, the time shift and frequency shift are reflected on the time-frequency distribution.

5. Time marginal

P5. $\dfrac{1}{2\pi} \displaystyle\int C_x(t, \omega; \phi) d\omega = x(t)x^*(t)$

Q5. $\phi(\theta, 0) = 1, \forall \theta$

6. Frequency marginal

P6. $\dfrac{1}{2\pi}\displaystyle\int C_x(t,\omega;\phi)dt = X(\omega)X^*(\omega)$

Q6. $\phi(0,\tau) = 1, \forall \tau$

Time marginal and frequency marginal properties are desirable: the projection of time-frequency distribution function on the time axis generates conjugated pair product of time function, and the projection on the frequency axis generates conjugated pair product of its Fourier transform. The time and frequency marginal properties confirm the physical validity of time-frequency based analysis of transient phenomena.

Although the spectrogram, based on the short-time Fourier transform, provides useful time-frequency distributions, it does not exhibit the useful marginal properties of Cohen's class as pointed out in [2]. Consider the time marginal properties for the spectrogram. If the spectrogram satisfies the time marginal property, we have

$$\int SP_x(t,\omega)d\omega = \int |x(\tau)|^2 \cdot |h(\tau - t)|^2 d\tau = |x(t)|^2 \qquad (1.25)$$

On the other hand, if the spectrogram satisfies frequency marginal property, we have

$$\int SP_x(t,\omega)dt = \int |X(\omega')|^2 \cdot |H(\omega' - \omega)|^2 d\omega = |X(\omega)|^2 \qquad (1.26)$$

where $X(\omega)$ and $H(\omega)$ are the Fourier transform of the time domain signal $x(t)$ and window $h(t)$. One cannot find a localization window $h(\tau)$ that satisfies both (1.25) and (1.26) simultaneously [2]. Therefore, theoretically the spectrogram cannot satisfy the marginal properties [2]. This is one of the principal drawbacks of the spectogram approach.

7. Time support

11

P7. $x(t) = 0, \forall t \notin [T_1, T_2] \rightarrow C_x(t, \omega, \phi) = 0, \forall t \notin [T_1, T_2]$

Q7. $\int \phi(\theta, \tau) e^{-j\theta t} d\theta = 0 \quad \text{for} \quad |\tau| \leq 2|t|$

8. Frequency support

P8. $X(\omega) = 0, \forall \omega \notin [\Omega_1, \Omega_2] \rightarrow C_x(t, \omega, \phi) = 0, \forall \omega \notin [\Omega_1, \Omega_2]$

Q8. $\int \phi(\theta, \tau) e^{-j\tau\omega} d\tau = 0 \quad \text{for} \quad |\theta| \leq 2|\omega|$

Time and frequency support properties allow one to properly map the time series into the time and frequency domain via the bilinear transformation. The Choi-Williams distribution [5] does not satisfy the time and frequency support properties so that a "synchronization effect" is observed in the time and frequency domain when the signal elements share a time or frequency of interest.

9. Group delay

P9. $\dfrac{\int t C_x(t, \omega; \phi) dt}{\int C_x(t, \omega; \phi) dt} = -t_f(\omega)$

Q9. Q3 & Q5 and $\dfrac{\partial \phi(\theta, \tau)}{\partial \theta}\Big|_{\theta=0} = 0, \forall \tau$

10. Instantaneous frequency

P10. $\dfrac{\int \omega C_x(t, \omega; \phi) d\omega}{\int C_x(t, \omega; \phi) d\omega} = \omega_f(t)$

Q10. Q4 & Q6 and $\dfrac{\partial \phi(\theta, \tau)}{\partial \tau}\Big|_{\tau=0} = 0, \forall \theta,$

Some important quantities that can be extracted from the time-frequency distribution for wave analysis are the instantaneous frequency and group delay. The instantaneous frequency can be calculated as the normalized first

12

frequency moment of the time-frequency distribution function, and corresponds to the "average" frequency at particular time t, where each frequency is weighted by the relative amount of energy associated with that frequency.

The group delay can be calculated as the normalized first time moment of the time-frequency distribution function. Physically, the group delay means the mean arrival time of the specific frequency components. Therefore, we can estimate arrival time of a specific frequency components. The instantaneous frequency and group delay are symmetrically related as a duality. In addition, the instantaneous frequency and group delay are determined by the characteristics of the signal $x(t)$, however, for a proper measurement via the time-frequency distribution requires the corresponding conditions of the kernel. In later chapters of this dissertation the instantaneous frequency will be utilized for electric power quality assessment, and the group delay estimation will play important role in the analysis of the dispersive wave propagation.

1.4   Organization of Dissertation

There are many fields of research in engineering and science that require a quantitative analysis of transient or nonstatinoary signals. As an extension and generalization of existing theories of classical time-frequency analysis, this dissertation provides a new theoretical scheme of signal processing, cross time-frequency analysis. In addition, the proposed cross time-frequency analysis is applied to various types of real-world signals and systems in order to verify the feasibility and applicability of the proposed theory.

In Fig. 1.1, a schematic description of the structure and organization of this dissertation is provided. This dissertation is divided into theory and

13

applications of time-frequency analysis as shown in Fig. 1.1. The application of time-frequency analysis is focused on electric power and physical systems. Classical time-frequency analysis covered in Chapter 1 and cross time-frequency analysis discussed in Chapter 2 are the primary tools for the analysis of transient phenomena in this dissertation. The classical time-frequency analysis will be applied to the transient "energy" associated phenomena (Power Quality Assessment in Chapter 3, Best Wavelet Search Algorithm in Chapter 5 and Time-Frequency Domain Reflectometry in Chapter 6) and are indicated with light shading in Fig. 1.1. Cross time-frequency analysis will be applied to the transient "phase difference" associated phenomena (Transient Disturbance Localization in Chapter 4, Dispersion Analysis in Wave Propagation in Chapter 7 and Postural Control System Analysis in Chapter 8) as indicated with dark shading in Fig. 1.1. However, note that the classical time-frequency analysis and the proposed cross time-frequency analysis are complimentary to each other by dealing with time and frequency localized "energy" and "phase difference", respectively.

The first part of the application of time-frequency theory is electric power systems. In electric power systems, transient disturbance phenomena are a subject of significant research, called power quality. Power quality is a quality of service (QoS) issue for both customers and electric power service providers and it covers a variety of "transient" electromagnetic phenomena in electric power distribution systems requiring assessment, localization and detection.

Hence, classical time-frequency analysis will be utilized for the assessment of the transient power quality problems by developing new definitions of transient power quality indices in Chapter 3. The cross time-frequency analysis of Chapter 2 will be utilized for the localization of the transient capaci-
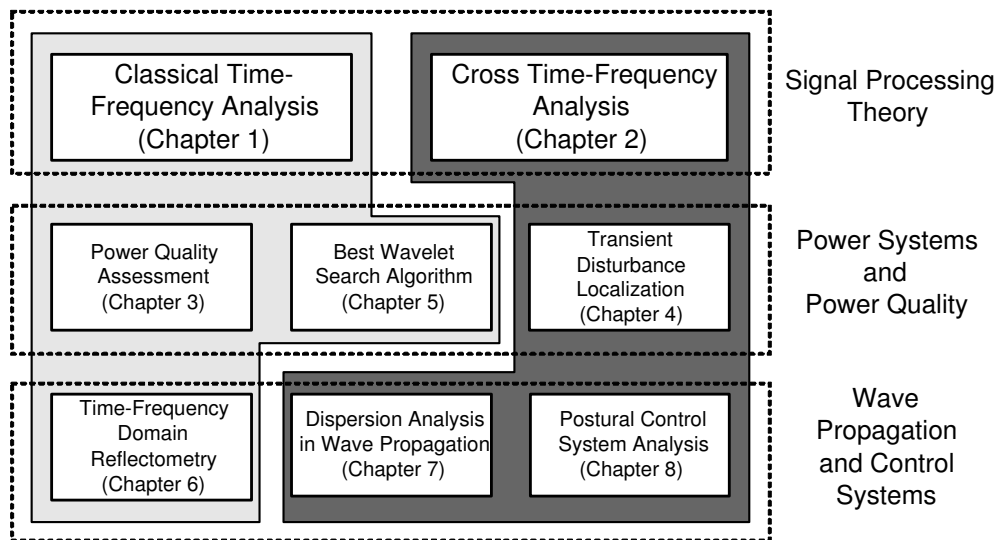
Figure 1.1: Structure and organization of dissertation

tor switching disturbance in Chapter 4. Detection of disturbances, especially voltage sags in power transmission systems, is another power system issue for which the wavelet transform is frequently employed. By exploring the time and frequency localized characteristics of signal and wavelet basis, a solution for determining the "best" wavelet basis for detection is discussed in Chapter 5.

The applications of time-frequency theory have been extended to various types of real-world physical systems by several interdisciplinary research activities. The second application of time-frequency theory is "transient" wave propagation phenomena and postural control systems. In Chapter 6, a new scheme of reflectometry, called time-frequency domain reflectometry (TFDR) is discussed. By considering time and frequency domain simultaneously, a new scheme for designing a reference signal is described. This approach appears to lead to a more sensitive detection and more accurate localization of faults on

coaxial cables.

In Chapter 7, cross time-frequency analysis has been utilized for the analysis of dispersive ocean wave propagation. In order to identify the dispersive wave propagation characteristics in ocean waves, the phase and group velocities of the wave propagation is measured via the time and frequency localized phase difference information, and the result has been confirmed by theory and compared with other approaches. In addition, in Chapter 8, cross time-frequency analysis has been applied to transient postural sway signals to identify the effects of aging and sensory systems on human postural control systems. The time and frequency localized phase difference of the postural sway signals allows one to quantitatively distinguish the contributions of aging and sensory systems using real-world experimental data sets.

Chapter 2

Theory of Cross Time-Frequency Distribution Functions

2.1 Introduction

Time-frequency analysis provides a powerful tool for the analysis of non-stationary signals. The well-defined Cohen's class generalizes various types of time-frequency distributions in terms of a kernel [1]. The main objectives of the various types of time-frequency distribution functions are to obtain a better resolution time-varying spectral density function, and to overcome interference effects [6]. However, the traditional definition of time-frequency distribution within Cohen's class [2] concerns a single signal and is based on the instantaneous autocorrelation to generate the time-varying spectrum. As a result, another critical feature of the signal, the phase, is not available in the real-valued time-frequency distribution function. This lack of phase information is also noted in some references [6], [8] as a limitation of traditional time-frequency analysis.

Using Rényi information measure of time-frequency analysis, phase difference between closely related signal components has been shown to be sensitive to the time-frequency information [9]. The need for cross time-frequency distributions has been suggested by Williams [8] via the Hilbert cross time-frequency distribution, and by Boashash [10], [11] regarding the application of cross Wigner distribution. Note that the cross time-frequency distribution

should not be confused with "*cross terms*", which are regarded as undesirable parts of the time-frequency distribution [5], [12], [13]. In this chapter, we focus on the phase difference preserving aspects of the cross time-frequency distribution function: if one can provide a joint distribution of signals, say, $x_1(t)$ and $x_2(t)$ as a function of time and frequency, one can determine the localized information of two signals for a given time and frequency. If the phase difference information between the signals can be reflected in the distribution, then the cross time-frequency distribution is very useful to deal with wave propagation and other physical phenomena dependent on phase differences. This is the motivation and objective of the cross time-frequency distribution, and the definition will be discussed in this chapter.

2.2   Motivation

To begin with, let us define a pair of complex sinusoids with different Gaussian envelopes, with different time group delays (t_1 and t_2), frequencies (ω_1 and ω_2), and phases (φ_1 and φ_2) as follows:

$$s_1(t) = (\frac{\alpha_1}{\pi})^{\frac{1}{4}} e^{-\alpha_1(t-t_1)^2/2 + j[\omega_1(t-t_1)+\varphi_1]} \tag{2.1}$$

$$s_2(t) = (\frac{\alpha_2}{\pi})^{\frac{1}{4}} e^{-\alpha_2(t-t_2)^2/2 + j[\omega_2(t-t_2)+\varphi_2]} \tag{2.2}$$

such that the means of the time and frequency of signal $x_1(t)$ are $\bar{\omega}_{x1} = \omega_1$ and $\bar{t}_{x1} = t_1$ and for $x_2(t)$, the means are $\bar{\omega}_{x2} = \omega_2$ and $\bar{t}_{x2} = t_2$ [2]. This set of testing signals will be continuously employed in this chapter to provide an example of the concepts. The time-domain representations of the signals in equation (2.1) and (2.2) and schematic plots of the time-frequency distributions for each individual signal are provided in Fig. 2.1. On each time-frequency distribution plot, the first moments in time and frequency are plotted as dashed lines.

18
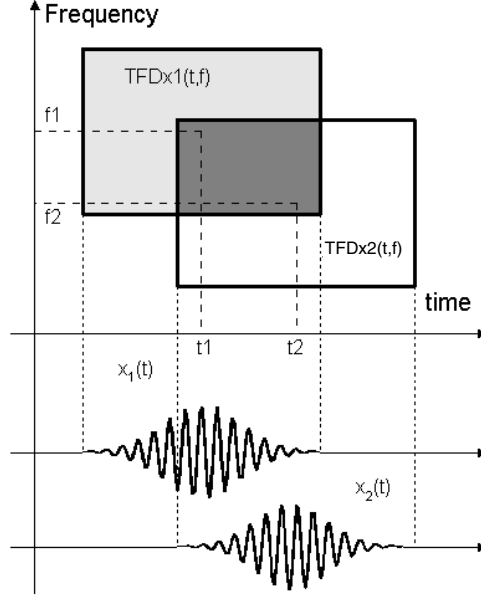
Figure 2.1: Time-frequency phase spectrum and corresponding parameters

The overlapping area of the time-frequency distributions is shaded. We choose the parameters such that the signal $x_2(t)$ is close to the signal $x_1(t)$, however, the signal $x_2(t)$ suffers some amount of time delay, and frequency shift. In addition, the two signals have different phases, φ_1 and φ_2 respectively.

How can we deal with signals, $s_1(t)$ and $s_2(t)$ in equations (2.1) and (2.2)? First of all, consider the Wigner distribution of the individual signals. With simple calculation, the Wigner distribution of each signal is as follows:

$$W_{s_1}(t,\omega) = \frac{1}{\pi}e^{-\alpha_1(t-t_1)^2-(\omega-\omega_1)^2/\alpha_1} \tag{2.3}$$

$$W_{s_2}(t,\omega) = \frac{1}{\pi}e^{-\alpha_2(t-t_2)^2-(\omega-\omega_2)^2/\alpha_2} \tag{2.4}$$

In (2.3) and (2.4), the Wigner distribution represents time-frequency distribution of the individual signals, but the phase information of the signals (φ_1,φ_2) is not reflected in the distributions in (2.3) and (2.4).

19

The motivation for cross time-frequency comes from Moyal's formula [4], [12]. Moyal's formula is defined as follows:

$$| \int x_1(t) x_2^*(t) dt |^2 = 2\pi \int \int W_{x_1}(t, \omega) W_{x_2}(t, \omega) dt d\omega \qquad (2.5)$$

where $x_1(t)$ and $x_2(t)$ are a pair of signals, and $W_{x1}(t, \omega)$ and $W_{x2}(t, \omega)$ are the corresponding Wigner distribution of signals, $x_1(t)$ and $x_2(t)$ respectively. For simplicity of calculation, let $\alpha_1 = \alpha_2 = \alpha$ for the signals in (2.1) and (2.2), and then substitute the resulting Wigner distributions into Moyal's formula [4], [12]; then we get the following result:

$$| \int s_1(t) s_2^*(t) dt |^2 = e^{-\alpha(t_1 - t_2)^2 / 2} e^{-(\omega_1 - \omega_2)^2 / 2\alpha} \qquad (2.6)$$

The corresponding amount of overlapping area is equal to the result in (2.6) and is indicated in Fig. 2.1 by the dark shading. The discrepancy of time and frequency of the pair of signals is reflected in the calculation result for the Moyal's formula, but still the phase difference information is not available. Therefore, the cross time-frequency distribution is to be featured by localized mutual information between $x_1(t)$ and $x_2(t)$ as a function of time and frequency. To describe two signals, $x_1(t)$ and $x_2(t)$, the time and frequency localized phase difference will play a key role. This is the motivation and objective of the cross time-frequency distribution, and the definition will be discussed in next section.

2.3 Definition and Derivation of Cross Time-Frequency Distribution

As Cohen's definition for time-frequency definition is based on the instantaneous autocorrelation function, the cross time-frequency starts with the

instantaneous cross correlation function. For a pair of complex analytic signals $x_1(t)$ and $x_2(t)$, we define the instantaneous cross correlation as follows:

$$R_{x_1 x_2}(t, \tau) = x_1(t + \tau/2)x_2^*(t - \tau/2) \tag{2.7}$$

In the frequency domain, if we assign $X_1(\omega)$ as a Fourier transform of $x_1(t)$ and $X_2(\omega)$ as a Fourier transform of $x_2(t)$ respectively, then the "instantaneous" spectral crosscorrelation is defined as follows:

$$R_{X_1 X_2}(\omega, \theta) = X_1(\omega + \theta/2)X_2^*(\omega - \theta/2) \tag{2.8}$$

Either $R_{x_2 x_1}(t, \tau)$ or $R_{X_2 X_1}(\omega, \theta)$ function can be transformed in terms of variables θ and τ with ambiguity functions as follows:

$$A_{x_1 x_2}(\theta, \tau) = \frac{1}{2\pi} \int R_{x_1 x_2}(t, \tau)e^{j\theta t} dt \tag{2.9}$$

$$A_{X_1 X_2}(\tau, \theta) = \frac{1}{2\pi} \int R_{X_1 X_2}(\omega, \theta)e^{j\omega\tau} d\omega \tag{2.10}$$

For the ambiguity function based on the "instantaneous" crosscorrelation function, the subscripts must be treated carefully:

$$A_{x_1 x_2}(\theta, \tau) = \frac{1}{2\pi} \int x_1(t + \tau/2)x_2^*(t - \tau/2)e^{j\theta t} dt \tag{2.11}$$

Therefore,

$$A_{x_1 x_2}(-\theta, \tau) = A_{x_2 x_1}^*(\theta, -\tau) \tag{2.12}$$

This relation also holds for the frequency domain as follows:

$$A_{X_1 X_2}(\tau, -\theta) = A_{X_2 X_1}^*(-\tau, \theta) \tag{2.13}$$

The ambiguity function in the time and frequency domain are related as follows:

$$A_{X_1 X_2}(\tau, \theta) = 2\pi A_{x_1 x_2}(-\theta, \tau) \tag{2.14}$$

21

Therefore, with a derivation in either the time domain or the frequency domain for cross time-frequency distribution, the derivation in the other domain can be derived based on the relation in (2.14).

Once the ambiguity function and instantaneous cross correlation are determined, one can employ the relation between ambiguity function, instantaneous correlation function and Wigner distribution as follows:

$$
\begin{aligned}
W_f(t, \omega) &= \int \int A_f(\theta, \tau) e^{-j(t\theta + \omega\tau)} d\theta d\tau \\
&= \frac{1}{2\pi} \int R_f(t, \tau) e^{-j\omega\tau} d\tau
\end{aligned}
\tag{2.15}
$$

where $R_f(t, \tau)$ is the instantaneous autocorrelation function, $A_f(\theta, \tau)$ is the ambiguity function of an analytic signal $f(t)$. Therefore, the cross Wigner distribution is derived as follows:

$$
\begin{aligned}
W_{x_1 x_2}(t, \omega) &= \int \int A_{x_1 x_2}(\theta, \tau) e^{-j(t\theta + \omega\tau)} d\theta d\tau \\
&= \frac{1}{2\pi} \int R_{x_1 x_2}(t, \tau) e^{-j\omega\tau} d\tau \\
&= \frac{1}{2\pi} \int x_1(t + \tau/2) x_2^*(t - \tau/2) e^{-j\omega\tau} d\tau
\end{aligned}
\tag{2.16}
$$

This definition of cross Wigner distribution corresponds to that of Boashash [10], [11] and Williams [8]. From the cross Wigner distribution, other types of generalized cross time-frequency distribution functions, $J_{x_1 x_2}(t, \omega; \Phi)$, can be obtained in terms of a kernel as follows:

$$
J_{x_1 x_2}(t, \omega; \Phi) = \frac{1}{4\pi^2} \int \int W_{x_1 x_2}(u, \xi) \Phi(t - u, \omega - \xi) du d\xi
\tag{2.17}
$$

where $\Phi(t, \omega)$ is the 2-D Fourier transform of the kernel $\phi(\theta, \tau)$. i.e.

$$
\Phi(t, \omega) = \int \int \phi(\theta, \tau) e^{-j(\theta t + \tau\omega)} d\theta d\tau
\tag{2.18}
$$

22

In other words, the following definitions of the cross time-frequency distribution are obtained:

$$
\begin{aligned}
J_{x_1 x_2}(t, \omega; \phi) &= \frac{1}{2\pi} \int \int A_{x_1 x_2}(\theta, \tau) \phi(\theta, \tau) e^{-j(\theta t + \tau \omega)} d\tau d\theta \\
&= \frac{1}{(2\pi)} \int \int \frac{1}{(2\pi)} A_{X_1 X_2}(\tau, -\theta) \phi(\theta, \tau) e^{-j(\theta t + \tau \omega)} d\tau d\theta \\
&= \frac{1}{4\pi^2} \int \int \int x_1(u + \frac{\tau}{2}) x_2^*(u - \frac{\tau}{2}) \phi(\theta, \tau) e^{-j\theta t - j\tau\omega + j\theta u} d\theta d\tau du \\
&= \frac{1}{4\pi^2} \int \int \int X_1(\nu - \frac{\theta}{2}) X_2^*(\nu + \frac{\theta}{2}) \phi(\theta, \tau) e^{-j\theta t - j\tau\omega + j\tau\nu} d\theta d\tau d\nu
\end{aligned}
$$

(2.19)

As one can see by comparing (1.13) and (2.19), the definition of the cross time-frequency distribution simply replaces the conjugated signal $x^*(t)$ in (1.13) with $x_2^*(t)$ in (2.19). In this chapter, the cross time-frequency distribution of $x_1(t)$ and $x_2(t)$ under the kernel $\phi(\theta, \tau)$ is denoted as $J_{x_1 x_2}(t, \omega; \phi)$, while the time-frequency distribution of an individual signal is denoted as $C_{x_1}(t, \omega; \phi)$, and $C_{x_2}(t, \omega; \phi)$, respectively. To facilitate comparison with Cohen's class of distributions, the definitions of the kernels is the same as Cohen's family. Therefore, changing the kernel of the cross time-frequency distribution in (2.19) will generate many types of cross time-frequency distribution functions: cross Wigner distribution, cross Choi-Williams distribution, cross RID etc. Instead of investigating many individual cross time-frequency distributions with various kernels, we investigate the properties and corresponding kernel requirements for cross time-frequency distribution functions.

23

Table 2.1: Properties of cross time-frequency distribution and associated kernel requirements

Complex	P1	$J_{x_1x_2}(t,\omega;\phi) \in C$, and $J_{x_1x_2}(t,\omega;\phi) = J^*_{x_2x_1}(t,\omega;\phi)$
distribution	Q1	$\phi(\theta,\tau) = \phi^*(-\theta,-\tau)$
time	P2	If $x_a(t) = x_1(t-t_0)$, and $x_b(t) = x_2(t-t_0)$
domain		Then $J_{x_ax_b}(t,\omega;\phi)=J_{x_1x_2}(t-t_0,\omega;\phi)$
shift	Q2	$\phi(\theta,\tau)$ does not depend on t
frequency	P3	If $x_a(t) = e^{j\omega_0 t}x_1(t)$, and $x_b(t) = e^{j\omega_0 t}x_2(t)$
domain		Then $J_{x_ax_b}(t,\omega;\phi)=J_{x_1x_2}(t,\omega-\omega_0;\phi)$
shift	Q3	$\phi(\theta,\tau)$ does not depend on ω
time	P4	$\dfrac{1}{2\pi}\displaystyle\int J_{x_1x_2}(t,\omega;\phi)d\omega = x_1(t)x_2^*(t)$
marginal	Q4	$\phi(\theta,0) = 1, \forall\theta$
frequency	P5	$\displaystyle\int J_{x_2x_1}(t,\omega;\phi)dt = X_1(\omega)X_2^*(\omega)$
marginal	Q5	$\phi(0,\tau) = 1, \forall\tau$
joint frequency	P6	$Re\{\dfrac{\displaystyle\int \omega J_{x_1x_2}(t,\omega;\phi)d\omega}{\displaystyle\int J_{x_1x_2}(t,\omega;\phi)d\omega}\} = \omega_{x_1x_2}(t)$
moment	Q6	Q4 and $\frac{\partial\phi(\theta,\tau)}{\partial\tau}\vert_{\tau=0} = 0, \forall\theta$
joint time	P7	$Re\{\dfrac{\displaystyle\int t J_{x_1x_2}(t,\omega;\phi)dt}{\displaystyle\int J_{x_1x_2}(t,\omega;\phi)dt}\} = -t_{x_1x_2}(\omega)$
moment	Q7	Q5 and $\frac{\partial\phi(\theta,\tau)}{\partial\theta}\vert_{\theta=0} = 0, \forall\tau$
Moyal's	P8	$\vert\displaystyle\int\int J_{x_1x_2}(t,\omega;\phi)dtd\omega\vert^2$ $= (2\pi)^2\displaystyle\int\int \widetilde{C_{x_1}}(t,\omega;\phi)\widetilde{C_{x_2}}(t,\omega;\phi)dtd\omega$
formula	Q8	$\phi(\theta,\tau) \neq 0, \forall\tau,\theta$
Time-Frequency	P9	$\Theta_{x_1x_2}(t,\omega;\phi) = \tan^{-1}[\dfrac{\text{Im}(J_{x_1x_2}(t,\omega;\phi)}{\text{Re}(J_{x_1x_2}(t,\omega;\phi)}]$
phase spectrum	Q9	Q1-Q8

2.4 Properties of Cross Time-Frequency Distribution

2.4.1 Properties of Cross Time-Frequency Distribution

The properties of various types of time-frequency distribution in Cohen's class are determined by the kernels. This is also the case for the cross time-frequency distribution. Some desirable properties and corresponding kernel requirements [12] for time-frequency distribution are suggested for the design of the reduced interference distribution [6], [14]. Corresponding desirable properties (P) and kernel requirements (Q) for the cross time-frequency distribution are summarized in Table 2.1. P2-P9, and Q2-Q9, are close or easy to follow to those of Cohen's class. P1 (Complex distribution), P10 (Moyal's formula), and P11 (Time-frequency phase spectrum) are notable exceptions for the cross time-frequency distributions.

The kernel requirements Q1 determines the conjugate relation between $J_{x_1 x_2}(t, \omega; \phi)$ and $J_{x_2 x_1}(t, \omega; \phi)$ such that $J_{x_1 x_2}(t, \omega; \phi) = J_{x_2 x_1}^*(t, \omega; \phi)$, while the reality of the classical time-frequency distribution is determined by the same condition, Q1. Time and frequency shift properties (P2, P3) are hold time t and frequency ω independence of the kernel (Q2, Q3). The kernel requirements for the marginal properties (Q4, Q5) are the same as the classical time-frequency distribution, however, the proper marginal of the cross time-frequency yields a product of signal and conjugation of reference signal in the time domain (P4) or product of spectrum and conjugation of the reference spectrum in the frequency domain (P5). Because the cross time-frequency distribution is a time-frequency localized *mutual* information of the signals, the normalized time and frequency moments are obtained by a joint moment (P6, P7). A detailed discussion of the joint time and frequency moments will be presented in the next subsection. As we are dealing with two different sig-

25

nals, strong finite support for time and frequency (P8, P9) is more reasonable than weak support. The proof of the strong support and corresponding kernel requirements (Q8, Q9) are directly applicable to the definition of the cross time-frequency distribution [15].

Based on the cross time-frequency distribution function, the expression for Moyal's formula can be generalized. Using the marginal properties of cross time-frequency distribution (P4,P5), alternative expressions for Moyal's formula can be obtained by the following sequence: the left side of Moyal's equation (2.5) can be modified in terms of the cross time-frequency distribution function, $J_{x_1 x_2}(t, \omega; \phi)$,

$$
\begin{aligned}
| \int x_1(t) x_2^*(t) dt |^2 &= | \int \{ \frac{1}{2\pi} \int J_{x_1 x_2}(t, \omega; \phi) d\omega \} dt |^2 \\
&= \frac{1}{4\pi^2} | \int \int J_{x_1 x_2}(t, \omega; \phi) dt d\omega |^2
\end{aligned}
$$

(2.20)

Note that this relation holds only for the kernels that satisfy the requirements for time marginal property (P4). Then the right hand side of Moyal's formula (2.5), the product of Wigner distributions can be transformed to the other types of distribution function by manipulation of the moment functions [16]

$$
\int \int W_{x_1}(t, \omega) W_{x_2}(t, \omega) dt d\omega = \int \int \widetilde{C_{x_1}}(t, \omega; \phi) \widetilde{C_{x_2}}(t, \omega; \phi) dt d\omega \qquad (2.21)
$$

where $\widetilde{C_{x_1}}(t, \omega; \phi)$ and $\widetilde{C_{x_2}}(t, \omega; \phi)$ are the transforms of the Wigner distributions $W_{x_1}(t, \omega)$ and $W_{x_2}(t, \omega)$ into the Cohen's class distribution with corresponding kernel $\phi(\theta, \tau)$. In other words,

$$
W_{x_1}(t, \omega) = \int \int g(t' - t, \omega' - \omega) C_{x_1}(t', \omega') dt' d\omega' = \widetilde{C_{x_1}}(t, \omega; \phi) \qquad (2.22)
$$

where

$$
g(t, \omega) = \frac{1}{4\pi^2} \int \int \frac{1}{\phi(\theta, \tau)} e^{j\theta t + j\tau\omega} d\theta d\tau \qquad (2.23)
$$

26

Therefore, we can obtain an alternative expression for Moyal's formula as follows:

$$|\int\int J_{x_1x_2}(t,\omega;\phi)dtd\omega|^2 = (2\pi)^2\int\int \widetilde{C_{x_1}}(t,\omega;\phi)\widetilde{C_{x_2}}(t,\omega;\phi)dtd\omega \quad (2.24)$$

Equation (2.24) shows the relation between the cross time-frequency distribution function and Cohen's class distribution function. In addition, we can clarify the meaning of the cross time-frequency distribution : the cross time-frequency distribution contains the mutual time-frequency information of the signals where the time-frequency distribution is overlapped. The phase information is included in the cross time-frequency distribution function, which is not available from the classical version of Cohen's class due to the conjugation operation.

The cross time-frequency distribution is a complex distribution and, thus, provides phase difference information. To obtain the phase difference information between two signals, it is recommended that the time-frequency kernel satisfy the kernel requirements Q1-Q10. In general, a cross time-frequency distribution can be rewritten in following polar format:

$$J_{x_1x_2}(t,\omega;\phi) = |J_{x_1x_2}(t,\omega;\phi)|e^{j\Theta_{x_1x_2}(t,\omega;\phi)} \quad (2.25)$$

where $\Theta_{x_1x_2}(t,\omega;\phi)$ is the phase difference spectrum of the signal x_1 and x_2.

$$\Theta_{x_1x_2}(t,\omega;\phi) = \tan^{-1}[\frac{\text{Im}(J_{x_1x_2}(t,\omega;\phi))}{\text{Re}(J_{x_1x_2}(t,\omega;\phi))}] \quad (2.26)$$

Therefore, the cross time-frequency distribution reveals the phase difference between two signals as a function of time and frequency. Reflecting on the properties and corresponding kernel requirements in Table 2.1, the Wigner and RID kernels are good candidates to obtain reasonable time-frequency phase

27

difference spectra, because, the desirable kernel requirements in Table 2.1, and characteristics of various kernels in [6], indicate that the Wigner and RID kernels satisfy all the kernel requirements for proper cross time-frequency distribution function. Detailed utilization of the time-frequency phase spectrum with choice of kernels will be treated in the next section along with a numerical example.

2.4.2 Gabor Logon Example of the Cross Time-Frequency Distribution

The individual properties in Table 2.1 are defined in terms of the kernel, and we will provide examples of the corresponding properties with the pair of signal sets in (2.1) and (2.2). Applying $\alpha_1 = \alpha_2 = \alpha$ to (2.1) and (2.2) for simplicity, we have,

$$s_1(t) = (\frac{\alpha}{\pi})^{\frac{1}{4}} e^{-\alpha(t-t_1)^2/2 + j[\omega_1(t-t_1)+\varphi_1]} \tag{2.27}$$

$$s_2(t) = (\frac{\alpha}{\pi})^{\frac{1}{4}} e^{-\alpha(t-t_2)^2/2 + j[\omega_2(t-t_2)+\varphi_2]} \tag{2.28}$$

To further simplify the expression, we arrange the variables of time delay and frequency shift as follows:

$$\begin{aligned} t_0 &= (t_1 + t_2)/2, & t_2 - t_1 &= \Delta t \\ \omega_0 &= (\omega_1 + \omega_2)/2, & \omega_2 - \omega_1 &= \Delta \omega \end{aligned} \tag{2.29}$$

Concerning the signal sets $s_1(t)$ and $s_2(t)$ in (2.27) and (2.28), the cross time-frequency distribution is calculated as follows:

$$\begin{aligned} J_{s_1 s_2}(t, \omega; \phi(\theta, \tau) = 1) &= \frac{1}{2\pi} \int s_1(t + \tau/2) s_2^*(t - \tau/2) e^{-j\omega\tau} d\tau \\ &= e^{-\alpha(t-t_0)^2 - (\omega-\omega_0)^2/\alpha} \cdot \\ &\quad e^{j[\Delta t(\omega-\omega_0) - \Delta\omega(t-t_0) + (\varphi_1 - \varphi_2)]} \end{aligned} \tag{2.30}$$

28
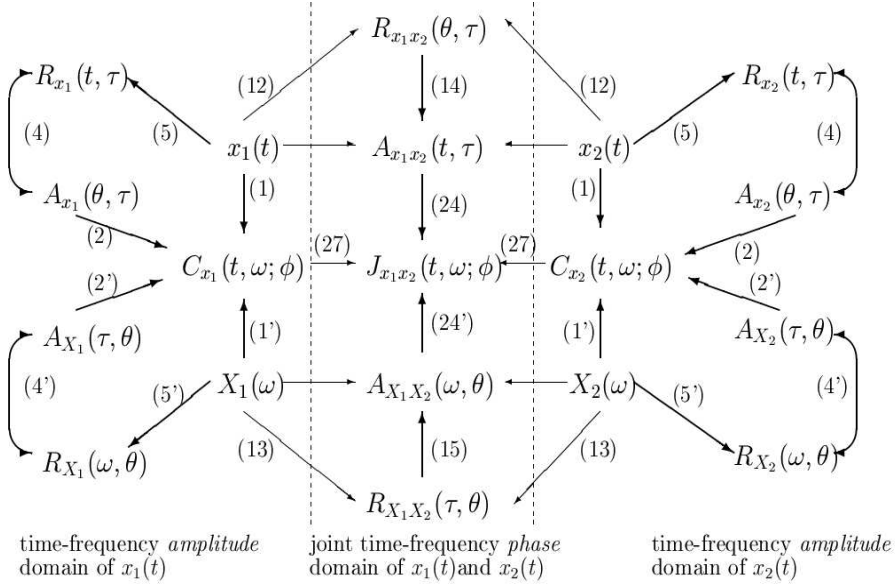
Figure 2.2: Relation between cross time-frequency distribution and Cohen's class (Numbers in the braces of the diagram correspond to the reference numbers of equation in this chapter.)

In the envelope part of the distribution, the joint distribution of signal $x_1(t)$ and $x_2(t)$ is provided. The phase part of the distribution is a function of the time deviation (Δt), frequency deviation $(\Delta \omega)$, and phase difference $(\varphi_1 - \varphi_2)$ between the signals.

Using the time and frequency domain marginal properties, we consider the joint frequency moment at t_0,

$$\frac{\int \omega J_{s_1 s_2}(t, \omega; \phi(\theta, \tau) = 1) d\omega}{\int J_{s_1 s_2}(t, \omega; \phi(\theta, \tau) = 1) d\omega}\Big|_{t=t_0} = \omega_0 + j\frac{\alpha \Delta t}{2} \qquad (2.31)$$
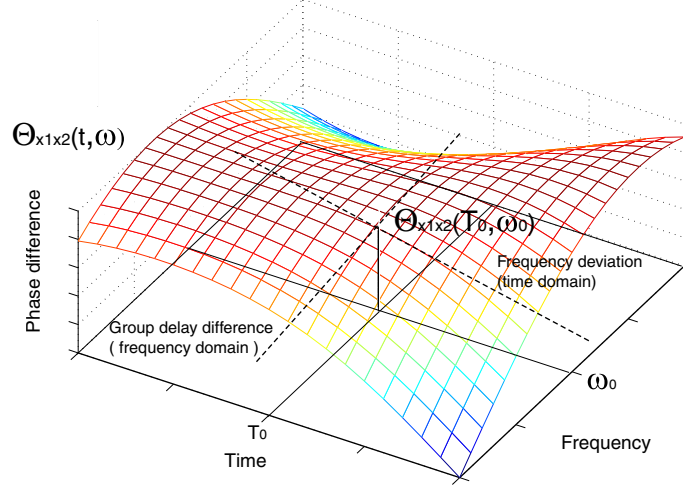
Figure 2.3: Time-frequency phase spectrum and corresponding parameters

Similarly, the joint time moment at ω_0 is,

$$\frac{\int t J_{s_1 s_2}(t, \omega; \phi(\theta, \tau) = 1) d\omega}{\int J_{s_1 s_2}(t, \omega; \phi(\theta, \tau) = 1) d\omega}\Big|_{\omega=\omega_0} = t_0 - j\frac{\Delta\omega}{2\alpha} \qquad (2.32)$$

If we take the real part of the normalized first moment in the time and frequency domain, we can obtain the mean of the instantaneous frequency and mean of the group delay for the signals. This is a unique feature of the cross time-frequency distribution function, because, one can estimate mutual information of two different signals.

In Fig. 2.3, a conceptual time-frequency phase spectrum $\Theta_{x_1 x_2}(t, \omega)$ is plotted. At the time and frequency of interest (t_0, ω_0), the corresponding phase difference can be estimated from the phase spectrum. Besides the phase difference, the partial derivatives of time and frequency variables includes transient

30

frequency deviation and group delay at (t_0, ω_0).

Consider the time-frequency phase spectrum of $s_1(t)$ and $s_2(t)$. Using the definition of the time-frequency phase spectrum and the cross time-frequency distribution, we have

$$\Theta_{s_1 s_2}(t, \omega; \phi = 1) = \Delta t(\omega - \omega_0) - \Delta \omega(t - t_0) + (\varphi_1 - \varphi_2) \qquad (2.33)$$

At (t_0, ω_0), the exact phase difference $\varphi_1 - \varphi_2$ is obtained from the time-frequency phase spectrum. Besides, at $t = t_0$, the slope in frequency domain corresponds to the group delay, Δt, as indicated in Fig. 2.3 such that

$$\Theta_{s_1 s_2}(t = t_0, \omega; \phi = 1) = \Delta t(\omega - \omega_0) + (\varphi_1 - \varphi_2) \qquad (2.34)$$

Similarly, at $\omega = \omega_0$, the slope in time domain corresponds to the frequency deviation between the signals such that

$$\Theta_{s_1 s_2}(t, \omega; \phi = 1) = -\Delta \omega(t - t_0) + (\varphi_1 - \varphi_2) \qquad (2.35)$$

From the time-frequency phase spectrum, one can provide time-frequency dependent phase difference information for two signals. The information is delivered by phase $(\varphi_1 - \varphi_2)$, group delay (Δt), and frequency difference $(\Delta \omega)$.

2.4.3 Relation between Cohen's Class and Cross Time-Frequency Analysis

We have discussed the cross time-frequency distribution and its properties. Next we need to summarize the cross time-frequency and establish the relation between cross time-frequency and Cohen's class. Fig. 2.2 shows the relation between Cohen's class definition of signal $x_1(t)$ and $x_2(t)$ and its cross time-frequency distribution $J_{x_1 x_2}(t, \omega; \phi)$. The upper part of the diagram is

31

for the time-domain, while the lower part of the diagram is for the frequency-domain. Individual terms are connected to related terms. The number beside the arrow indicates the corresponding transform equation numbers provided in this chapter.

The left and right hand side outside the dashed line indicates Cohen's class domain for individual signals $x_1(t)$ and $x_2(t)$, respectively. Each item in Fig. 2.2 is related to corresponding items via arrows where the relations are indicated by the equation numbers provided in this chapter. The prime of a number indicates an inverse relation not provided in this chapter, but can be obtained by the inverse transformation of corresponding numbered relations. As shown in Fig. 2.2, the derivation of the cross time-frequency distribution is close to that of the Cohen's class time-frequency distribution functions in terms of time/frequency correlation and time/frequency ambiguity functions. However, note that while time, frequency-varying *"amplitude"* of individual signals is treated in Cohen's domain, time, frequency-varying *"phase difference"* between two signals is treated in the cross time-frequency domain in terms of complex distribution $J_{x_1 x_2}(t, \omega; \phi)$. Between Cohen's class distribution functions $C_{x_1}(t, \omega; \phi)$ and $C_{x_2}(t, \omega; \phi)$ are connected to the cross time-frequency distribution function $J_{x_1 x_2}(t, \omega; \phi)$ via Moyal's formula. Based on the definition of the cross time-frequency distribution, Moyal's formula can be interpreted as a deterministic correlation function for a pair of nonstationary signals that measures the closeness of signals in the time-frequency plane. The cross time-frequency distribution allows one to determine a phase difference in time and frequency for two different signals whose individual phases are not available in Cohen's class time-frequency distributions.

2.5 Numerical Example

When dealing with cross time-frequency distributions, one will face the following fundamental questions: 1) How is the phase difference information via cross time-frequency distribution different from classical Fourier-based cross power spectrum? 2) How does the choice of kernel effect the estimate of a time-frequency phase spectrum? It is clear that classical Fourier analysis cannot provide time resolution, while the cross time-frequency provides time and frequency dependent phase information. It is important to identify the pros and cons of time-frequency localized phase difference information. In addition, we have provided time-frequency kernel requirements in Table 2.1, however, most of the explanation in previous sections actually deals with the cross Wigner distribution due to the simplicity of calculation. In this section, we will consider a numerical example in order to compare classical Fourier analysis and cross time-frequency analysis. In addition, the results are compared with different kernels, i.e. Wigner and binomial reduced interference distribution kernels to demonstrate the validity of the kernel requirements in Table 2.1. Consider the following numerical example,

$$x(t) = e^{-(t-2.45)^2/1+j[2\pi(10+0.3)(t-2.45)]} + n_1(t) \tag{2.36}$$

$$y(t) = e^{-(t-2.55)^2+j[2\pi(10-0.3)(t-2.55)-1.0]} + n_2(t) \tag{2.37}$$

where $n_1(t)$ and $n_2(t)$ are independent additive zero mean white Gaussian noise. For both $x(t)$ and $y(t)$, the SNR is -5.946 dB. The corresponding waveforms are plotted in (a) and (b) in Fig. 2.5. In this setup of the testing signals, the signal envelope of $y(t)$ is slightly time shifted from $x(t)$ by 0.1 sec., and it suffers a frequency shift of 0.6 Hz. In addition, the phase of $y(t)$ is shifted by -1.0 (rad.) in comparison with $x(t)$. Using the variable notations in (2.29), the
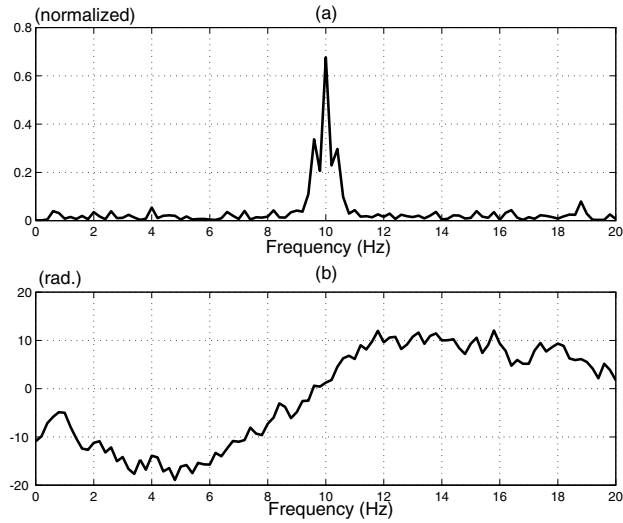
Figure 2.4: Normalized cross power spectrum of signal $x(t)$ and $y(t)$ in (a) and phase spectrum in (b)

signal pairs can be summarized as follows: t_0=2.5 sec., $\omega_0 = 2\pi \times 10$ rad./sec., Δt=0.1 sec., and $\Delta\omega$=-$2\pi \times 0.6$ rad./sec. The objective of the testing signal pair is to realize the situation depicted in Fig. 2.1.

The classical Fourier-based cross power spectrum and its phase spectrum are provided in Fig. 2.4. The cross power spectrum in Fig. 2.4-(a) is normalized by the unit area and it shows a peak amplitude at 10 Hz, the center frequency (ω_0). The phase difference at 10 Hz is 1.27 rad. whose discrepancy is 0.27 rad. (27% error) from the theoretical value, 1.0 rad. Note that the classical cross power spectral analysis utilizes the entire time series which has low SNR in this example.

Based on the definition of the cross time-frequency spectrum in (2.26), the time-frequency phase difference spectrum can be obtained. In Fig. 2.5-(a), (b), the time series of the testing signals in (2.36) and (2.37) are provided. As shown in Fig. 2.3, one can obtain time-varying phase difference spectrum for

34

a given frequency of interest by taking a cross section of the time-frequency phase difference spectrum $\Theta_{xy}(t, \omega; \phi)$; in this example, $\omega_0/2\pi$=10Hz. In Fig. 2.5-(c), (d), the cross section of the time-frequency phase difference spectrum using Wigner kernel and RID kernel respectively at 10 Hz are provided. At 2.5 sec., the cross Wigner distribution shows 1.06 rad. (6.0% error) while the cross RID shows 1.02 rad. (2.0% error). In addition, the slope of the phase difference, which corresponds to the frequency deviation $\Delta\omega$ in (2.34), is estimated to be 3.66 (rad./sec.) via the cross Wigner distribution and 3.65 (rad./sec.) via cross RID. The result is quite close to the theoretical value, 3.76 (rad./sec.). Comparing the Wigner and RID kernel results in Fig. 2.5-(c), (d), both of the kernels shows consistent results. Within the time interval where the signal is dominant, say 2-3 sec., there is no significant difference between the kernel results.

Similarly, the frequency-domain cross section of the time-frequency phase difference spectrum is provided in Fig. 2.6. Note that the plots in Fig. 2.6 corresponds to a perpendicular cross section to Fig. 2.5 at 2.5 sec. in the cross time-frequency phase spectrum as shown in Fig. 2.3. Therefore, the phase difference values at 10 Hz in Fig. 2.6-(a),(b) are the same as the values in Fig. 2.5-(c),(d) at 2.5 sec. In the frequency domain cross section, one can obtain group delay deviation (Δt). The slope of the phase difference, which corresponds to group delay deviation Δt in (2.35), are estimated to be 0.098(sec.) via cross Wigner distribution and 0.098(sec.) via cross RID. The result is quite close to the theoretical value, 0.1. No significant difference in dominant frequency bandwidth, within 9.7 and 10.3 Hz, are found for Wigner kernel and binomial RID kernel for cross time-frequency phase spectrum.

In Table 2.2, the phase difference estimation results via Fourier cross-power analysis, cross Wigner distribution and cross RID are provided in terms
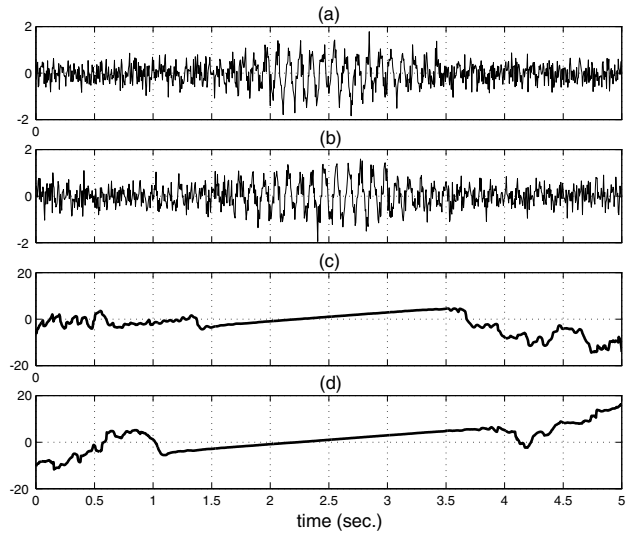
Figure 2.5: A couple of testing signals with noise $x(t)$ in (a) and $y(t)$ in (b) and corresponding phase difference estimation via Wigner kernel (c) via RID binomial kernel (d) (Note time center: 2.5 sec.)
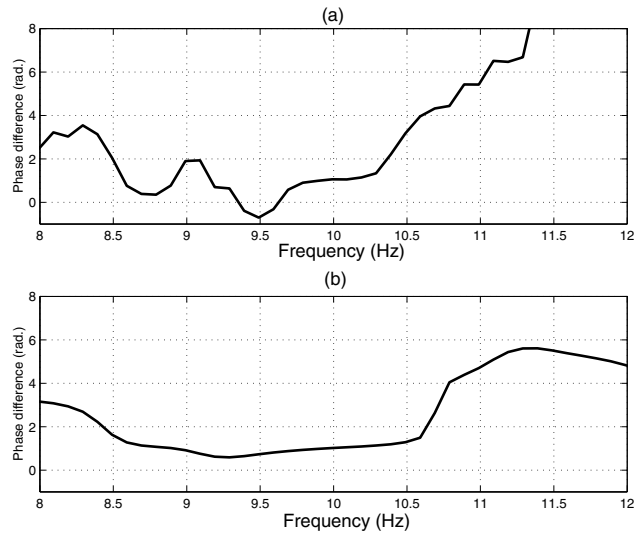
Figure 2.6: Phase difference with respect to frequency at mean time 5 sec. via Wigner kernel (a), and RID binomial kernel (b) (note: frequency of interest is 10 Hz)

36

Table 2.2: Comparisons of phase difference estimation with Fourier analysis, cross Wigner distribution, cross RID

Method	Phase difference difference	Δt	$\Delta \omega$
theoretical value	1.0 (rad.)	0.1 (sec.)	3.76 (rad./sec.)
Fourier analysis	1.27 (rad.)	N/A	N/A
cross Wigner distribution	1.06 (rad.)	0.098 (sec.)	3.66 (rad./sec.)
cross RID	1.02 (rad.)	0.098 (sec.)	3.65 (rad./sec.)

of phase difference, group delay difference (Δt) and frequency deviation ($\Delta \omega$). Cross time-frequency analysis either by Wigner or RID kernel show results close to the theoretical values. This can be interpreted in terms of the time-frequency localization of phase information: the cross time-frequency analysis takes localized signal information, so the effect of the additive Gaussian noise is less severe than cross power spectral analysis that utilizes the entire time series. As the given signal is transient with short time interval, cross time-frequency analysis shows better estimation of the phase difference.

In addition, between two signals, "exact" frequency deviation and group delay difference are also available using cross time-frequency phase spectrum. However, note that the cross time-frequency phase difference estimation requires time and frequency of interest which will be more critical for signal pairs with large deviations in time (Δt) and frequency ($\Delta \omega$). The deviations in time (Δt) and frequency ($\Delta \omega$) for a signal pair can be quantified by the deterministic correlation function, modified Moyal's formula in Table 2.1.

In other words, Moyal's formula via cross time-frequency distribution reveals how "*close*" signals are in time and frequency such that it determines the cross time-frequency phase spectrum.

The effect of kernels, especially Wigner and RID, on cross time-frequency distribution has been shown with the testing signals. Using these relatively narrowband test signals, we find no significant difference between the kernels is observed. However, if the signals have a larger frequency bandwidth or the signal is composed of multi-components, we expect that the RID kernel will be more effective. Note that the autocorrelation based classical RID suppresses the cross terms, however, the phase difference information is still available by the definition of the cross time-frequency distribution function.

2.6 Conclusion

In this chapter, the cross time-frequency distribution is derived and its properties are investigated. It is shown that the cross time-frequency distribution preserves time-frequency localized phase difference information for a transient signal pair. The relation between the classical Cohen's class and cross time-frequency distribution are provided by generalization of Moyal's formula. Using numerical simulation example with low SNR signals, we show that the cross time-frequency exhibits more robustness than the classical cross power spectral analysis by time-frequency localization. The Wigner and RID kernels are shown to be a desirable kernels to obtain adequate time-frequency localized time-frequency phase difference information.

The main advantage of the cross time-frequency distribution can be characterized by time-frequency localized phase difference information. Phase difference information is very critical to analyze physical wave propagation

phenomena in dispersive media. More investigation on the cross time-frequency distribution and application of cross time-frequency distribution to real-world signals will expand the territory of time-frequency analysis.

Chapter 3

Power Quality Indices for Transient Disturbances

3.1 Introduction

Power quality is a quality of service (QoS) issue for customer and electric power service providers and it covers a variety of transient electromagnetic phenomena in electric power distribution systems [17]. Recently, the increasing number of nonlinear loads and power electronic devices for utility and customers are becoming sources of electric power quality degradation via the generation of disturbances, e.g., impulsive transients, transient oscillations, interruptions, sag, harmonic distortion, interharmonics, etc. [18], [19]. The disturbances corrupt the power system waveforms, which are to be maintained at a fixed amplitude, frequency and sinusoidal shape. Hence, definitions, standards and evaluations are required for power quality issues. The ITIC standard [20] and IEEE 519 [21] are examples of transient power quality treatment and practice.

For assessment purposes, power quality indices are utilized to represent the degree of the quality degradation in a quantitative manner. Hence, various types of power quality indices are defined, either in the time domain or the frequency domain depending on the purpose of the application. In the time domain, the crest factor, peak and RMS values are defined, while total harmonic distortion (THD), distortion index (DIN), K-factor and telephone influence

factor (TIF), etc. are defined in the frequency domain in terms of the Fourier series coefficients [22]. Note that Fourier series coefficients are evaluated from a disturbance waveform under the assumption of periodicity. Consequently, the classical power quality indices based on Fourier series coefficients are not appropriate for transient disturbances [22]. For example, a traditional power quality index, total harmonic distortion (THD) is the most common and reasonable power quality index for a periodic disturbance. However, THD is not a suitable power quality index for transient disturbances where the frequency content involves a continuous spectrum which varies in time. The problem of applying various power quality indices based on the periodicity of disturbance to transient power quality phenomena has been carefully addressed in [22] and [23], which provide a strong motivation for this chapter. Hence, it is necessary to devise a measure of power quality to capture the "transient" and "interharmonic" characteristics of disturbance signals in power systems.

In order to analyze the transient and time varying nature of the disturbance signals in power systems, signal processing techniques have been employed for the assessment, detection, localization and classification purposes [24], [25], [26] and [27]. Recently, the wavelet transform [28], [29] and the short-time Fourier transform [30] have been frequently utilized in the study of power quality, which are characterized by the "time & scale" and "time & frequency" localization of the transient signals, respectively. Hence one can obtain "time"-localized information of the transient disturbance waveform for the detection, assessment, localization and classification via wavelet or short-time Fourier transform, whereas the "time"-localized information is not available from the classical Fourier series expansion or Fourier transform.

One of the most interesting applications is the assessment of power quality by re-defining the power quality indices for transient events using sig-

nal processing techniques. G. Heydt et. al. recognized the limitations of the traditional power quality indices [22], [23] and suggested a new definition and application of power quality indices based on the short-time Fourier transform for aperiodic signals [31]. However, as discussed in [32], the short-time Fourier transform requires a time localization window with time duration ΔT which prohibits a more general application of the power quality indices to "*nonstationary*" signals [33]. In addition, the potential applicability of time-frequency analysis to transient power quality is mentioned in [32]. In this chapter, we utilize "time-frequency analysis", which encompasses short-time Fourier transform as a special case, to provide a unified definition of various power quality indices and their application to the transient and interharmonic disturbance signals.

Time-frequency analysis [2], [4] provides a time-frequency localized energy distribution with high resolution for transient disturbance signals in power systems [34], [35]. The mathematically well-defined time-frequency distribution satisfies time and frequency marginal properties (such properties will be discussed in this chapter later), which enable one to obtain reasonable moment functions in the time and frequency domain. This feature of time-frequency analysis is suitable for development of power quality indices for transient disturbance.

3.2 Time-Frequency Based Power Quality Indices

In this section, we discuss the algorithm, definition and evaluation of the various time-frequency based power quality indices. The approach is composed of following steps:

1. **Step 1: Generation of the time-frequency distribution**

2. **Step 2: Separation of the fundamental and disturbance waveforms**

3. **Step 3: Frequency weighting of the time-frequency distribution**

4. **Step 4: Calculation of the principal average of transient power quality indices**

A flowchart of the algorithm for time-frequency based power quality indices is provided in Fig. 3.1. Each step will be discussed in detail in this section. For the discussion of the transient power quality assessment, the time-frequency based transient power quality indices are defined in Step 3. In Step 4, the principal average is introduced to quantify the time-varying transient power quality indices.

1. **Generation of the time-frequency distribution**

Based on the definition of the time-frequency distribution provided in (1.13), the first step starts with generation of the time-frequency distribution. In Fig. 3.2, a reduced interference distribution of a capacitor switching is provided. The time series data and time-frequency distribution are provided in Fig. 3.2. The capacitor switching introduces an abrupt interruption of the signal and significant frequency changes. The time-frequency distribution shows that the frequency rapidly increases from 60 Hz to 3.5 kHz in the beginning, and linearly decreases in frequency at the end of the capacitor switching. Within one cycle of 60 Hz, all frequency components above 1 kHz begin and end. The time-frequency distribution of the normal state is composed of a stripe in the 60 Hz band, whereas the time-frequency distribution of the disturbance is spread over higher frequency bands within the time interval of the disturbance. Fig. 3.2 illustrates that time-frequency analysis clearly indicates

43
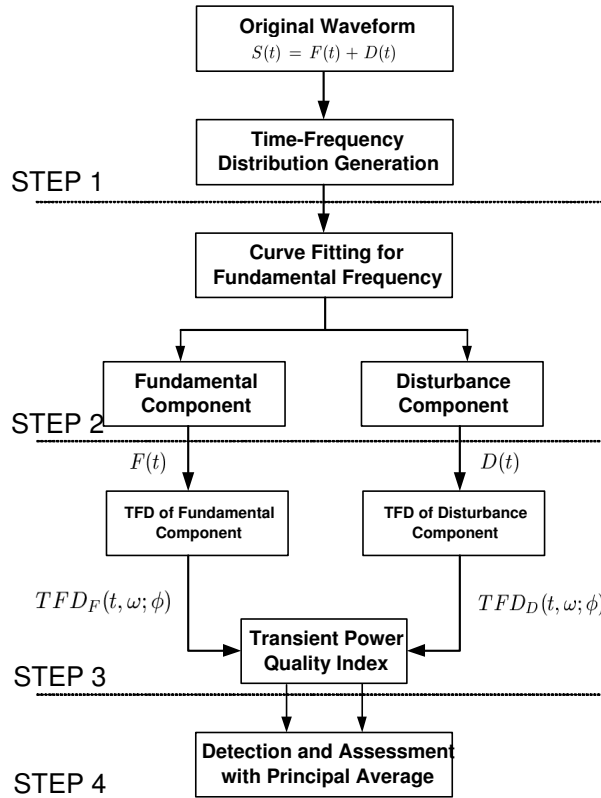
Figure 3.1: Algorithm process of the time-frequency based transient power quality assessment

how the transient energy is jointly distributed over time and frequency.

However, the dominance of the 60 Hz component impedes the high-resolution observation of the time-frequency distribution of the disturbance due to a limited dynamic range available for the disturbance component of the signal. Hence, in the next section we will introduce a set of power quality assessment evaluation algorithms to represent the time-frequency distribution of the transient disturbance by first isolating the disturbance signal from the fundamental frequency component. Furthermore, one can detect the existence

44
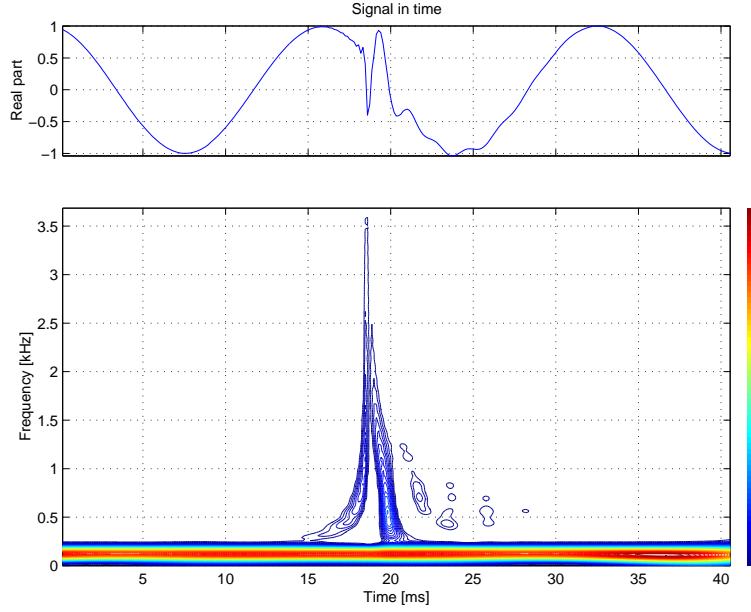
Figure 3.2: Reduced interference distribution (on bottom) of a capacitor switching disturbance (on top)

of the transient disturbance via the time-frequency based power quality indices as discussed in next section.

2. Separation of the fundamental and disturbance waveforms

Assign the fundamental frequency component of signal as $F(t)$ and disturbance signal as $D(t)$ such that the original waveform of the signal $S(t) = F(t) + D(t)$. As the fundamental frequency $(\omega_0/2\pi)$ in power systems is fixed at 60 Hz or 50 Hz, one can estimate the disturbance waveform $\hat{D}(t)$ by subtracting an estimate of the fundamental waveform $\hat{F}(t)$ from the original waveform $S(t)$ as follows:

$$\hat{D}(t) = S(t) - \hat{F}(t) \tag{3.1}$$

where $\hat{F}(t; A, \theta) = A_0 \cdot \cos(\omega_0 t + \theta)$. The amplitude of the fundamental frequency components is evaluated from the time-frequency distribution at the fundamental frequency, $TFD(t, \omega_0)$, and the phase θ_0 of the fundamental frequency is obtained by a curve fitting routine as follows:

$$\{\theta_0\} = \arg_\theta \min |S(t) - \hat{F}(t)|^2 \tag{3.2}$$

The isolation of the disturbance signal, $D(t)$, enables one to obtain greater resolution for the disturbance signal by eliminating the dominant fundamental frequency component in the time-frequency distribution. After the separation of the fundamental frequency component $\hat{F}(t)$ and the disturbance signal $\hat{D}(t)$, one can generate the time-frequency distributions of the individual signals from (1.13) as depicted in Fig. 3.1. We denote the time-frequency distribution of disturbance as $TFD_D(t, \omega; \phi)$ and that of the fundamental component as $TFD_F(t, \omega; \phi)$.

3. Frequency weighting and calculation of the time-frequency based power quality index

After obtaining the time-frequency distributions of the fundamental $TFD_F(t, \omega; \phi)$ and disturbance $TFD_D(t, \omega; \phi)$, one can define the time-frequency based power quality indices in a unified manner. There exist various ways of defining the power quality indices, however, the object of this chapter is to modify the classical power quality indices defined in terms of Fourier coefficients so that the transient power quality is to be assessed as a function of time. Therefore, we define "transient" power quality indices in terms of time-frequency distributions which collapse to the definitions of the classical power quality indices if the disturbance is periodic. In this chapter, we postulate the following four time-frequency based power quality indices: instantaneous distortion energy ratio ($IDE(t)$), normalized instantaneous distortion energy ra-

46

tio ($NIDE(t)$), instantaneous frequency ($IF(t)$), and instantaneous K-factor ($IK(t)$).

1. Instantaneous Distortion Energy Ratio

The instantaneous distortion energy ratio ($IDE(t)$) is defined as follows in terms of time-frequency distributions of the disturbance $TFD_D(t, \omega; \phi)$ and fundamental frequency components $TFD_F(t, \omega; \phi)$:

$$IDE(t) = \{\frac{\int TFD_D(t, \omega; \phi)d\omega}{\int TFD_F(t, \omega; \phi)d\omega}\}^{1/2} \times 100\% \qquad (3.3)$$

The definition of the $IDE(t)$ can be interpreted as a *"time-varying"* power quality assessment determined by the time-frequency localized energy ratio of the disturbance events to the fundamental frequency energy. In other words, $IDE(t)$ is the transient version of the total harmonic distortion (THD). Note that in $IDE(t)$, the energy of the disturbance is calculated not just from the harmonics but from all continuous frequencies. Therefore, we do not have to confine the disturbance energy to harmonics, and it is the reason why the index is named "instantaneous distortion energy ratio," not "harmonic" factor. Furthermore, interharmonics, which cannot be properly dealt with Fourier series coefficients that assume periodicity of disturbance signal can be quantified using $IDE(t)$.

2. Normalized Instantaneous Distortion Energy Ratio

Instead of the total harmonic distortion (THD), the power contribution of a periodic disturbance may be represented by the distortion index (DIN), alternatively. The concept of the distortion index (DIN) is very close to that of the total harmonic distortion (THD); however, the distortion index is defined in terms of the harmonic power divided by the total power in the waveform

itself.

$$DIN_v = \frac{\sqrt{\sum_{k=2}^{k=\infty} |v_k|^2}}{\sqrt{\sum_{k=1}^{k=\infty} |v_k|^2}} \quad (3.4)$$

This feature is an advantageous aspect of the distortion index (DIN) over the total harmonic distortion (THD) where the absence of the fundamental frequency components causes the evaluation of the index to fail [31]. Hence, the transient disturbance energy $TFD_D(t, \omega; \phi)$ can be normalized by the sum of the transient disturbance itself and fundamental energy $TFD_F(t, \omega; \phi)$ as follows:

$$NIDE(t) = \{\frac{\int TFD_D(t, \omega; \phi)d\omega}{\int TFD_D(t, \omega; \phi)d\omega + \int TFD_F(t, \omega; \phi)d\omega}\}^{1/2} \times 100\% \quad (3.5)$$

Therefore, the normalized time-varying instantaneous disturbance energy ratio corresponds to the transient version of DIN_v defined by the Fourier coefficients. Note that the $NIDE(t)$ increases with the transient disturbance energy, however, it cannot exceed a maximum value of 100 %. The relation between the THD and DIN still holds true for $NIDE(t)$ and $IDE(t)$, as indicated in the following:

$$NIDE^2(t) = \frac{1}{1 + \dfrac{\int TFD_F(t, \omega; \phi)d\omega}{\int TFD_D(t, \omega; \phi)d\omega}} = \frac{IDE^2(t)}{1 + IDE^2(t)}$$

$$NIDE(t) = IDE(t) \cdot \sqrt{\frac{1}{1 + IDE^2(t)}} \quad (3.6)$$

48

A large amplitude transient disturbance may result in a large value of $IDE(t)$, however, for $NIDE(t)$, the maximum value is bounded by 100% so that the variations of this transient power quality index is limited. Due to the relation between the $NIDE(t)$ and $IDE(t)$ shown in (3.6), for a relatively small disturbance, e.g., less than 30%, $IDE(t)$ will have a value close to $NIDE(t)$. We recognize that $IDE(t)$ and $NIDE(t)$ correspond to the square root of an appropriate energy ratio; however, to avoid awkward phraseology, we will simply use the term "energy ratio" throughout this chapter.

3. Instantaneous Frequency

The time-frequency based transient power quality indices discussed above interpret the effects of the disturbance in terms of transient energy. However, the same transient disturbance energy might have different effects on the power system depending on the local frequency content. By exploring the frequency localization via the time-frequency distribution, one can define a measure of the severity of the transient disturbance in terms of frequency deviation.

The instantaneous frequency is calculated from the time-frequency distribution as follows [2]:

$$IF(t) = \frac{\int \omega \cdot TFD_S(t, \omega; \phi) d\omega}{\int TFD_S(t, \omega; \phi) d\omega} \tag{3.7}$$

Therefore, the instantaneous frequency is a first-order moment, where each frequency component in $S(t)$ is weighted by the energy associated with that component at the time of interest. Consequently, a disturbance with higher frequency content will result in higher value of instantaneous frequency than a disturbance with lower frequency content. Hence, the instantaneous frequency is very sensitive to the onset of a transient event, which is usually composed

of high frequency components. This sensitive feature of the instantaneous frequency allows one to utilize it for the detection of the onset of a variety of transient disturbance events.

4. Instantaneous K-Factor

The K-factor is a measure of the harmonic content generation of a load, especially for transformer rating [22]. To generalize the K-factor to a transient disturbance, the square (2nd order) of the normalized frequency is weighted by the relative amount of energy associated with that frequency at the time of interest. Hence, one can define the instantaneous K-factor $IK(t)$ as follows:

$$IK(t) = \frac{\displaystyle\int \omega_N{}^2 \cdot TFD_S(t, \omega; \phi)d\omega}{\displaystyle\int TFD_D(t, \omega; \phi)d\omega + \int TFD_F(t, \omega; \phi)d\omega} \qquad (3.8)$$

where the normalized angular frequency ω_N is,

$$\omega_N = \frac{1}{2\pi} \cdot \frac{\omega}{60 \text{ Hz}} \qquad (3.9)$$

Based on the definition of the instantaneous K-factor $IK(t)$ provided in (3.8), the value of $IK(t)$ under the normal steady state conditions, will remain 1. The value of the $IK(t)$ is more sensitive to any transient variation of the waveform compared to the instantaneous frequency provided in (3.7), because, $IK(t)$ has a squared frequency, ω^2, dependence, while $IF(t)$ has just a linear frequency, ω, dependence.

4. Calculation of the principal average of transient power quality indices

The transient power quality indices provide useful information about the time-varying signature of the transient disturbance for assessment purposes. However, if the time-varying signature can be quantified as a single

number, it would be more informative and convenient for an assessment and comparison of transient power quality. Therefore, we define a "*principal average*" of the transient power quality indices, $\overline{TFPQ}$ as an average of the time-frequency based power quality index function $TFPQ(t)$ over a fundamental period T_0 as follows:

$$\overline{TFPQ} = \frac{1}{T_0} \int_{t_0-T_0/2}^{t_0+T_0/2} TFPQ(t)dt, \quad \text{where} \quad t_0 = \arg\max_t \{TFPQ(t)\}$$

$$(3.10)$$

The selection of the time interval center for the evaluation of the principal average $\overline{TFPQ}$ is determined by the time index of the local peak value of the $TFPQ(t)$, t_0. Consequently, the principal average of transient power quality indices is the local average over a T_0 sec. duration which is centered at the local peak value of the $TFPQ(t)$.

Based on the definitions of the transient power quality indices, one can assess the time-varying signatures of transient disturbances. However, it is necessary to clarify the relation between the time-frequency based transient power quality indices and classical Fourier-based power quality indices. Consider an $IDE(t)$ of a periodic disturbance signal with fundamental period $T_0 = 2\pi/\omega_0$ such that $D(t) = D(t + T_0)$. If a signal is periodic, one can obtain its Fourier series expansion as follows:

$$D(t) = \sum_{n=-\infty}^{n=\infty} d_n \cdot e^{jn\omega_0 t} \tag{3.11}$$

51

If the time-frequency distribution of the disturbance $TFD_D(t, \omega)$ satisfies the time marginal property, one can obtain the following relations:

$$
\begin{aligned}
\int TFD_D(t, \omega) d\omega &= |D(t)|^2 \\
&= \sum_{n=-\infty}^{n=\infty} d_n \cdot e^{jn\omega_0 t} \cdot \sum_{m=-\infty}^{m=\infty} d_m^* \cdot e^{-jm\omega_0 t} \\
&= \sum_{n=-\infty}^{n=\infty} \sum_{m=-\infty}^{m=\infty} d_n \cdot d_m^* e^{j(n-m)\omega_0 t} \qquad (3.12)
\end{aligned}
$$

Consider the average of the $IDE(t)$ over a fundamental period T_0 as follows:

$$
\begin{aligned}
\frac{1}{T_0} \int_{-T_0/2}^{T_0/2} \int TFD_D(t, \omega) d\omega dt &= \sum_{n=-\infty}^{n=\infty} \sum_{m=-\infty}^{m=\infty} d_n \cdot d_m^* \cdot \{\frac{1}{T_0} \int_{-T_0/2}^{T_0/2} e^{j(n-m)\omega_0 t} dt\} \\
&= \sum_{n=-\infty}^{n=\infty} \sum_{m=-\infty}^{m=\infty} d_n \cdot d_m^* \cdot \delta(n-m) \\
&= \sum_{n=-\infty}^{n=\infty} |d_n|^2 \qquad (3.13)
\end{aligned}
$$

where $d_{\pm 1} = 0$, since we are considering just the disturbance. The result corresponds to the power of the disturbance in harmonics while the total harmonic distortion indicates that it is a power ratio of disturbance to the fundamental frequency. Therefore, if a disturbance is periodic, then the average of the $IDE(t)$ over the fundamental period is equal to the total harmonic distortion. This result is not limited to the $IDE(t)$. The other types of time-frequency based power quality indices discussed in this chapter, reduce to the corresponding Fourier coefficient based power quality indices if the definition is proper and frequency marginal property is satisfied.

52

3.2.1 Transient Interharmonics

In this section, we will discuss applications of time-frequency based transient power quality indices, discussed in the previous subsection, to the interharmonic disturbance problem. Due to the aperiodic characteristics of interharmonics with respect to the fundamental frequency, the problem of measurement and assessment of interharmonics has drawn the attention to the power quality research community. The existence of frequencies other than the harmonics with respect to the sampling period result in the errors due to the end-effect in the evaluation and measurement of the Fourier coefficient based power quality indices. The major sources of the interharmonic disturbances are associated with the use of the power electronic devices (frequency converters, sub-synchronous converter cascades, induction motors, arc furnaces), which result in undesirable heating, light flicker, and peak value variation problems in power systems.

For a verification of the application of time-frequency based transient power quality indices to interharmonics, consider an example of a simulated transient interharmonic disturbance $s(t)$ as follows:

$$s(t) = \begin{cases} A \cdot \sin(2\pi f_0 \cdot t) + 0.25 \cdot A \cdot \sin(2\pi\sqrt{20} \cdot f_0 \cdot t) & (25\text{ms.} < t < 75 \text{ ms.}) \\ A \cdot \sin(2\pi f_0 \cdot t) & (\text{elsewhere}) \end{cases}$$

$$(3.14)$$

where f_0 is the fundamental frequency, 60 Hz. Employing the example of the simulated transient interharmonic disturbance, the procedures of time-frequency based transient power quality evaluation discussed in previous subsection will be discussed. At the top of Fig. 3.3, a time series of the transient interharmonic disturbance signal is presented. Note that between 25 ms. and 75 ms., an interharmonic disturbance with 25% amplitude (with respect to

53
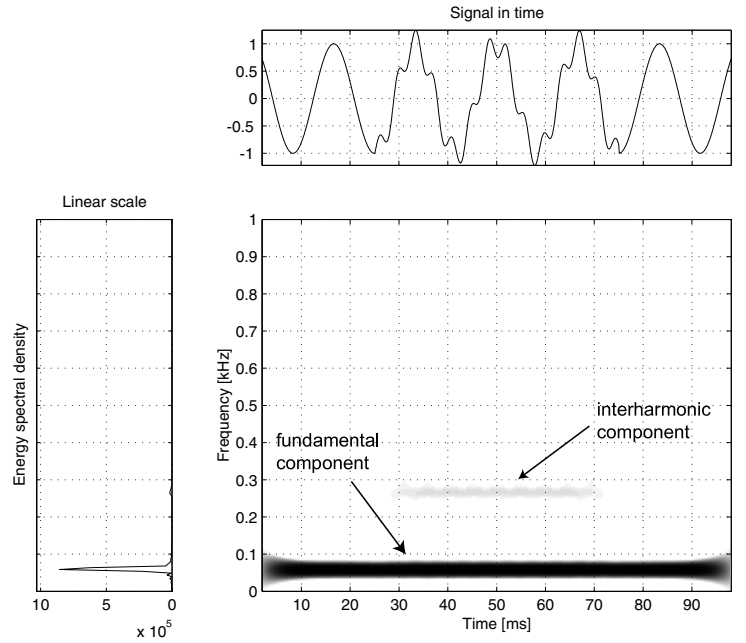
Figure 3.3: Reduced interference distribution (bottom) of a transient interharmonics waveform (top) and its energy spectrum (bottom left)

fundamental frequency component) and at 268.33 Hz $(= \sqrt{20} \times 60)$ is present. The amplitude and frequency of the interharmonic can be also found in the energy spectral density located on left side of Fig. 3.3. Due to the relatively small amplitude and duration of the interharmonics, it is difficult to observe the existence of the interharmonic component at 268.33 Hz in the energy spectral density. However, note that the time-frequency distribution provided in Fig. 3.3 clearly displays the presence of the transient interharmonic disturbance jointly in both the time and frequency domain. As shown in Fig. 3.3 one can confirm the existence of the interharmonics in time (between 25 and 75 ms.) and frequency $(268.33 \text{ Hz} = \sqrt{20} \times 60)$ simultaneously.

Based on the time-frequency distribution of the transient interharmonic

54
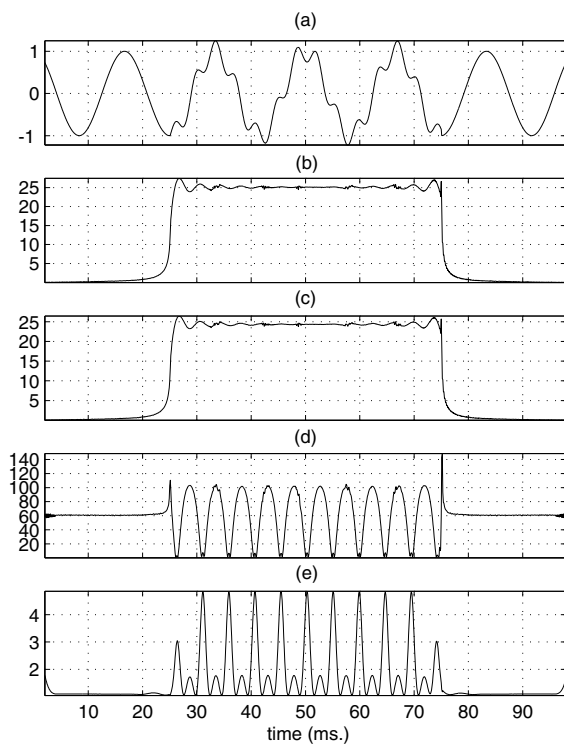
Figure 3.4: Time-frequency based transient power quality indices of the transient interharmonics: (a) Disturbance waveform, (b) Instantaneous distortion energy ratio ($IDE(t)$), (c) Normalized instantaneous distortion energy ratio ($NIDE(t)$), (d) Instantaneous frequency ($IF(t)$) and (e) Instantaneous K-factor ($IK(t)$)

disturbance provided in Fig. 3.3, one can one can successfully assess interharmonic problems by exploring the advantages of time-frequency analysis. In Fig. 3.4, various time-frequency based transient power quality indices of the transient interharmonics are provided in terms of the instantaneous distortion energy ratio ($IDE(t)$), normalized instantaneous distortion energy ratio ($NIDE(t)$), instantaneous frequency ($IF(t)$), and instantaneous K-factor ($IK(t)$). The instantaneous distortion energy ratio ($IDE(t)$) in Fig. 3.4-(b)

55

and normalized instantaneous distortion energy ratio ($NIDE(t)$) Fig. 3.4-(c) show similar value of 25% from 25 ms. to 75 ms. The beginning and end of the transient interharmonic are also detectable via a sudden increase and decrease of the time-varying power quality indices. The instantaneous frequency $IF(t)$ in Fig. 3.4-(d) depicts the existence of the interharmonic components in terms of frequency from 25 ms. to 75 ms., while the instantaneous frequency $IF(t)$ remains at 60 Hz before and after the transient interharmonic occurence. The instantaneous frequency with the transient interharmonic oscillates from 0 Hz to 100 Hz with the interharmonic cycle, whose pattern is determined by the phase difference relation between the fundamental component and the inter-harmonic components. Note that the instantaneous frequency is periodic with the interharmonic frequency (268.33 Hz $= \sqrt{20} \times 60$) whose RMS value 72.25 Hz corresponds to definition of the instantaneous frequency provided in (3.7) as follows:

$$
\frac{\displaystyle\int \omega \cdot TFD_S(t, \omega; \phi) d\omega}{\displaystyle\int TFD_S(t, \omega; \phi) d\omega} = \frac{60 \times (1)^2 + 60\sqrt{20} \times (0.25)^2}{(1)^2 + (0.25)^2}
$$

$$
= 72.25 \text{Hz} \tag{3.15}
$$

Hence, we conclude that the time-frequency based power quality indices provide a proper methodology to with which to assess interharmonic disturbances. In addition, the time-localization characteristics of the time-frequency based power quality indices allows one to detect the existence of transient interharmonics, which is not available via classical Fourier coefficient based power quality indices.

3.3 Application Examples

In this section, we will consider three real-world samples of disturbance waveforms to illustrate the time-frequency based power quality indices defined in the previous section. The first two samples are fast and slow capacitor switching disturbances. Then, a sub-transient disturbance, voltage sag is characterized by the time-frequency based power quality indices. In the following subsections, each disturbance example will be discussed individually. The real-world disturbance waveform data illustrated in this section was provided by courtesy of EPRI (Electric Power Research Institute).

3.3.1 Transient Capacitor Switching Disturbances

In Fig. 3.5, a fast capacitor switching disturbance is provided with the time-frequency distribution and the corresponding transient power quality indices are shown in Fig. 3.6. The waveform at the top of Fig. 3.5 is the original waveform and the waveform in the middle is the extracted disturbance waveform obtained by the Eq. (3.1). The time-frequency distribution of the fast capacitor switching disturbance is provided in the bottom of Fig. 3.5. The fast capacitor switching is caused by a restrike on opening; if a contactor does not successfully open during the deenegizing process, an arc is generated by re-energizing the capacitor. It is known that the disturbance generated by the capacitor switching restrike on opening exhibits transient oscillation with natural frequency determined by the capacitance and inductance of the system. Therefore, the disturbance signal is more transient and oscillatory than normal capacitor energizing, which will be considered next.

The time-frequency distribution in Fig. 3.5 shows that the transient energy of the disturbance occupies approximately 500 Hz to 1000 Hz dur-
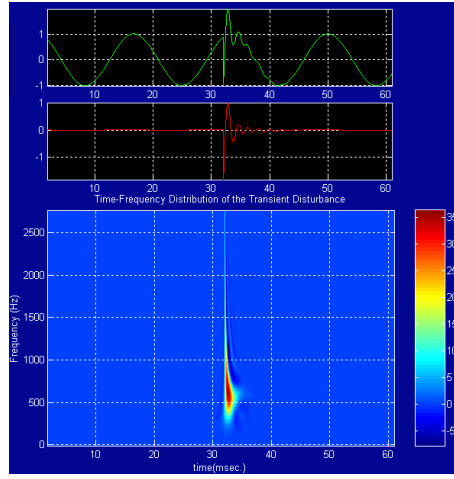
Figure 3.5: Time-frequency distribution of a fast capacitor switching disturbance

ing 32-33 ms. The instantaneous disturbance energy ratio $IDE(t)$ in Fig. 3.6-(c) shows a peak value 231.9 % at 32.04 ms while the peak of the normalized instantaneous disturbance energy ratio $NIDE(t)$ in Fig. 3.6-(d) shows a peak value 91.83% at the same time. The principal averages for $\overline{IDE(t)}$ and $\overline{NIDE(t)}$ are 17.64% and 13.56%, respectively. The instantaneous frequency shows a peak value of 2.695 kHz at 32.09 ms. and the principal average of the instantaneous frequency $\overline{IF(t)}$ is 115.65 Hz. The instantaneous K-factor shows peak value 10.14 at 32.24 ms. and the principal average of the instantaneous K-factor $\overline{IK(t)}$ is 1.65.

In Fig. 3.7, a slow capacitor switching disturbance is considered with the corresponding time-frequency distribution and corresponding transient power quality indices in Fig. 3.8. The slow capacitor switching provided in Fig. 3.7 comes from a normal capacitor switching for the correction of power factor. Hence, the disturbance caused by the slow capacitor switching
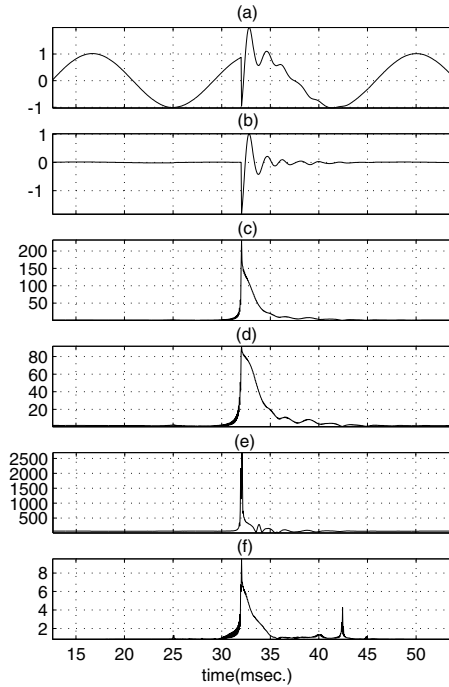
Figure 3.6: Time-frequency based transient power quality indices of the fast capacitor switching: (a) Disturbance waveform, (b) Separated disturbance waveform, (c) Instantaneous disturbance energy ratio ($IDE(t)$), (d) Normalized instantaneous distortion energy ratio ($NIDE(t)$), (e) Instantaneous frequency ($IF(t)$) and (f) Instantaneous K-factor ($IK(t)$)

is intuitively expected to be less significant than the fast capacitor switching disturbance discussed before.

The time-frequency distribution in Fig. 3.7 shows that the transient energy of the disturbance occupies between 200 Hz and 600 Hz during 12-15 ms. The instantaneous disturbance energy ratio $IDE(t)$ in Fig. 3.8-(3) shows a peak value 33.67 % at 13.00 ms, while the peak of the normalized instantaneous disturbance energy ratio $NIDE(t)$ shows a peak value 31.91%. The principal average of the $\overline{IDE(t)}$ and $\overline{NIDE(t)}$ are 6.26% and 6.19%, respec-
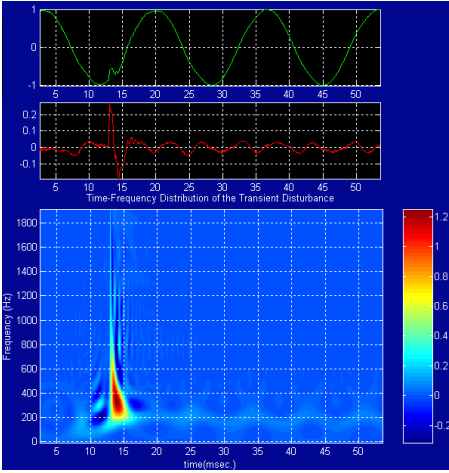
Figure 3.7: Time-frequency distribution of a slow capacitor switching distur-
bance

tively. The instantaneous frequency shows peak value 253.1 Hz at 12.87 ms.
and the principal average of the instantaneous frequency $\overline{IF(t)}$ is 64.35 Hz.
The instantaneous K-factor shows a peak value 1.73 at 13.92 ms. and the
principal average of the instantaneous K-factor $\overline{IK(t)}$ is 1.11.

The transient power quality index peak values indicate that the fast
capacitor switching is a more severe transient event than the slow capacitor
switching in terms of $IDE(t)$, $NIDE(t)$, $IF(t)$ and $IK(t)$. This result can be
confirmed by the shorter time duration and higher frequency content of the
disturbance observed in the time-frequency distributions in Figs. 3.5 and 3.7.
The ratio of the instantaneous peak values between the fast to the slow capac-
itor switch vary depending on the power quality indices : approximately 11
(2695/253.1=10.65) times higher peak $IF(t)$ and 3 (91.83/31.91=2.88) times
higher peak $NIDE(t)$. However, in terms of principal average values, the fast
capacitor switching disturbance has, approximately, 2 times higher values than

60
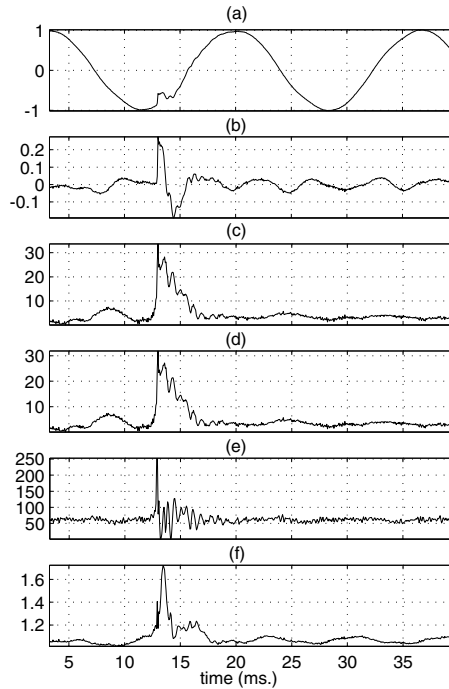
Figure 3.8: Time-frequency based transient power quality indices of the slow capacitor switching: (a) Disturbance waveform, (b) Separated disturbance waveform, (c) Instantaneous disturbance energy ratio ($IDE(t)$), (d) Normalized instantaneous distortion energy ratio ($NIDE(t)$), (e) Instantaneous frequency ($IF(t)$) and (f) Instantaneous K-factor ($IK(t)$)

the slow capacitor switching case.

3.3.2 Sub-transient Disturbance: Voltage Sag

The application of the time-frequency based transient power quality indices are not only limited to purely transient disturbances. A sub-transient voltage sag disturbance caused by a motor starting is provided with the corresponding time-frequency distribution in Fig. 3.9 and corresponding transient power quality indices in Fig. 3.10. The waveform at the top of Fig. 3.9 is the

61

original waveform and the waveform in the middle is the extracted disturbance waveform. Voltage sag is an event that exhibits a transient decrease of RMS value of the waveform which is very critical for adjustable speed drive (ASD), programmable logic controllers, microprocessors, etc.

The pattern of the time-frequency distribution is somewhat different compared with the previous two transient disturbance examples; the time-frequency distribution shows that the disturbance energy occurs at the fundamental frequency 60 Hz from 30 ms. onwards, with the amplitude slowly decreasing with time. The instantaneous disturbance energy ratio $IDE(t)$ shows an abrupt increasing peak value 21.70 % at 38.94 ms while the peak of the normalized instantaneous disturbance energy ratio $NIDE(t)$ shows a peak value 21.21% at the same time. The peak value of the $IDE(t)$ is associated with the depth of the sag; 80% of the nominal amplitude results in the value of approximately 20% instantaneous disturbance energy ratio. The slow recovery of the voltage sag is observed by the decreasing values of the $IDE(t)$ and $NIDE(t)$ in Fig 3.10. The principal average values of the $\overline{IDE(t)}$ and $\overline{NIDE(t)}$ are 18.42% and 18.10%, respectively.

The instantaneous frequency exhibits a peak value 155.3 Hz at 30.81 ms., which is the exact time of the start of the voltage sag. The value of instantaneous frequency and its time index demonstrates that the instantaneous frequency is a powerful tool for accurate detection of the voltage sag initiation, which has been traditionally treated by RMS values or wavelet transforms. The principal average of the instantaneous frequency is very close to 60 Hz, i.e., $\overline{IF(t)}$ is 59.76 Hz. The instantaneous K-factor shows peak value 2.04 at 22.05 ms. The principal average of the instantaneous K-factor $\overline{IK(t)}$ is 1.07, which implies very small variation of the frequency content as is true for the case of voltage sag.
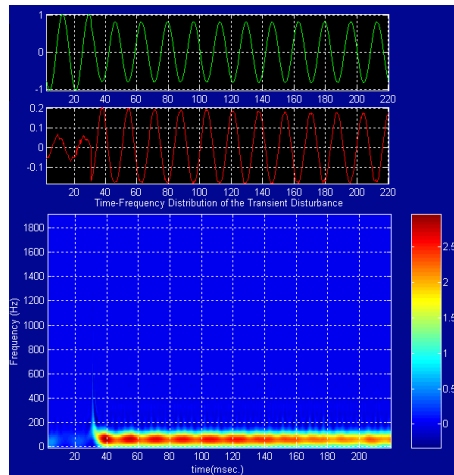
Figure 3.9: Time-frequency distribution of a voltage sag disturbance

In terms of the principal averages of the instantaneous frequency and instantaneous K-factor, the voltage sag does not affect the frequency very much which remains very close to the fundamental frequency and its normalized value of 1. However, the variations of the amplitude are reflected in the values of the disturbance energy ratio. In the case of voltage sag, a sub-transient disturbance, the peak values are relatively smaller than the transient distur- bances; moreover, the differences between the peak value and principal average values of energy are relatively smaller compared to the transient cases due to the slower variations of the voltage sag. This example of transient power qual- ity assessment for voltage sag confirms the fact that the time-frequency based power quality indices, $IDE(t)$ and $NIDE(t)$, are very informative regarding to the sub-transient disturbances. Moreover, the instantaneous frequency and instantaneous K-factor provide accurate and sensitive detection of the time of occurrence of the voltage sag as shown in Fig. 3.10.

In Table 3.1, a summary of the various power quality indices is provided

63
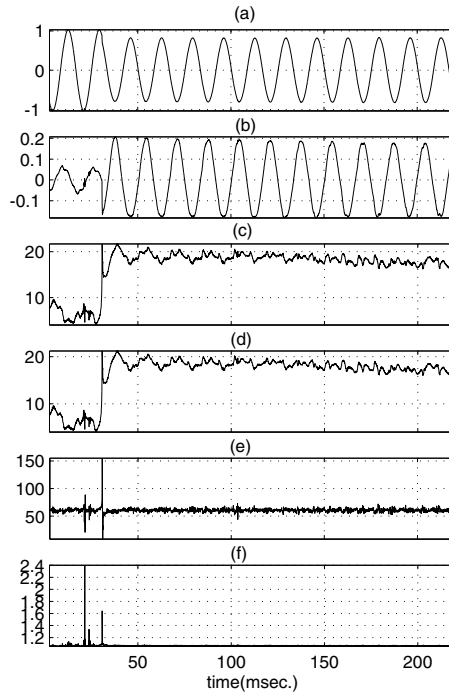
Figure 3.10: Time-frequency based transient power quality indices of voltage sag: (a) Disturbance waveform, (b) Separated disturbance waveform, (c) Instantaneous disturbance energy ratio ($IDE(t)$), (d) Normalized instantaneous distortion energy ratio ($NIDE(t)$), (e) Instantaneous frequency ($IF(t)$) and (f) Instantaneous K-factor ($IK(t)$)

for the four examples discussed in this chapter. Comparing the disturbance examples in terms of their respective time-frequency based transient power quality indices, one can determine and compare the transient power quality in a quantitative way. It is difficult to tell which is the "best" power quality index, because they have different parameter dimensions; Hz (or equivalently rad./sec. for angular frequency notation) for $IF(t)$, dimensionless energy percentage for $IDE(t)$ and $NIDE(t)$, and dimensionless frequency squared for $IK(t)$. However, if one determines a dimension or purpose of the

64

Table 3.1: Summary of transient power quality indices for the examples

		Fast cap. switching	Slow cap. switching	Motor starting
Type of disturbance		Transient	Transient	Sub-transient
IDE	peak time (ms.)	32.04	13.00	38.94
	peak value (%)	231.92	33.67	21.70
	principal average	17.64	6.26	18.42
NIDE	peak time (ms.)	32.04	13.00	38.94
	peak value (%)	91.83	31.91	21.21
	principal average	13.56	6.19	18.10
IF	peak time (ms.)	32.09	12.87	30.81
	peak value (Hz)	2695	253.1	155.3
	principal average	115.65	64.35	59.76
IK	peak time (ms.)	32.24	13.92	22.05
	peak value	10.14	1.73	2.04
	principal average	1.65	1.11	1.07

transient power quality index, one can select an appropriate corresponding time-frequency based transient power quality index. If one needs an assessment of transient power quality in terms of energy, one can choose $IDE(t)$ or $NIDE(t)$. If one needs an assessment of transient power quality in terms of frequency, one can choose $IF(t)$ or $IK(t)$. If one needs an assessment of transient power quality in terms of a specific frequency spectrum (for example, telephone interference factor), one can customize time-frequency based transient power quality indices once one has calculated $TFD_D(t,\omega)$ and $TFD_F(t,\omega)$. Note that irrespective of power quality index selection, the time-frequency based power quality indices provide time-varying frequency signatures of the transient disturbance.

3.4 Conclusion

In this chapter, power quality assessment for transient disturbance signals has been carefully treated by time-frequency analysis. The limitations of the traditional Fourier series coefficient based power quality indices, which inherently require periodicity of the disturbance signal, has been resolved by use of the time-frequency analysis. Utilizing the time and frequency localization of the time-frequency distribution, the following time-frequency based power quality indices are proposed: the instantaneous disturbance energy ratio, normalized instantaneous disturbance energy ratio, instantaneous frequency, and instantaneous K-factor. The first two power quality indices characterize the disturbance in terms of energy, while the latter two power quality indices characterize the disturbance in terms of frequency deviation. Furthermore, the application of the time-frequency based power quality indices can be extended to the assessment and detection of sub-transient and periodic disturbances. In this chapter, the efficacy of the time-frequency based power quality indices has been demonstrated by the use of real-world disturbance examples.

Chapter 4

Time-Frequency Domain Solution for a Direction Finder of Transient Power Quality Disturbances

4.1 Introduction

Power quality has been an important issue in power systems engineering with the increased number of power electronic devices and sensitive electronic loads. Capacitor banks are placed in power distribution systems to provide voltage support and correct displacement power factor. However, the capacitor switching in power distribution system results in a transient over-voltage with oscillation, which is one of the most common and critical power quality events followed by voltage sags. The impact of capacitor switching on customer systems has been recognized in the early 90's [36]. For a more fair management of power quality in the near future, the responsible parties are expected to be penalized for the degradation of power quality.

Unfortunately, although the capacitor switching disturbance is one of the most common disturbances in power distribution systems, the abilities and methodologies to locate the capacitor switching is limited. Capacitor switching localization was proposed by the identification of a transient parameter [37], which requires the knowledge of system parameters, capacitor size and configuration. Hence, as an alternative, waveform based solutions have been proposed. An empirical approach has been proposed in terms of instantaneous

67

power and disturbance power [38] and signature analysis has been proposed in order to track the capacitor switching performance [39]. In order to provide an analytic solution of the capacitor switching localization, a time-domain Kalman filter based solution has been proposed [40].

Irrespecting of the different approaches to capacitor switching localization, the difficulties of the problem are caused by the "transient" and "oscillatory" nature of the disturbance event. For steady state power systems, the direction of power flow is determined by the phase angles between voltage and current, which correspond to the power factor at the fundamental frequency. However, for transient events it is necessary to investigate the phase difference relations of the transient disturbance waveforms in both a "time" and "frequency" domain localized manner. In this chapter, we propose an advanced signal processing, i.e., cross time-frequency analysis, based analytic solution to the localization of transient capacitor switching. The time-frequency based analytic solution provides determination of the transient power flow direction in terms of time and frequency localized phase difference.

4.2   Transient Circuit Analysis of Capacitor Switching

In this section, we will investigate a fundamental, but simple, structure of an electric power network with its analytic transient response solutions. Consider a simplified RLC transient resonant electric circuit diagram in Fig. 4.1. The circuit diagram provided in Fig. 4.1 depicts a set of capacitor switching scenarios at different spatial locations: with respect to the observation points (dashed box in Fig. 4.1) capacitor A is located upstream, capacitor B is located in the middle and capacitor C is located downstream, respectively. Based on the observed voltage $(v_1(t), v_2(t))$ and current $(i_1(t), i_2(t))$ waveforms
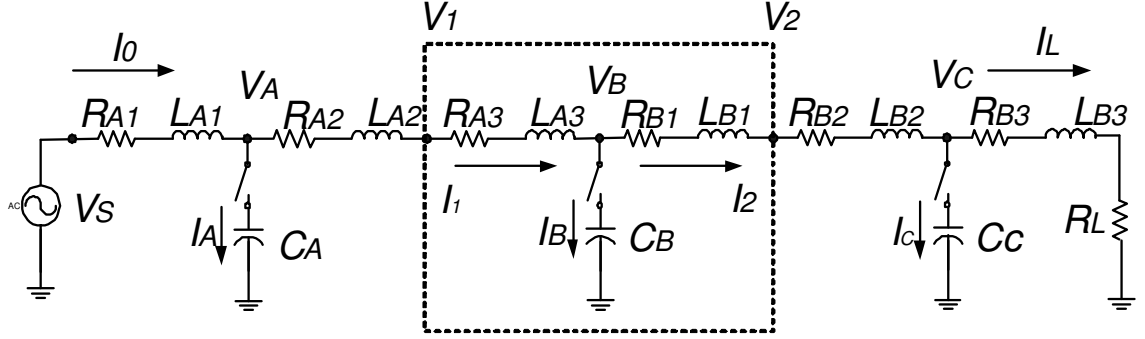
Figure 4.1: A simplified RLC transient resonant electric circuit diagram

the phase difference angles of the transient disturbance are to be determined. Consider the transient solutions of the capacitor B switching first, then the solutions of the others will follow. The differential equations for the capacitor B switching can be written as follows in terms of voltage and current:

$$-v_s(t) + R_A \cdot i_1(t) + L_A \frac{di_1(t)}{dt} + v_B(t) = 0$$

$$-v_B(t) + L_B \frac{di_2(t)}{dt} + (R_B + R_L) \cdot i_2(t) = 0$$

$$i_1(t) - i_2(t) - C_B \frac{dv_B(t)}{dt} = 0 \tag{4.1}$$

where $R_A = R_{A_1} + R_{A_2} + R_{A_3}$, $L_A = L_{A_1} + L_{A_2} + L_{A_3}$, $R_B = R_{B_1} + R_{B_2} + R_{B_3}$, and $L_B = L_{B_1} + L_{B_2} + L_{B_3}$. The initial conditions of the system are:

$$v_B(t = t_0^+) = 0, v_B'(t = t_0^+) = 0 \tag{4.2}$$

where t_0 is the arbitrary time instance of the capacitor switching. The solution of (4.1) is stable and underdamped, which is characterized by a decay factor α and resonance frequency ω_f. (Note that ω_0 stands for the fundamental frequency of the power system.) By solving the equations above, one can

69

obtain a solution of the reference voltage $v_B(t)$ as follows:

$$
\begin{aligned}
v_B(t) &= V_B \cdot \sin(\omega_0(t - t_0) + \theta_0) + \frac{\omega_0}{\omega_f} \cdot V_B \cdot e^{-\alpha(t-t_0)} \sin \omega_f(t - t_0) \\
&\quad - \frac{\sigma}{\sigma^2 + 1} \cdot \alpha \cdot V_B \cdot e^{-\sigma(t-t_0)} \\
&\cong V_B \cdot \sin(\omega_0(t - t_0) + \theta_0) + \frac{\omega_0}{\omega_f} \cdot V_B \cdot e^{-\alpha(t-t_0)} \sin \omega_f(t - t_0) \\
&\quad (\alpha > 0, \ \omega_f > 0, \ \sigma \gg 0, \ t \geq t_0)
\end{aligned}
$$

$$
\text{where} \qquad \tan \theta_0 = \frac{\alpha \cdot \sigma}{\sigma^2(\alpha - 1) - 1} \tag{4.3}
$$

V_B represents the nominal amplitude value of the voltage source $V_s(t) = V_s \cdot \sin(\omega_0 t)$ in the steady-state. The value of σ is typically large enough, thus $e^{-\sigma(t-t_0)}$ can be reasonably approximated to be zero. Based on the solution of $v_B(t)$ in (4.3), the transient components of the currents $i_1(t)$ and $i_2(t)$, which we denote by $\tilde{i}_1(t)$ and $\tilde{i}_2(t)$, associated with the disturbance at frequency ω_f, are obtained as follows:

$$
\begin{aligned}
\tilde{i}_1(t) &= I_1 \cdot e^{-\alpha(t-t_0)} \sin(\omega_f(t - t_0) - \theta_1), \\
\text{where} \qquad \tan \theta_1 &= \frac{L_A \cdot \omega_f}{R_A - \alpha \cdot L_A}, \quad (0 < \theta_1 < \pi) \tag{4.4}
\end{aligned}
$$

$$
\begin{aligned}
\tilde{i}_2(t) &= I_2 \cdot e^{-\alpha(t-t_0)} \sin(\omega_f(t - t_0) - \theta_2), \\
\text{where} \qquad \tan \theta_2 &= -\frac{L_B \cdot \omega_f}{(R_B + R_L) - \alpha \cdot L_B}, \quad (-\pi < \theta_2 < 0) \tag{4.5}
\end{aligned}
$$

where I_1 and I_2 are the amplitude of the transient oscillation determined by the system parameter and initial conditions. Note to the phases of the current in (4.4) and (4.5). The solutions of the current, $\tilde{i}_1(t)$ and $\tilde{i}_2(t)$, allow one to obtain solutions of the voltage at the observation points, $v_1(t)$ and $v_2(t)$ as

70

follows:

$$
\begin{aligned}
v_1(t) &= v_B(t) + R_{A_3} \cdot i_1(t) + L_{A_3} \cdot \frac{i_1(t)}{dt} \\
&= (V_B + \delta V_{B_1}) \cdot \{\sin(\omega_0 t - \delta_1) + e^{-\alpha(t-t_0)}\sin(\omega_f(t - t_0) - \delta_1')\}, \\
&\quad \text{where} \quad (V_B \gg \delta V_{B_1}, \delta_1 \approx 0) \\
v_2(t) &= v_B(t) - R_{B_1} \cdot i_2(t) - L_{B_1} \cdot \frac{i_2(t)}{dt} \\
&= (V_B - \delta V_{B_2}) \cdot \{\sin(\omega_0 t + \delta_2) + e^{-\alpha(t-t_0)}\sin(\omega_f(t - t_0) + \delta_2')\}, \\
&\quad \text{where} \quad (V_B \gg \delta V_{B_2}, \delta_2 \approx 0) \quad\quad\quad\quad (4.6)
\end{aligned}
$$

The additional variables are introduced for voltage, $(\delta V_{B_1}, \delta V_{B_2})$, and phase, $(\delta_1, \delta_1', \delta_2, \delta_2')$, respectively. However, the variations in amplitude and phase are relatively small and the exact values can be evaluated, if needed, with knowledge of the distribution line characteristics, i.e., R_1, R_2, L_1, and L_2.

Comparing the transient solutions of the current waveforms, $(\tilde{i}_1(t), \tilde{i}_2(t))$ and voltage waveforms $(v_1(t), v_2(t))$, one can find that the direction of the transient power flow due to the capacitor switching is determined by the phase difference between voltage and current at the time of capacitor switching and frequency of transient oscillation. If the phase angle of current leads that of voltage $(\theta_1 > \delta_1')$, the switched capacitor is located at the downstream direction while the phase angle of current lags that of voltage $(\theta_2 < \delta_2')$, the switched capacitor is located at the upstream direction.

Based on the solutions of the circuit, the transient voltage and current waveforms can be obtained so that the phase relation can be extended to capacitor A switching (upstream) and capacitor C switching (downstream). In the case of capacitor A switching (upstream direction), the current $\tilde{i}_1(t)$ and $\tilde{i}_2(t)$ correspond to the transient solution provided in (4.4) and (4.5) (of course with small degree of phase difference caused by the lines) phase difference so

71

that the phase angles of the currents I_1 and I_2 lags the phase angles of the voltage V_1 and V_2. Likewise, the capacitor C switching (downstream direction) will result in leading phase of currents with respect to the voltages.

The voltage and current phase relations discussed above is summarized by a set of phase angle relations in Fig. 4.2. Based on the phase relation discussed above, the capacitor switching in the middle (C_B) will result in the leading phase for current I_1 with the lagging phase for current I_2. The capacitor switching at the upstream results in the lagging phase angle of both currents with respect to the voltage as depicted in Fig. 4.2-(a). Likewise, the capacitor switching at the downstream results in the leading phase angle of both currents with respect to the voltage as depicted in Fig. 4.2-(c). Note that in each figure, the leading or lagging phase relation between voltage and current associated with flow of energy provided in Fig. 4.2 corresponds to classical notations of power flow in the steady state.

From the viewpoint of measurement, the phase itself is meaningless; the phase relation can be obtained by the measurement of phase "difference". Hence, the phase relation in Fig. 4.2 is represented in terms of following factors of phase difference between voltage (V_1, V_2) and current (I_1, I_2):

1. $\Theta_{V_1 V_2}$: Phase difference of voltages, V_1 with respect to V_2.

2. $\Theta_{I_1 I_2}$: Phase difference of currents, I_1 with respect to I_2.

3. $\Theta_{V_1 I_1}$: Phase difference of voltage (V_1) with respect to current (I_1) at observation point 1

4. $\Theta_{V_2 I_2}$: Phase difference of voltage (V_2) with respect to current (I_2) at observation point 2
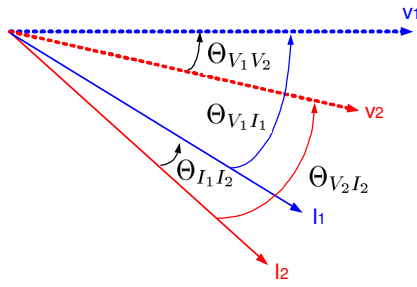
72

(a) Phase angle relation for Case A
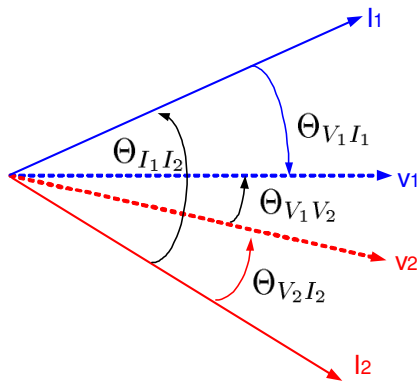
(b) Phase angle relation for Case B
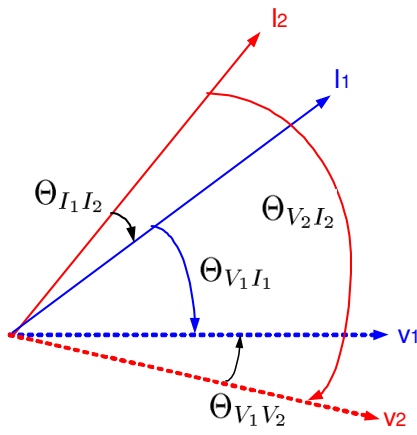
(c) Phase angle relation for Case C

Figure 4.2: Phase angle relation for Case A, B and C

Hence, via the measurement of time and frequency localized phase differences listed above, one can construct the phase relation diagram to determine the location of the transient capacitor switching as depicted in Fig. 4.2.

4.3   Time-Frequency Localized Phase Difference Evaluation

The direction of real and reactive power flow in the steady state can be identified by comparing power factor. The power factor is determined by the phase difference between voltage and current at the fundamental frequency. However, in the case of a transient, it is not a simple task to determine the phase difference between voltage and current to identify the direction of real and reactive power flow. Especially in case of capacitor switching, the disturbance is localized over a short time duration with a transient resonance frequency, ω_f, which is clearly different from the fundamental frequency, ω_0. In this chapter, we will provide a methodology to obtain time- and frequency-localized phase difference so that one can determine the direction of transient disturbance flow in terms of phase difference.

In order to obtain time- and frequency-localized phase difference information for transient disturbance voltage and current waveform pairs, it is necessary to utilize a new state-of-the-art method, cross time-frequency analysis discussed in Chapter 2. The cross time-frequency distribution $S_{vi}(t, \omega; \phi)$ of voltage $v(t)$ and current $i(t)$ is defined as follows:

$$S_{vi}(t, \omega; \phi) = \frac{1}{4\pi^2} \int \int \int v(u + \frac{\tau}{2}) \cdot i^*(u - \frac{\tau}{2}) \phi(\theta, \tau) e^{-j\theta t - j\tau\omega + j\theta u} d\theta d\tau du \quad (4.7)$$

where $\phi(\theta, \tau)$ is the kernel of the cross time-frequency distribution, and $v(t)$ and $i(t)$ are now analytic signal representations of the voltage and current

waveforms. Thus, one can define "time-frequency complex power" as follows:

$$S_{vi}(t,\omega) = |S_{vi}(t,\omega)|e^{j\Theta_{vi}(t,\omega)} \tag{4.8}$$

where the time-frequency phase difference spectrum $\Theta_{vi}(t,\omega)$ corresponds the time-frequency phase difference angle between voltage and current by following relation:

$$\Theta_{vi}(t,\omega) = \Theta_v(t,\omega) - \Theta_i(t,\omega) \tag{4.9}$$

Note that the time-frequency phase difference above corresponds to the classical notation of power angle. Conceptually, it is equivalent to the classical power angle, however, the phase difference between voltage and current is defined in terms of "time" and "frequency" simultaneously. In addition, the cross time-frequency distribution satisfies time and frequency marginal properties such that:

$$
\begin{aligned}
\int S_{vi}(t,\omega)d\omega &= v(t) \cdot i^*(t) \qquad &: \text{Time Marginal} \\
\int S_{vi}(t,\omega)dt &= V(\omega) \cdot I^*(\omega) \qquad &: \text{Frequency Marginal}
\end{aligned}
$$

$$\tag{4.10}$$

Hence, the time and frequency marginal properties guarantee that the analysis based on cross time-frequency distribution collapses to the classical notations of power in the time domain or frequency domain for the steady state. Thus, based on the time and frequency marginal properties, the instantaneous real power $P(t)$ and reactive power $Q(t)$ can be defined in terms of time and frequency simultaneously as follows:

$$
\begin{aligned}
P(t) &= \Re\{\int S_{vi}(t,\omega)d\omega\} \quad \text{:Instantaneous Real Power} \\
Q(t) &= \Im\{\int S_{vi}(t,\omega)d\omega\} \quad \text{:Instantaneous Reactive Power}
\end{aligned}
$$

$$\tag{4.11}$$
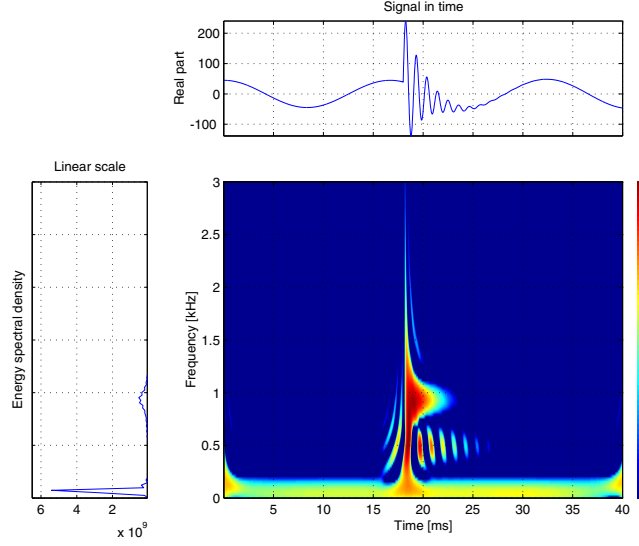
Figure 4.3: Time-frequency distribution of the capacitor switching disturbance in current (Capacitor B)

Therefore, from the complex cross time-frequency distribution, one can obtain time-frequency phase difference spectrum as follows:

$$\Theta_{vi}(t,\omega;\phi) = \tan^{-1}\{\frac{\Im\{S_{vi}(t,\omega;\phi)\}}{\Re\{S_{vi}(t,\omega;\phi)\}}\}$$

where $\Re$ and $\Im$ denote the real and imaginary parts, respectively. Note that in order to obtain a reasonable measure of time- and frequency-localized phase difference, knowledge of the proper time and frequency locations on which to focus is required [41] . This time and frequency localization information is obtained from the classical time-frequency distribution. Based on the transient solution of the voltage in (4.6), $v_1(t) = (V_B + \delta V_{B_1}) \cdot e^{-\alpha t} \sin(\omega_f t - \delta_1)$, and current in (4.4), $i_1(t) = I_1(0^+) \cdot e^{-\alpha t} \sin(\omega_f t - \theta_1)$, waveforms caused by the capacitor switching, consider the cross time-frequency distribution with

76

Wigner kernel, (for a simple calculation), i.e., $\phi(\theta, \tau) = 1$, as follows:

$$
\begin{aligned}
S_{vi}(t, \omega; \phi = 1) &= \frac{1}{4\pi^2} \int \int \int v(u + \frac{\tau}{2}) \cdot i^*(u - \frac{\tau}{2}) e^{-j\theta t - j\tau\omega + j\theta u} d\theta d\tau du \\
&= \frac{1}{2\pi} \int v(t + \tau/2) \cdot i^*(t - \tau/2) e^{-j\omega\tau} d\tau \\
&\cong (V_B + \delta V_{B_1}) \cdot I_1(0^+) \cdot e^{-2\alpha(t - t_0)} \cdot \delta(\omega - \omega_f) \cdot e^{j(\theta_1 - \delta_1)}
\end{aligned}
$$

(4.12)

The approximation in the last step to ideal delta function in (4.12) owes to the properties of Hilbert transform. Because of the fast exponential decay of the envelope, the actual time-frequency distribution will spread and be centered at the transient resonance frequency ω_f. The interpretation of the (4.12) should be focused on the localized phase difference at time t_0 and frequency ω_f of interest. Hence, from the cross time-frequency distribution in (4.12), one can obtain time-frequency phase difference spectrum:

$$
\Theta_{V_1 I_1}(t_0, \omega_f) = (\theta_1 - \delta_1)
$$

(4.13)

where t_0 denotes the time of capacitor switching to be determined below via the time-frequency distribution.

From (4.13), one can find that it is necessary to determine the frequency of interest, i.e., the transient resonance frequency ω_f for a proper estimation of the time-frequency localized phase difference. The determination of the time and frequency of interest can be achieved by the classical time-frequency distribution where the "energy" of a signal is represented in terms of time and frequency simultaneously while the cross time-frequency distribution represent the "phase difference" in terms of time and frequency. Wigner distribution is defined as follows:

$$
W_s(t, \omega) = \frac{1}{2\pi} \int s(t - \frac{1}{2}\tau) s^*(t + \frac{1}{2}\tau) e^{-j\tau\omega} d\tau
$$

(4.14)

For this analysis, plug in transient disturbance current waveform $s(t) = i_1(t) = I_1(0^+) \cdot e^{-\alpha(t-t_0)} \sin(\omega_f t - \theta_1)$, then the Wigner distribution of the transient disturbance current is,

$$TFD_s(t, \omega) \cong I_c^2(0^+) \cdot e^{-2\alpha(t-t_0)} \delta(\omega - \omega_f) \qquad (4.15)$$

The basis for the approximation in (4.15) is the same with the approximation discussed in (4.13). (The numerical calculations of the time-frequency distribution of the signal will be discussed in later.) Hence, the time and frequency localization of the time-frequency phase difference can be determined as follows:

$$\{t_0, \omega_f\} = \arg \max_{t, \omega \neq \omega_0} \{TFD_s(t, \omega)\} \qquad (4.16)$$

In order to illustrate the time and frequency localization, consider a time-frequency distribution of a transient capacitor switching disturbance provided in Fig. 4.3. The time series provided in the top of Fig. 4.3 is a capacitor switching disturbance (the description of the waveform will be discussed in detail in the next section). The time-frequency distribution of the disturbance is provided in the bottom right of Fig. 4.3 with the frequency domain energy spectrum in the bottom left of Fig. 4.3. On the frequency domain energy spectrum, the fundamental frequency component located at 60 Hz is dominant while the transient oscillation component located around 1 kHz is relatively small in magnitude. However, the time-frequency distribution in Fig. 4.3 represent the transient signature of the capacitor switching disturbance. Therefore, applying the formula provided in (4.16) to the time-frequency distribution in Fig. 4.3 allows one to determine the time (18.78 ms.) and frequency (953.7 Hz) of interest for the capacitor switching disturbance.

Based on the discussion of the time-frequency phase difference
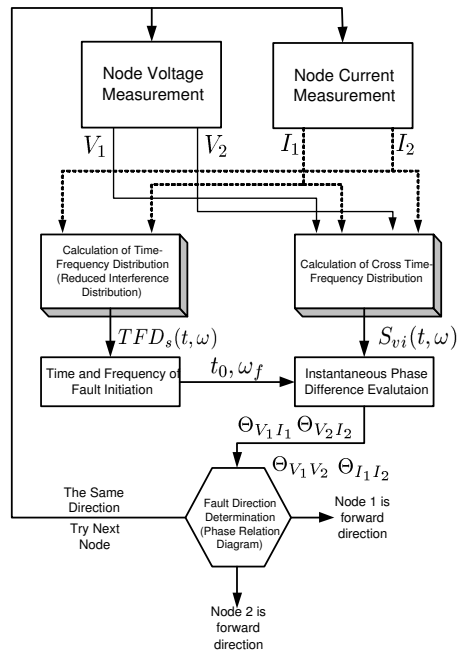
Figure 4.4: Flowchart of the algorithm for determination of transient power flow direction
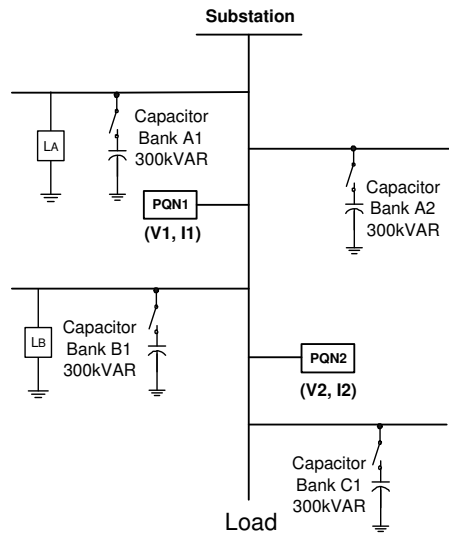
Figure 4.5: EMTP simulation power distribution network for transient capacitor switching

79
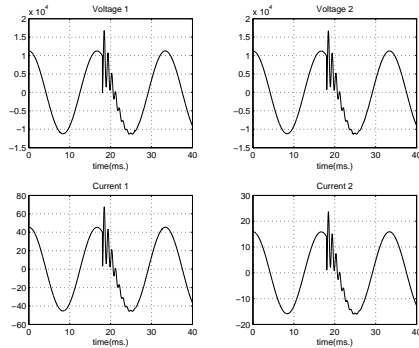
(a) Transient disturbance voltage and current waveform caused by capacitor A switching
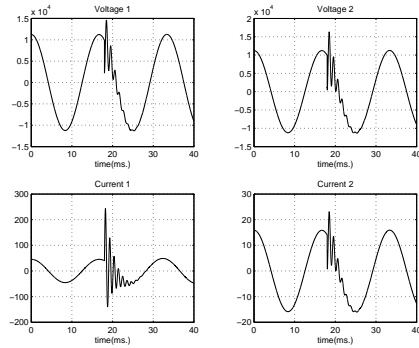
(b) Transient disturbance voltage and current waveform caused by capacitor B switching
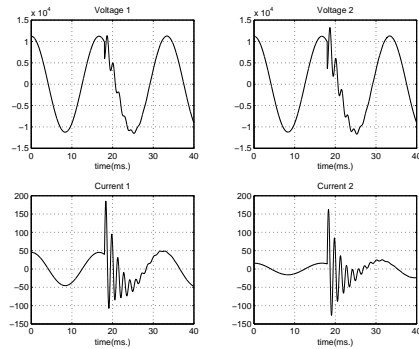
(c) Transient disturbance voltage and current waveform caused by capacitor C switching

Figure 4.6: Transient disturbance voltage and current waveform caused by capacitor A, B, and C switching

80

spectrum in this section, a flowchart to determine the location of capacitor switching is provided in Fig. 4.4. The algorithmic process is based on the transient disturbance voltage $(v_1(t), v_2(t))$ and current $(i_1(t), i_2(t))$ waveform observation. The voltage and current waveform pairs will be utilized for the calculation of the cross time-frequency distribution provided in (4.7). Using the definition provided in (4.8), the cross time-frequency can be utilized to calculate the time-frequency phase difference spectrum. However, in order to evaluate the instantaneous phase difference spectrum at the time of switching and at the frequency of transient oscillation, it is necessary to evaluate the time and frequency of interest provided in (4.16) via the time-frequency distribution provided in (4.14). Therefore, we will utilize the current waveform of the disturbance to evaluate the time and frequency of interest $\{t_0, \omega_f\}$ at the observation points as illustrated in Fig. 4.4. Then the measurement of time-frequency localized phase difference allows one to map the phase relation into one of types depicted in Fig. 4.2 so that one can determine the relative location of capacitor switching. For a pinpoint location of the capacitor switching, this process can be continues to find the capacitor switching located in the middle of the observation points. The sequence of determining the location of the capacitor switching can be repeated by moving the nodes of interest in order to pinpoint the source of capacitor switching disturbance as indicated in Fig. 4.4.

4.4 EMTP Simulation and Analysis

In this section, we will demonstrate the application of time-frequency analysis for the relative localization of the capacitor switching. For the verification of the theoretical derivation discussed in the previous section, we will

employ an EMTP simulation of the network as provided in Fig. 4.5.

In Fig. 4.5, a schematic description of the power distribution feeder at 8kV with 4 distributed capacitors is provided. Each capacitor bank consists of 300 kVAR capacitors. Each power distribution line segment consists of a resistance (0.25 Ω) and inductance (1.57 mH). The voltage and current transient disturbance waveforms are monitored and recorded at the PQN1 $(v_1(t), i_1(t))$ and PQN2 $(v_2(t), i_2(t))$, respectively. With respect to the location of the observation points (PQN1 and PQN2), the capacitor A is located at the upstream direction, the capacitor B is located in the middle, the capacitor C is located at the downstream direction, respectively. The configuration provided in Fig. 4.5 corresponds to the circuit diagram provided in Fig. 4.1 for transient analysis. Based on the observed voltage and current waveforms, the location of the swtiched capacitor will be identified by the time-frequency based methodology discussed in the previous section.

In Fig. 4.6, a set of transient disturbance voltage and current waveform caused by capacitor A, B, and C switching are provided. Each subfigure consists of the transient disturbance voltage waveforms $(v_1(t), v_2(t))$ on top and current waveforms $(i_1(t), i_2(t))$ on bottom. Each capacitor switching disturbance event occurs at 18 ms. as shown in Fig. 4.6. At the instance of capacitor switching, the node voltages $(v_1(t)$ and $v_2(t))$ drop, then the transient decay oscillation continues for less than a fundamental cycle. At the instance of the capacitor switching, the disturbance current shows abrupt decrease $(i_1(t), i_2(t)$ in Fig. 4.6-(a)) or increase $(i_1(t), i_2(t)$ in Fig. 4.6-(c)) depending on the location of the capacitor switching. When the switched capacitor is located between node 1 and 2, $i_1(t)$ initially increase while $i_2(t)$ decreases showin in Fig. 4.6-(b).

Comparing the sets of disturbance waveforms in time domain in differ-

ent scenario of capacitor switching provided in Fig. 4.6-(a) (c), one can quantitatively observe the variations of transient resonat frequency. Depending on the configuration of the distribution system and size of the switched capacitor, the transiet resonant frequency varies. One can observe that the transient resonant frequency decreases from capacitor A through B and C in time domain. However, it is necessary to extract the quantitative phase difference relation between the transient disturbance voltage and current waveforms in order to distinguish the relative location of the capacitor switching. In addition, the transient resonant frequency is to be estimated via the transient disturbance waveform so that the solution of the transient phase difference can be applied to any distribution system without circuit analysis. The cross time-frequency distribution provides time and frequency localized phase difference relation between voltage and current, while the time-frequency distribution provides information for the time and frequency localization of interest in (4.16).

The result of the time-frequency domain solution is illustrated by Figs 4.7-4.8 and Table 4.1. In Fig. 4.7, the time-frequency localized phase difference spectra are provided for 3 different locations of capacitor switching. In each figure, the phase differences are evaluated in terms of $\Theta_{V_1 V_2}$, $\Theta_{I_1 I_2}$, $\Theta_{V_1 I_1}$ and $\Theta_{V_2 I_2}$. In order to provide quantitative information for Fig. 4.7, the phase differences at the frequencies of interest are summarized in Table 4.1. Note that depending on the location of the switched capacitor, the transient resonance frequency will change, because the solution of the characteristic equation is affected by the location of the capacitor. However, using the time-frequency distribution of the transient capacitor switching, one can accurately determine the time and frequency of interest for all cases as illustrated with Fig. 4.3 and (4.16). The frequency of transient oscillation caused by the capacitor switching is indicated by the vertical dashed lines in each cases. (The exact values

of the frequency of interest is tabluated in Table 4.1.)

Utilizing the time-frequency localized phase differences provided in Fig. 4.7, one can map the phase relations into a diagram as illustrated in Fig. 4.2. In Fig. 4.2, the reference of the phase angle is the phase of $v_B(t)$, which is not directly available from the observed waveforms. In this simulation, as $R_{A_3} = R_{B_1}$ and $L_{A_3} = L_{B_1}$, one can take the mean of the phase difference of $\Theta_{V_1 V_2}$; however, it can be properly calibrated, if needed, with knowledge of the line characteristics between V_1 and V_2. In Fig. 4.8, the time-frequency localized phase differences in Fig. 4.7 for Cases A, B and C are provided in terms of phase difference angles of voltages (V_1, and V_2) and currents (I_1, and I_2). It is more informative to represent the phase difference relation as shown in Fig. 4.8 to distinguish relative location of the capacitor switching. Now consider each capacitor switching disturbance by interpreting Figs 4.7-4.8 and Table 4.1.

1. Capacitor A switching (upstream direction)

In Fig. 4.7-(a) the time-localized phase difference spectrum of the capacitor switching A (upstream direction) is provided. By applying the formula provided in (4.16) to the time-frequency distribution one can obtain time (18.78 ms.) and frequency of interest (1.073 kHz) of the capacitor A switching disturbance is indicated in Fig. 4.7-(a) by a vertical dashed line. Note that the vertical scale of the Fig. 4.7-(a) is smaller than the other plots in Fig. 4.7. Resorting to the time domain waveform in Fig. 4.6-(a), it is reasonable, because all the waveforms are closely in-phase. However, the time-frequency localized phase difference in Fig. 4.7-(a) and corresponding Fig. 4.8(a) shows that the both of the currents lag the voltage phase to a small degree, i.e., $\Theta_{V_1 I_1}$=0.0782 rad. and $\Theta_{V_2 I_2}$=0.0460 rad.

2. Capacitor B switching

In Fig. 4.7-(b) the time-localized phase difference spectrum of the capacitor switching B is provided. The frequency of interst for the capacitor B switching is estimated to be 0.9537 kHz. The time-frequency distribution in Fig. 4.3 is the current disturbance waveform $i_1(t)$ of the capacitor B switching event. The phase angle of the current I_1 leads the phase angle of the voltage V_1 by 1.5886 rad., while the phase angle of the current I_2 lags the phase angle of the voltage V_2 by 0.0432 rad. Hence, the corresponding phase relation is presented as in Fig. 4.8-(b), which is close to the phase relation schematic provided in Fig. 4.2-(b).

The phase relation diagram in Fig. 4.8-(b) allows one to quantitatively interpret the time domain disturbance waveform provided in Fig. 4.6-(b) in terms of phase difference. The pair of voltages, V_1 and V_2, are closely in phase ($\Theta_{V_1 V_2}$=0.0779 rad.). Also the voltage and current pair at node 2, V_2 and I_2 are closely in phase ($\Theta_{V_2 I_2}$=0.0432 rad.). However, the current I_1 is out-of-phase with other waveforms, due to the instantaneous inrush current to the capacitor and B exhibits approximately $\pi/2$ rad. phase difference with respect to the current I_2 ($\Theta_{I_1 I_2}$=1.6747 rad.) and voltage V_1 ($\Theta_{V_1 I_1}$=-1.5886 rad.).

3. Capacitor C switching (downstream direction)

As indicated in Fig. 4.8-(c), for capacitor C switching, the currents I_1 and I_2 are nearly in phase ($\Theta_{I_1 I_2}$=-0.1041 rad.), however, out of phase with respect to the voltages V_1 and V_2, which are in turn closely in phase ($\Theta_{V_1 V_2}$=-0.1091 rad.). Hence, both of the phase angles of the currents I_1 and I_2 lead thoes of the voltage V_1 and V_2 as illustrated in Fig. 4.8-(c). Also note to the decrease of the frequency of interest for the capacitor C switching (0.6198 kHz). The reduced frequency of interest of capacitor C switching is associated with the large value of the load resistance.
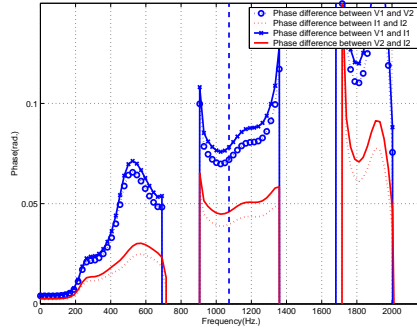
(a) Phase difference relation for Case A
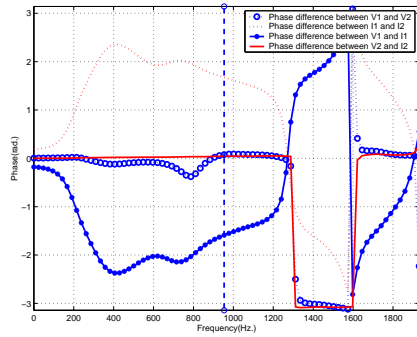
(b) Phase angle relation for Case B
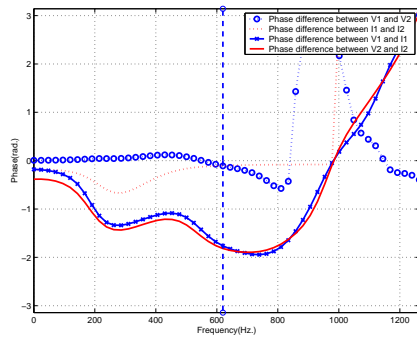
(c) Phase difference relation for Case C

Figure 4.7: Phase difference relation for Case A, B and C in terms of $\Theta_{V_1 V_2}$, $\Theta_{I_1 I_2}$, $\Theta_{V_1 I_1}$, $\Theta_{V_2 I_2}$
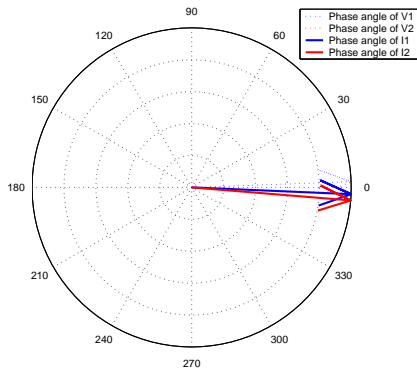
(a) Phase angle relation for Case A
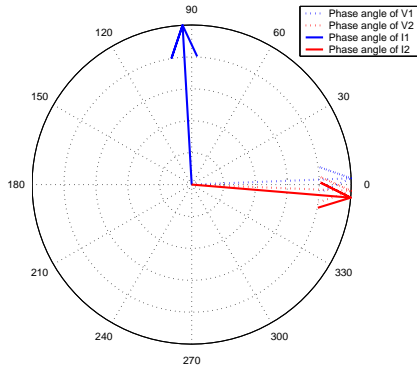
(b) Phase angle relation for Case B
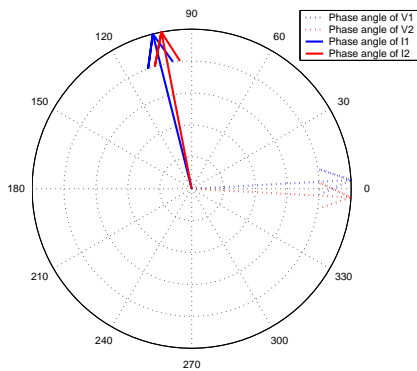
(c) Phase angle relation for Case C

Figure 4.8: Phase angle relation for Case A, B and C

Table 4.1: Time-frequency localized phase difference between voltage and current for different location of capacitor switching

Location	Capacitor A (downstream)	Capacitor B (middle)	Capacitor C (upstream)
$\Theta_{V_1 V_2}$ (rad.)	0.0719	0.0779	-0.1091
$\Theta_{I_1 I_2}$ (rad.)	0.0397	1.6747	-0.1041
$\Theta_{V_1 I_1}$ (rad.)	0.0782	-1.5886	-1.7625
$\Theta_{V_2 I_2}$ (rad.)	0.0460	0.0432	-1.8160
$\omega_f / 2\pi$ (kHz)	1.073	0.9537	0.6198

4.5 Conclusion

This chapter provides a signal processing based general solution to locate transient capacitor switching disturbances. The flow of transient disturbance energy caused by the transient capacitor switching is determined by the time and frequency localized phase difference, which is obtained from the disturbance waveforms only. The key contribution of this study owes to the applications of the cross time-frequency analysis, which provides the required time and frequency localized phase differences, which in turn are used to determine the location of the capacitor switching.

The application and results of the time-frequency localized phase difference approach to the EMTP simulation discussed in this chapter confirms the feasibility of the proposed time-frequency domain methodology. If recording devices for the transient disturbance waveforms are available when applied at several spatial points, the proposed scheme will provide automated and accurate localization of capacitor switching in power distribution systems. The determination of the time and frequency of interest is a strong advantage of the proposed methods, which allows one to identify the location of capacitor switching disturbance, irrespective of location and size of the switching capac-

itor. In this chapter, the discussion and application of the the time-frequency based solution for the location of the transient disturbance is limited to the capacitor switching events only, however, other types of transient disturbance deserve to be investigated by the proposed methodology.

Chapter 5

An Optimal Wavelet Basis Search Algorithm for the Detection of Voltage Sags in Electric Power Systems

5.1   Introduction

The most common type of power quality disturbances at the distribution level is voltage sag [42–44]. In particular, such power system disturbances have a greater impact on customers than ever before, because of the increased use of sensitive electronic equipment [42]. As a result, monitoring and assessment of the power system performance both at the transmission and distribution levels are becoming increasingly important. Moreover, voltage sag analysis is a very complex one, since it is closely related with a large variety of random factors such as types of short-circuits, location of faults, protective system performance, atmospheric discharges, motor starting, etc.[44]. Traditionally, the RMS value and the disturbance duration have been used to characterize the voltage sag waveforms. For some types of equipment, however, more quantitative information on such power quality disturbances may be required to properly assess their impact on the power system performance. In such cases, some additional indices related with the point-on-wave of fault initiation and recovery, unbalance, distortion, and the phase angle shift should be also estimated along with the standard depth and duration values. Thus, to accurately estimate such additional parameters, and to extract some features

necessary to locate the sources of the sag disturbances, an efficient detection scheme for more accurately localizing the source of the sag disturbances is called for.

Recently, as an alternative to the conventional RMS value detection method, wavelet analysis has been utilized for the detection of power quality disturbances including voltage sags [28, 29, 38, 45, 46]. However, the choice of the wavelet basis has a great effect on the end result and the interpretation of the analysis. The precise end of the sag is hard to define, but the recovery phase is usually marked by discernible discrete wavelet transform (DWT) activity. Furthermore, the proper choice of the wavelet basis is key to good performance in detecting the beginning and ending time. This result arises from the well-known fact that trade-offs between time resolution and frequency resolution exists in wavelet analysis.

5.2   Wavelet Analysis and the Uncertainty Principle

Fourier analysis is based on a harmonic basis whose length is infinity. Therefore, Fourier analysis cannot provide time localized information of the signal. However, the wavelet basis produces localized time, and frequency (scale) information. Consider a signal $x(t)$ defined in $L^2(R)$ space which is absolutely integrable, then the continuous wavelet transform (CWT) of $x(t)$ is defined as follows:

$$\text{CWT}_\psi x(a,b) = \int_{-\infty}^{\infty} x(t)\psi_{a,b}^*(t)dt, \tag{5.1}$$

where

$$\psi_{a,b}(t) = |a|^{-\frac{1}{2}}\psi\left(\frac{t-b}{a}\right) \tag{5.2}$$

ψ is the basis function wavelet. Restrict the variables such that $a, b \in R$, and $a \neq 0$. The parameter, a, is a dilation or scale parameter, and b is a translation parameter, respectively. Note that the wavelet transform is function of dilation, and translation, whereas the Fourier transform is function of frequency only.

The discrete wavelet transform is defined by samples of parameters a and b such that $a = a_0^m$ and $b = nb_0 a_0^m$, where a_0 and b_0 are fixed constants under the condition that $a_0 > 1$, $b_0 > 0$, and $m, n \in Z$. The discrete wavelet transform (DWT) is defined as follows:

$$\text{DWT}_\psi x(m, n) = \int_{-\infty}^{\infty} x(t)\psi_{m,n}^*(t)dt \tag{5.3}$$

where the basis function is expressed with discrete variables,

$$\psi_{m,n}(t) = a_0^{-m/2}\psi(\frac{t - nb_0 a_0^m}{a_0^m}) \tag{5.4}$$

The orthonormal wavelet basis $\psi(t)$ function determines the resolution of the coefficients in the time and frequency domain.

Various classes of wavelet basis functions such as Haar, Sinc, Daubechies, Spline, Battle-Lemarie and Meyer are generally used. Each of the wavelet basis functions satisfies conditions for perfect reconstruction, supportness, etc.

Several Daubechies' wavelet basis waveforms are provided in Fig. 5.1. Note that the Daubechies' wavelet with an assigned length 1 is equivalent to the Harr wavelet basis. The time and frequency resolution properties of each wavelet basis changes with different choices of the length; as a result, the wavelet transform of the signal will change depending upon the choice of the wavelet length. However, in many wavelet applications using Daubechies' wavelets, the choice of the Daubechies' wavelet basis is not specified or if it is
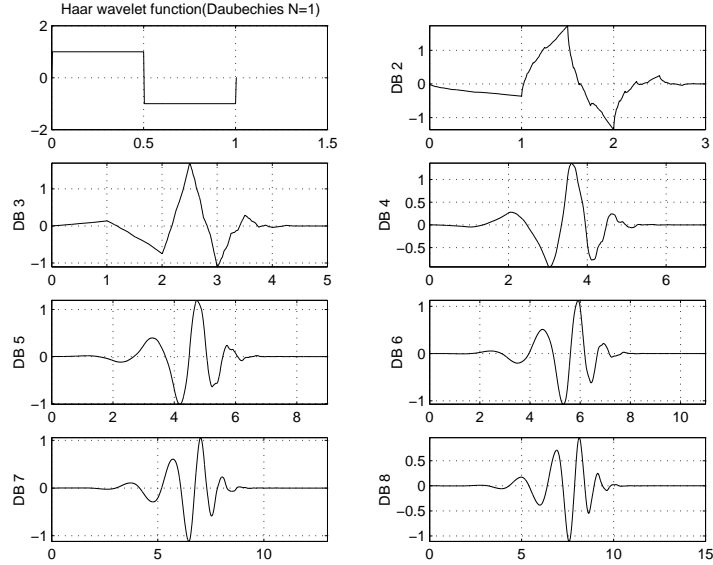
Figure 5.1: Haar wavelet basis and Daubechies' wavelet bases (2 through 8) with different length

provided, the procedure is quite empirical [38]. In this chapter, we will focus on the optimal choice of Daubechies' wavelet for detecting voltage sag signals, as will be described in next section, in terms of time and frequency resolution.

When we deal with time and frequency (or scale) together for localized analysis, the resolution in the time and frequency domains is not arbitrarily available. The trade-off relation between time resolution and frequency resolution is contained in the uncertainty principle [47].

Define a signal with localization window $h(t)$, such that $x(t) = s(\tau)h(\tau - t)$, then we can define frequency localization characteristic parameters, the center frequency f_m and the frequency bandwidth F, as follows [48]:

$$f_m = \frac{1}{E_x} \int_{-\infty}^{\infty} \nu |X(\nu)|^2 d\nu \qquad (5.5)$$

93

$$F = 2\sqrt{\frac{\pi}{E_x} \int_{-\infty}^{\infty} (\nu - f_m)^2 |X(\nu)|^2 d\nu} \qquad (5.6)$$

where $X(\nu)$ is the Fourier transform of the localized signal $x(t)$. Similarly, the time localization parameters are defined by a mean time t_m and a time duration T, as follows:

$$t_m = \frac{1}{E_x} \int_{-\infty}^{\infty} t |x(t)|^2 dt \qquad (5.7)$$

$$T = 2\sqrt{\frac{\pi}{E_x} \int_{-\infty}^{\infty} (t - t_m)^2 |x(t)|^2 dt} \qquad (5.8)$$

where E_x is the energy of the signal. Then the uncertainty principle boundary constant will be changed to the following inequality.

$$F \cdot T \geq 1 \qquad (5.9)$$

In this chapter, we will use the notations in equations (5.6) and (5.8) for convenience. Therefore, the time duration (T) specifies the characteristics of time localization, and the frequency bandwidth (F) specifies the characteristics of frequency localization.

5.3 Voltage Sag Detection in Power Transmission and Distribution

Voltage sag occurs at both the transmission and distribution levels in power systems. The voltage level, which is supposed to be maintained constant, and the frequency, which is supposed to be maintained at 60Hz, change. The detection of the sag and estimation of the voltage sag starting time is especially important. Three sets of real world voltage sag waveforms on a high voltage transmission line provided by the Electric Power Research Institute (EPRI) are shown in Fig. 5.2. The full data set consists of 25 typical voltage

sag signals whose sampling rate is 6 kHz which is also a typical sampling rate for monitoring. In the rest of the chapter, we assume the sampling rate 6 kHz and 60 Hz for fundamental frequency.

Wavelet analysis has shown excellent potential in detecting the voltage sag in power systems [49]. Concerning the wavelet basis, the optimal wavelet packet searching algorithm based on the concept of entropy is provided in [50]. However, for a specified scale, the optimal length of wavelet basis is not yet specified. Among the many samples of the voltage sag time series, we choose a typical voltage sag waveform, label with data 109, and its wavelet transform with different Daubechies' wavelet bases (2-8) are shown in Fig. 5.3. In this chapter, the scale is set equal to 1 that covers the highest frequency range. It is reasonable to set the scale equal to 1, if we are focusing on the detection of sag, because the beginning of the sag will involve higher frequency components. In this chapter, we will utilize sag data 109 for explaining the detailed procedures, however, the results based on exactly the same procedures will be provided at the end of the chapter for 22 more real world data sets including data 101, and data 102 shown in Fig. 5.2.

From Fig. 5.3, our mission concerning the optimal wavelet basis search is clarified. The correspondences of the uncertainty principle relation are vivid in Fig. 5.3. The wavelet bases with short length (DB 2 and DB 3) show good time resolution. However, due to the corresponding poor frequency resolution of the short length (DB 2 and DB 3) wavelet bases, the amplitude of coefficients are often not high enough for detection. As the length of the Daubechies' wavelet increases, the frequency resolution increases, but the poor time resolution degrades the temporal resolution of the coefficients.

The optimal wavelet basis for voltage sag detection should provide *the highest signal-to-noise ratio within a short time frame* for more accurate

95
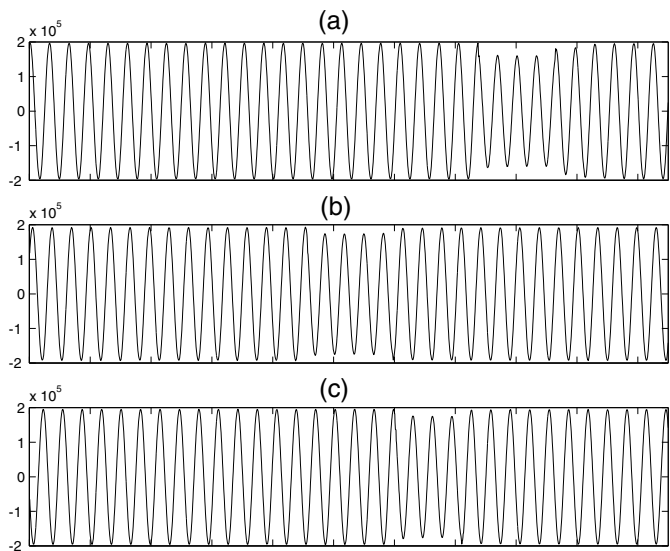
Figure 5.2: Voltage sag time series data (Data 101, Data 102, Data 109)
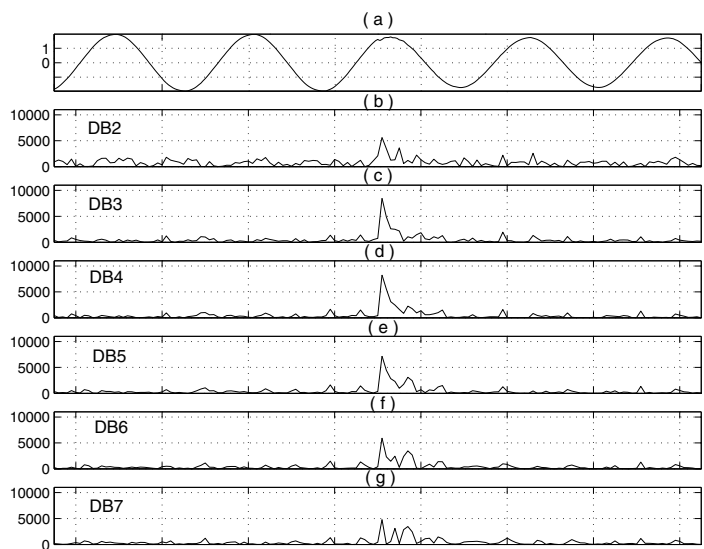
Figure 5.3: Voltage sag time series data (Data 109) and its discrete Daubechies wavelet transforms for DB 2 through DB 7

96

detection. Reflecting on this fact, from the several results in Fig. 5.3, one might intuitively choose a desirable wavelet basis like DB3, DB4 or DB5, by inspection. However, this is a quite difficult decision, because, one must deal with time resolution and frequency resolution together within the uncertainty principle constraints. We will provide a systemetic and quantitative measure of the relation between the wavelet basis and voltage sag signals in the following sections.

5.4 Measure of Similarity for Signal and Basis : Instantaneous Signal-to-Noise Ratio (SNR)

In this section, we will discuss how one can measure the *"goodness"* of a basis function for a given signal to be detected. Before we expand our discussion on wavelet basis and voltage sag signals, let us consider a simple but general case of basis function and signal. The *"goodness"* of the basis can be explained by the degree to which the basis and the signals are highly correlated for a short time period.

In Fig.5.4, a set of basis functions are presented in (a) and their correlation with signal S_1 is provided in (b). Assume that signal is S_1 (indicated in dotted line) rectangular waveform whose duration is τ_s=100. Different basis functions are also indicated $B_i(\tau_s - \tau_{b_i})$ in Fig. 5.4-(a), where τ_s and τ_{b_i} are the duration of the signal s and basis b_i. Note that the set of basis functions are all designed to be centered at zero, have a rectangular shape and contain the same energy. The cross correlation results are provided in Fig. 5.4-(b). The cross correlation plotted in Fig. 5.4-(b) can be expressed as follows:

$$c(t) = \int_{-\infty}^{\infty} s_1(\tau)B_i(t + \tau)d\tau \tag{5.10}$$

97
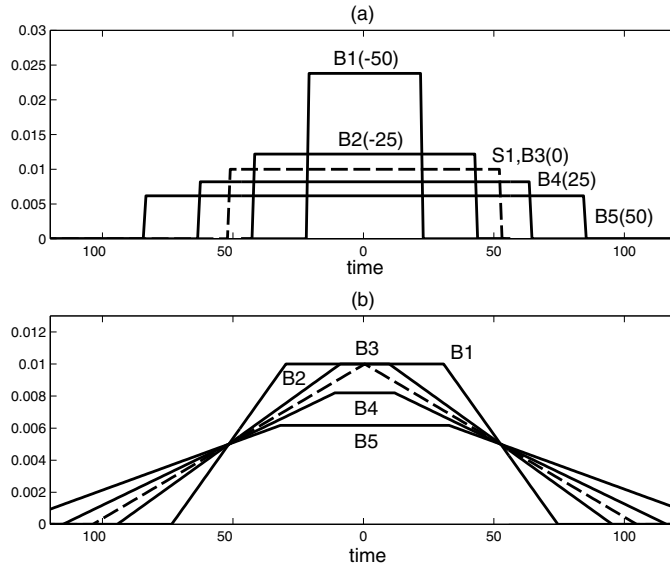
Figure 5.4: A set of basis functions (a) and corresponding correlation function with signal (b)

In Fig. 5.4-(b), the basis $B_3(0)$ which is identical with the signal is indicated by the dotted line. The cross correlation function of B_3 provided in Fig. 5.4-(b) shows a sharp peak at the center of the signal which corresponds to the matched filter theory.

These set of cross correlation results can be explained by frequency bandwidth (F) and time duration (T), defined in (5.6) and (5.8), respectively. Based on the uncertainty principle in (5.9), the equality is satisfied when the signal is Gaussian. Therefore, for a given F and T, we will approximate the individual time-frequency signal elements as a two-dimensional Gaussian distribution on the time-frequency plane. Then the trace of the signal elements on the time-frequency plane will be a elliptic curve whose semimajor and semiminor are also determined by F and T. This approximation is adopted from [51] where the time and frequency characteristics are treated together on the
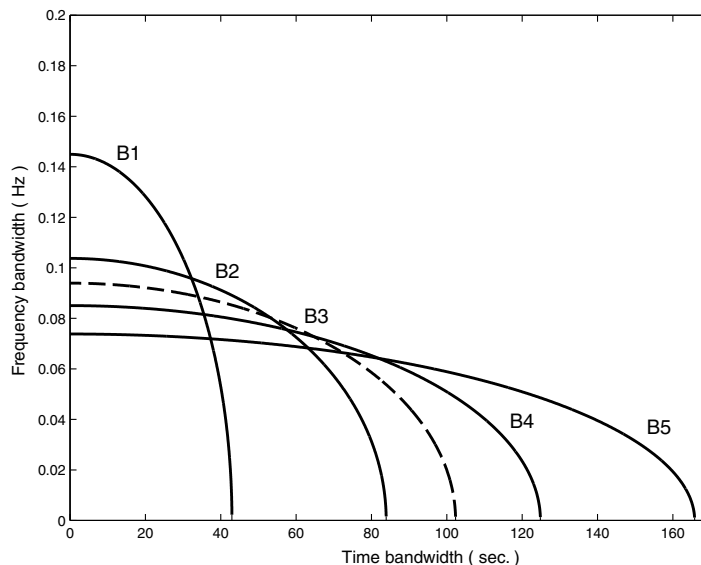
Figure 5.5: FT characteristics of basis $(B_1, B_2, B_3 \text{ and } B_4)$ and signal (S_1)

time-frequency plane.

The F and T characteristics of various basis functions and the B_3 signal are provided in Fig. 5.5. The main pattern of the F and T characteristics is as follows: the shorter basis has smaller time duration, but larger frequency bandwidth. The longer basis has larger time duration, but smaller frequency bandwidth.

How can one quantitatively express the relation between signal and basis? In Fig. 5.6, an example of a pair of F and T characteristics is provided. The equations of the curves are as follows: $r_s(\theta) = \sqrt{T_s^2 \cos^2 \theta + B_s^2 \sin^2 \theta}$ for signal characteristics and $r_b(\theta) = \sqrt{T_b^2 \cos^2 \theta + B_b^2 \sin^2 \theta}$ for basis characteristics. Then, the common area determined by the two ellipses corresponds to the similarity between the signal and basis in the sense of time and frequency. The discrepancy area corresponds to the mismatch between the signals which is also reflected on the cross correlation but which is undesirable for higher

99
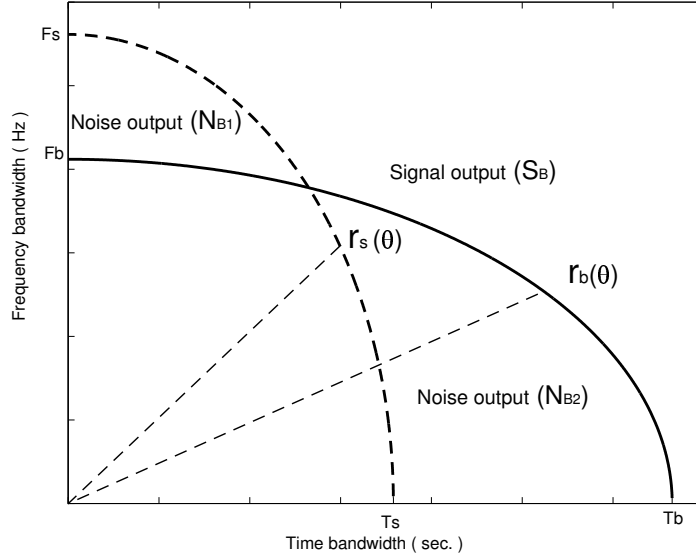
Figure 5.6: Signal (solid line) and noise (dashed line) determination from FT characteristics

resolution results. Then one can define signal (S_B) and noise (N_B) between signal and basis as follows:

$$S_B = \int_{\theta=0}^{\theta=\pi/2} \int_{r=0}^{r=\min(r_b,r_s)} r\,dr\,d\theta \qquad (5.11)$$

$$N_B = N_{B_1} + N_{B_2} = \int_{\theta=0}^{\theta=\pi/2} \int_{r=\min(r_b,r_s)}^{r=\max(r_b,r_s)} r\,dr\,d\theta \qquad (5.12)$$

Note that the resolution index in this chapter is to provide transient time-frequency resolution of the basis against a given signal. Therefore, the measure of resolution (SNR) is to be confined within the time frame of the basis which is determined by the time duration of the basis T_B. Considering all the aspects of the basis and signal discussed above, we postulate the the following transient resolution index named "instantaneous SNR" whose dimension is dB/sec.:

$$\text{dB/sec.} = \frac{1}{T_B} 10 \log_{10}(\frac{S_B}{N_B}) \qquad (5.13)$$

This index provides a measurement of similarity and mismatch between the signal and basis within the time frame of the basis function.

The set of simulations discussed in Sec. 5.4 can be re-interpreted in terms of the index provided in (5.13). In Fig. 5.7, the variations of S_B, N_B and T_B with the duration of the basis (τ_{B_i}) are provided in (a) and the corresponding instantaneous SNR is provided in (b). Both of the figures are a function of the differences of the time duration, $\tau = \tau_s - \tau_{b_i}$. As we assumed identical waveform and duration, S_B is maximum and N_B is minimum at the center, while S_B drops and N_B increases as the duration difference increases. Note that the calculation is based on the F and T characteristics and (5.11), (5.12). Reflecting on the definition of index in (5.13), the higher index indicates higher local resolution. This implication is clearly shown in Fig. 5.7. At the identical basis the index approaches infinity while the index drops down as the discrepancy increases.

In this section, an important local resolution index is defined and also explained by a simple set of signal simulations. The interpretation of the index and its applicability is clarified. In the following sections, a similar systemetic approach will focus on real voltage sag signals and various wavelet bases to answer which wavelet basis provides the highest local resolution.

5.5 Uncertainty Analysis for Voltage Sags and Daubechies' Wavelet Bases

We have discussed the general aspects of signals' similarity and we derived an important parameter (instantaneous SNR) to measure the similarity between a signal and a basis function. We will now expand the general discussion to the voltage sag signal sets and the Daubechies' wavelet basis family.
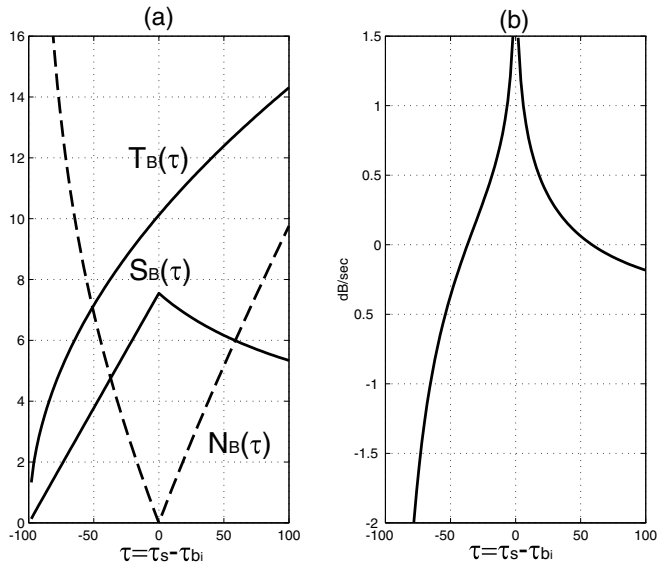
Figure 5.7: Parameters (signal and noise) for instantaneous SNR in (a) and its instantaneous SNR in (b)

The ultimate goal of this chapter and section is to provide a quantitative recommendation for optimal Daubechies' wavelet basis for detection of voltage sags.

We consider data sample 109 to illustrate the approach. First of all, the localizing characteristics of the wavelet basis can be described by the time duration (T) and frequency bandwidth (F) of the Daubechies' wavelets. One can calculate the local time-frequency properties of the voltage sag signal in the neighborhood of the sag starting point. For the portion of the starting of the sag, the localized time-frequency properties of data 109 are provided in Fig. 5.8. This enables us to compare the localized properties of the wavelet basis and the voltage sag on the uncertainty plane together. The number N stands for the degree of the localization of the voltage sag. That implies we want to localize the voltage sag to within N samples. The rectangular win-
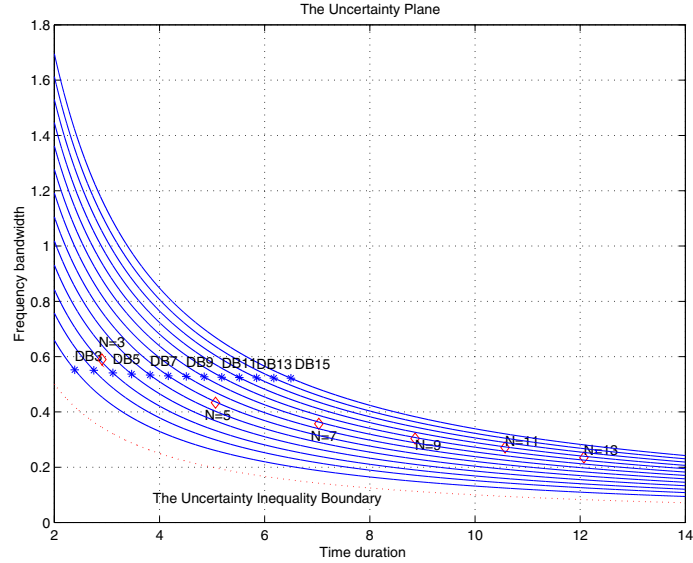
Figure 5.8: Localized time-frequency FT characteristics of wavelet basis (DB 3-DB 15) and voltage sag signal (Data 109)

dow length N is applied to get localized information of the voltage sag in this application.

In Fig. 5.8, the *FT* characteristics of the wavelet basis and voltage sag are provided, however, we cannot describe an exact relation between wavelet basis and voltage sag. It is necessary for us to provide a quantitative measure to compare the *FT* relation of the wavelet basis and the voltage sag. For the window length, we choose $N = 3$ which is nearest to the *FT* clusters of the basis.

For the voltage sag event 109 with $N = 3$ and Daubechies' wavelet basis family, *FT* elliptical approximations of the signal elements are provided in Fig. 5.9. The solid line traces are the *FT* time-frequency characteristics of the wavelet bases with different length (DB2-DB7) where the dashed line traces are that of the localized voltage sag signal. In Fig. 5.9, one can intuitively

103
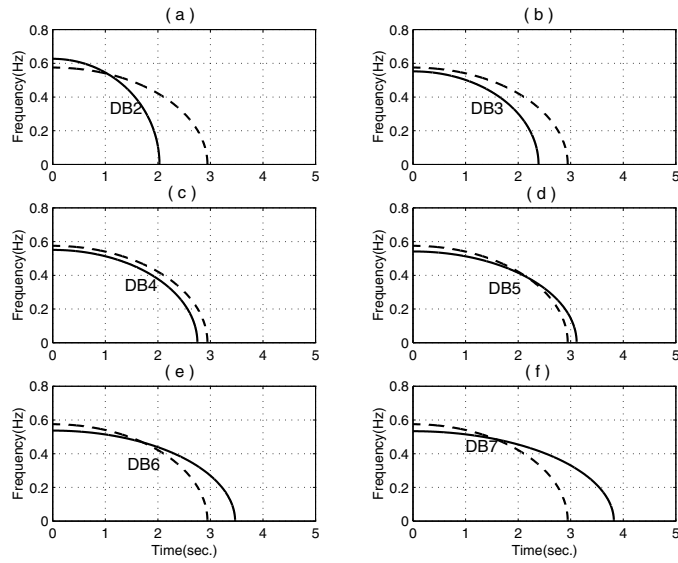
Figure 5.9: Plots of the FT characteristics of the voltage sag signal data 109 (N=3), and Daubechies' wavelets 2,3,4,5,6 and 7. (The solid line is for the basis and the dashed line is for the signal)
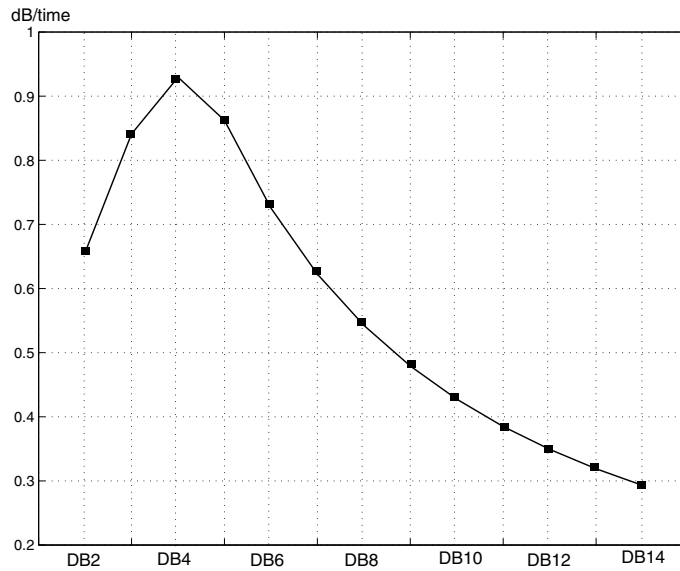
Figure 5.10: Plots of the dB/sec. between Sag 109 and Daubechies wavelet bases (DB2∼DB14)

104
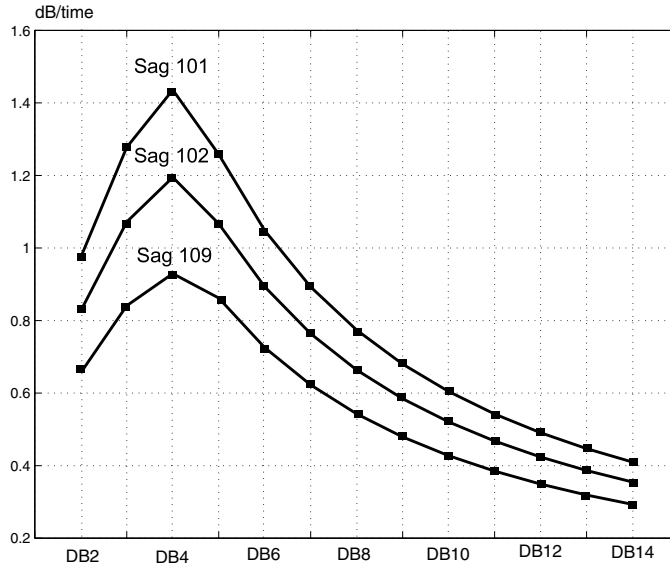
Figure 5.11: Plots of the dB/sec. between Sags (101, 102, and 109) and Daubechies wavelet bases (DB3~DB14)

observe that the *FT* characteristics are becoming better matched for DB4 and DB5.

Using the definition of the instantaneous SNR in (5.13), one can obtain a quantitative relation between the various bases functions and signal to be detected. The instantaneous SNR for the wavelet bases and voltage sag signal is provided in Fig. 5.10. By comparing Fig. 5.10 and Fig. 5.9, one can confirm how the instantaneous SNR describes the degree of match between the various bases and the signal to be detected. For the case of Sag 109, the optimal wavelet basis is DB4, which shows the highest instantaneous SNR among the bases functions. Even further, by comparing Fig. 5.9 and Fig. 5.3, one can find the implication of the instantaneous SNR: DB3 and DB4 show clear high peaks for detection. Therefore we can recommend that DB4 is the best basis for the detection of the voltage sag event 109 on a quantitative basis.
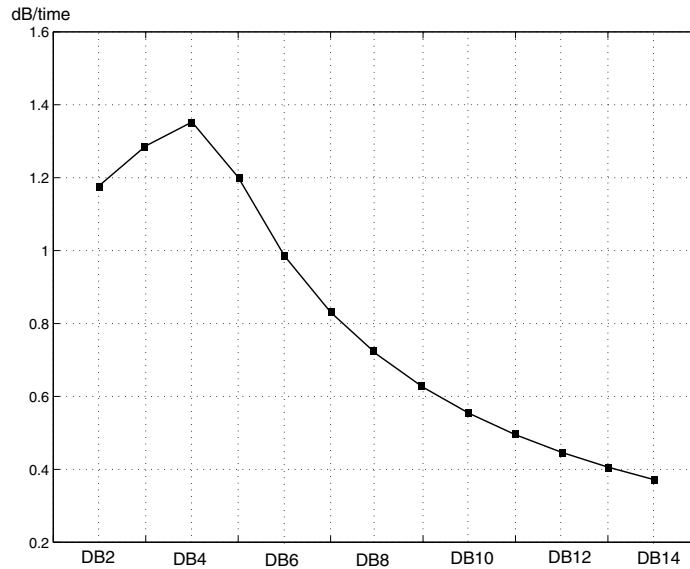
Figure 5.12: Average dB/sec. plot of 25 voltage sag samples and Daubechies wavelet bases (DB2∼DB14)

We can extend the discussion of the basis function to other voltage sag event. The instantaneous SNR of the 3 voltage sag events shown in Fig. 5.2 are provided in Fig. 5.11. The values of peak instantaneous SNR are slightly different depending on the events, however, the main pattern of the instantaneous SNR is similar- peak instantaneous SNR for DB4 and the instantaneous SNR decreases as length of the bases increase or decrease.

Including the 3 examples shown in Fig. 5.11, the average instantaneous SNR of 25 typical samples of voltage sag is provided in Fig. 5.12. Now we can recommend DB4 as a best basis for detection of the voltage sag. However, note that DB 3 and DB 5 bases are also good candidate for detection of the sag in quantitative basis. This procedure and algorithm can be extended to different applications of the signal detection in order to identify the best basis on a "quantitative" basis in terms of the instantaneous SNR.

106

5.6 Conclusion

We have provided a methodology to find an optimal Daubechies' wavelet basis for voltage sag signals. The parameters for the algorithm are based on the second order statistics from the time-frequency analysis, the time duration (T) and frequency bandwidth (F). Our index, instantaneous SNR, to describe the relation between the wavelet basis function and the voltage sag signal provides a quantitative measure for the time, frequency resolution mechanism within the uncertainty principle. For a typical case of voltage sag, the optimal Daubechies wavelet basis turns out to be Daubechies 4, although Daubechies 3 or 5 will work almost as well. This algorithm is not restricted to voltage sag detection cases and Daubechies' wavelet basis. The objective signal can be any type of disturbance signal to be detected, and other types of wavelet bases such as Battle-Lemarie, spline, etc. can be considered with this algorithm.

Chapter 6

Application of Time-Frequency Domain Reflectometry for Detection and Localization of a Fault on a Coaxial Cable

6.1   Introduction

The importance of aging electrical wiring and associated faults in aircraft has been highlighted in [52]. This problem is not limited to aircraft only but also includes systems where complicated wiring is involved and high safety is required such as the space shuttle, nuclear power plants and very tall buildings [53]. Thus, the detection and localization of faults with high accuracy is required for diagnosis and maintenance of wiring systems. In addition, the detection of faults and imperfections in wiring and cables used in communication systems is also of importance.

The state-of-art for wiring/cable fault detection can be categorized by time domain analysis and frequency domain analysis. In time domain analysis, time domain reflectometry (TDR) [54] is used, whereas in frequency domain analysis, frequency domain reflectometry (FDR) [55] and standing wave reflectometry (SWR) [56] are utilized. Each methodology is based on the appropriate analysis of the reference signal and reflected signal either in the time or frequency domain *only*. However, in this chapter, detection and location of coaxial cable faults by the use of joint time-frequency analysis is discussed.

Time domain reflectometry (TDR) [57] and frequency domain reflec-

tometry (FDR) are well-known, conventional methods which have been applied to various types of applications including the cable test [58], network analyzer [59] and measurement of characteristic impedance [60], [61], etc. Recently, modern TDR instruments have been used for failure analysis and signal integrity characterization of high speed circuit boards [62], wiring packages, sockets, connectors, cable interconnects and even power electronic devices [63], etc. However, the resolution and accuracy of the TDR and FDR are limited by the rise/fall time and frequency sweep bandwidth, respectively. To enhance the resolution of TDR, a time-to-digital conversion technique has been introduced for application to coaxial cables [64]. To enhance the accuracy in reflectometry, digital signal processing techniques, e.g., the "cepstrum", has been suggested for TDR [65] and "cisoids" have been applied to FDR [66]. Recently, the problem of TDR waveform distortion has been investigated by the approximation of the skin effect to enhance accurate localization of a fault in cables [67]. However, the distortion of the TDR pulse is an inherent problem in TDR for accurate detection and localization of a fault.

In TDR a step pulse is applied to the wire/cable under test, which is then reflected by any faults present. The time it takes for the reflected signal to make a round trip can then be converted to distance from the knowledge of the velocity of propagation. Since the energy of the pulse is spread over a broad frequency range, TDR is usually not suitable for investigating the RF properties of a cable, which is important, for example, when dealing with wires/cables used for communication purposes. On the other hand, FDR often uses a swept frequency signal which allows one to place the energy of the reference or probing signal in the RF band of interest.

In this chapter we introduce a joint time-frequency domain reflectometry (TFDR) technique which captures many of the advantages of TDR and

109

FDR mentioned previously. The reference signal is a (linear with time) chirp signal which allows one to apply the RF power in the band of interest. To provide time localization, the chirp signal is multiplied by a Gaussian envelope in the time domain. The time-frequency distributions [1] of the reference signal and the reflected signals are calculated. Then these two time-frequency distributions are cross-correlated in the time-frequency domain. The peak in the time-frequency cross correlation function allows one to estimate an accurate round-trip propagation time and, hence, distance, as in classical TDR. Yet, the experiment is carried in an RF band of interest which is relevant for the particular wire/cable under test, as in FDR. If frequency-dependent phenomena, such as dispersion, lead to substantial distortion of the reflected signal, these effects can be mitigated by reducing the frequency bandwidth of the reference signal.

6.2   Time-Frequency Domain Reflectometry

In this section, the basic idea of time-frequency domain reflectometry (TFDR) is presented. To begin with, let us compare this new reflectometry methodology with traditional reflectometry methodologies. Fig. 6.1 schematically depicts reference signals for time domain reflectometry (TDR), frequency domain reflectometry (FDR) and time-frequency domain reflectometry (TFDR) on a time-frequency plane. As suggested in Fig. 6.1, TDR uses a pulse with fixed time duration and compares the reference and reflected signals in the time domain only. Therefore, TDR can not analyze the signal in the frequency domain because an ideal step pulse has its energy spread over a wide range of frequencies at the time instance of the step. On the other hand, FDR uses a set of sinusoidal signals with fixed frequency bandwidth and analyzes
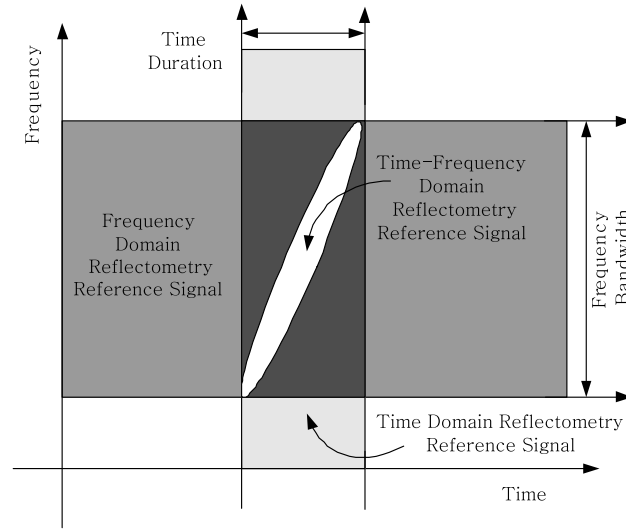
Figure 6.1: Schematic comparison of time domain reflectometry (TDR), frequency domain reflectometry (FDR) and time-frequency domain reflectometry (TFDR).

the change of the signal in the frequency domain only. As a result, it is difficult to analyze the signal in time domain by FDR because a pure sinusoidal signal, which is a reference signal in FDR, has, in principle, infinite time duration.

Therefore, instead of traditional TDR and FDR, we propose a new type of reflectometry, time-frequency domain reflectometry. TFDR uses a linearly modulated chirp signal with a Gaussian envelope. The proposed reference signal is written as follows:

$$s(t) = (\alpha/\pi)^{1/4} e^{-\alpha(t-t_0)^2/2 + j\beta(t-t_0)^2/2 + j\omega_0(t-t_0)} \qquad (6.1)$$

where α, β, t_0 and ω_0 determine the time duration, frequency sweep rate, time center and frequency center, respectively. The Gaussian envelope localizes the reference signal in the time and frequency domain while the instantaneous frequency of the signal increases with time in a linear manner as depicted in Fig.

111

6.1.

In other aspects, the time-frequency domain reflectometry can be regarded as a generalized reflectometry methodology. Refer to Fig. 6.1: time-frequency domain reflectometry can be characterized by time and frequency localization as a mixture of time domain reflectometry and frequency domain reflectometry. For example, under the conditions $\beta = \omega_0 = 0$ and α is very large for the chirp signal in (6.1), the reference signal of the time-frequency domain reflectometry takes on a pulse-like character reminiscent of the reference signal of TDR. Similarly, for α very small, the reference signal of the time-frequency domain reflectometry corresponds to the swept sinusoidal reference signal of FDR. Therefore, the time-frequency domain reflectometry scheme provides flexible application depending on the physical characteristics of the wire or cable under test.

The appropriate determination of the four signal parameters for a specific application is very important in TFDR. The design of the reference signal that fits the physical characteristics of the RG type coaxial cable used in the experiments and post processing of the reflected signal for detection and localization will be addressed in the next subsections.

6.2.1 Design of Reference Signal

The central idea of time-frequency domain reflectometry is to design a reference signal that "fits" the physical characteristics of the target wire or cable in the time and frequency domain. Consider the proposed reference signal in (6.1). In Eqs. (6.2)-(6.6) we describe several properties of this signal given in [1]. For this signal, one can evaluate the time center (t_s) and the time

112

duration (T_s) as follows:

$$t_s = \int t|s(t)|^2 dt = t_0,$$

$$T_s^2 = \int (t - t_s)^2 |s(t)|^2 dt = \frac{1}{2\alpha} \tag{6.2}$$

The Fourier transform of the chirp signal in (6.1) is obtained as follows:

$$S(\omega) = \sqrt{\frac{\sqrt{\alpha}}{\sqrt{\pi}(\alpha - j\beta)}} e^{-(\omega - \omega_0)^2/2(\alpha - j\beta)} \tag{6.3}$$

Similarly, the frequency center (ω_s) and bandwidth (B_s) can be evaluated in terms of $S(\omega)$ as follows:

$$\omega_s = \int \omega |S(\omega)|^2 d\omega = \omega_0,$$

$$B_s^2 = \int (\omega - \omega_s)^2 |S(\omega)|^2 d\omega = \frac{\alpha^2 + \beta^2}{2\alpha} \tag{6.4}$$

Consider the Wigner time-frequency distribution of the time signal $s(t)$ obtained by following transformation:

$$W(t, \omega) = \frac{1}{2\pi} \int s^*(t - \frac{1}{2}\tau) s(t + \frac{1}{2}\tau) e^{-j\tau\omega} d\tau \tag{6.5}$$

Then the Wigner distribution of the reference signal $W_s(t, \omega)$ is

$$W_s(t, \omega) = \frac{1}{\pi} e^{-\alpha(t-t_0)^2 - (\omega - \beta(t-t_0) - \omega_0)^2/\alpha} \tag{6.6}$$

Equation (6.6) indicates how the energy in the reference signal is distributed over the time and frequency plane as indicated schematically in Fig. 6.1.

In order to apply the reference signal to the coaxial cables used in the experiment, the parameters of the signal are to be selected with consideration of the attenuation characteristics of the coaxial cables. The selection of the parameters take the following order:

113
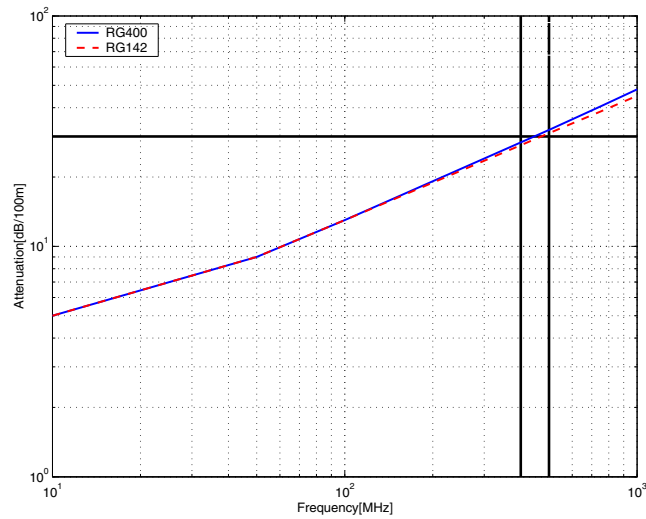
Figure 6.2: Frequency-dependent attenuation characteristics of RG 142 (dotted line) and RG 400 (solid line) type coaxial cables in dB per 100 m. The frequency region of interest is indicated by the two solid vertical lines: 400 MHz $\sim$ 500 MHz.

- **Step 1.** Determine center frequency : (ω_0)

- **Step 2.** Determine frequency bandwidth : (B_s)

- **Step 3.** Determine time duration : (T_s)

Step 1. Center Frequency : The center frequency of the reference signal determines the degree of attenuation of the reference signal through the cable, since attenuation increases with frequency. Thus, one must consider a trade off, since higher frequencies allow higher spatial resolution with shorter wavelengths, but suffer more severe attenuation. Considering the noise sensitivity of the experimental setup, we find we can tolerate a round-trip attenuation of 24dB. The maximum fault distance in this set of experiments is 40 m, so the maximum signal attenuation is 24dB/40 m or 30 dB/100m. From Fig. 6.2, we

114

see that the horizontal line of 30 dB/100m intersects the attenuation curves at approximately, 450 MHz, which we then select as our center frequency of the reference signal. Obviously, in the general case, the procedure used to select the center frequency will depend upon the the attenuation characteristics of the system under test, or possibly other RF characteristics of interest.

The selection of the center frequency for the reference signal also can be interpreted in terms of energy. Assign P_{rec} as the signal power of the reflected signal and P_{tran} as the signal power of the transmitted, i.e., reference signal. Then the ratio of the P_{rec} to P_{tran} can be defined by the attenuation characteristics of the cable per unit length $A(\omega)$ such that

$$P_{rec} = P_{tran}/A(\omega) \tag{6.7}$$

In dB scale calculation,

$$[P_{rec}] = [P_{tran}] - [A(\omega)], \tag{6.8}$$

Normalize the power of the reference signal such that $[P_{tran}]$=0dB. Then, the power of the received signal is,

$$
\begin{aligned}
[P_{rec}] &= [P_{tran}] - [A(\omega)], \\
&= -[A(\omega)] \\
&= -[A(\omega)/2d] \times 2d \tag{6.9}
\end{aligned}
$$

where d is the maximum length of cable under test. Assume that the minimum required power of the reflected signal at the terminal is -24dB,

$$[P_{rec}] = -[A(\omega)/2d] \times 2d \geq -24\text{dB} \tag{6.10}$$

where the maximum length of cable under test is 40 m in this experiment. Hence,

$$[A(\omega)/2d] \leq \frac{24\text{dB}}{80\text{m}} = 30\text{dB}/100\text{m} \tag{6.11}$$

115

Referring the frequency dependent attenuation characteristics provided in Fig. 6.2 for 30dB/100m, the center frequency of the reference signal f_0 should be selected such that

$$f_0 \leq 450\text{MHz} \tag{6.12}$$

Step 2. Frequency Bandwidth : The experimental frequency bandwidth of the chirp signal generation is limited to the performance of the signal generator and circulator (100 MHz in experiment described this chapter) which isolates the signal reflected from the fault. As a result, the frequency bandwidth of the chirp signal is limited by 100 MHz so that the frequency range of interest is selected as 400 MHz ∼ 500 MHz as indicated in Fig. 6.2.

Step 3. Time Duration : The performance of the signal generator in terms of rise/fall time and frequency sweep capacity limit is 25 ns. in this chapter. In order to meet the selected parameters (center frequency and frequency bandwidth) selected above, the time duration of the reference signal is selected to be 50ns. We note that in time-frequency analysis the uncertainty principle places a constraint on the best time and frequency localization that can be achieved simultaneously. Observe that the product of frequency bandwidth B_s and time duration T_s in this experiment is equal to 10π and therefore does not violate the uncertainty principle stated in (1.2).

In a summary, the following parameters of the chirp signal (6.1) will be applied to the coaxial cable as a reference signal.

- Center Frequency : $\omega_0/2\pi$=450 MHz

- Time Duration of Chirp : 50 ns.

- Frequency Bandwidth : 100 MHz (400MHz ∼ 500MHz)
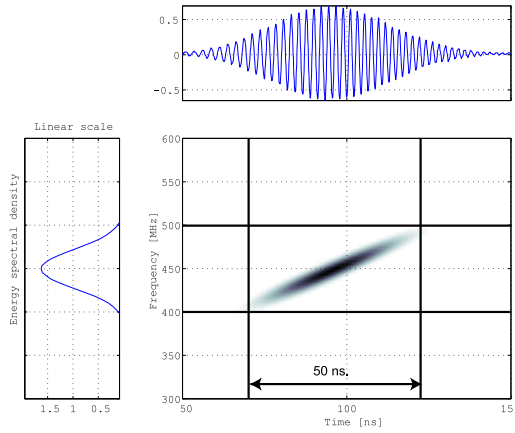
Figure 6.3: Time-frequency distribution of the designed reference signal for RG type coaxial cables. The top plot is the reference signal time waveform, and the left hand plot is its corresponding energy spectrum.

- Frequency Sweep Rate: Linear increasing $(\beta/2\pi = \dfrac{100\text{MHz}}{50\text{ns}})$

In Fig. 6.3, the designed time-frequency distribution of the experimental reference signal for RG type coaxial cable is provided. Also shown at the top is the time waveform of the Gaussian chirp signal and on the left its energy spectrum. As shown in Fig. 6.3, the reference signal provides time localization within 50 ns while the frequency is also localized between 400 MHz and 500 MHz.

In this chapter, the design of the reference signal is customized for RG type coaxial cables up to 40 meters in length, however, for longer distance testing, the time duration of the signal is to be increased while the center frequency is to be decreased so that the reference signal suffers less attenuation by the wire or cable under test. If a longer testing distance is required, one can design the reference signal in the time-frequency domain by following the

reference signal design procedures. The flexibility in designing reference signal in TFDR also allows one to minimize frequency-dependent distortion of the reflected signal by assigning a relatively narrower frequency bandwidth.

6.2.2 Detection and Localization by Time-Frequency Cross Correlation Function

For a successful detection and localization of a fault in RG type coaxial cable, it is necessary to model the propagation of the reference signal in the media which allows one to determine the properties of the signal reflected from the fault in the coaxial cable.

Consider the spatial propagation and reflection of the time-frequency domain reference signal. As the signal propagates along the media with spatial variable x, the waveform will be changed by the transfer function of the media $H(\omega, x)$. For convenience of calculation, let the time center of the reference signal be $t_0 = 0$ without loss of generality. Let $u(x, t)$ be a waveform that is observed at a distance, x, for a given initial condition, $u(x = 0, t) = s(t)$, then, the general solution of the $u(x, t)$ is,

$$u(x, t) = \frac{1}{\sqrt{2\pi}} \int S(\omega, x) e^{-j\omega t} d\omega \tag{6.13}$$

where

$$S(\omega, x) = S(\omega, x = 0) \cdot H(\omega, x) = S(\omega, x = 0) e^{-(\alpha(\omega) - jk(\omega))x} \tag{6.14}$$

and where $H(\omega, x)$ is the transfer function of the medium which is characterized by the frequency-dependent attenuation $\alpha(\omega)$ and wave number $k(\omega)$ [68]. Note that the frequency-dependent attenuation $\alpha(\omega)$ is not to be confused with the parameter α in (6.1). In the following we assume linear frequency-dependent attenuation, $\alpha(\omega) \simeq A\omega$, and dispersion, $k(\omega) \simeq K\omega$. For the latter

118

case, note that both the phase (ω/k) and group $(\partial\omega/\partial k)$ velocities are both equal to $1/K$ and will, henceforth, be simply denoted by v, the velocity of propagation. The assumption of a dispersionless media is particularly suitable for the coaxial cable experiments considered later in this chapter.

Consider, the time center $(t_{u(x)})$ and frequency center $(\omega_{u(x)})$ of the signal $u(x,t)$ with the assumptions that $\alpha(\omega) \simeq A\omega$ and $k(\omega) \simeq K\omega$. First of all, evaluate frequency center $(\omega_{u(x)})$ of the signal $u(x,t)$ with the propagation distance x,

$$
\begin{aligned}
\omega_{u(x)} &= \int \omega |S(x,\omega)|^2 d\omega \\
&= \int \omega |S(\omega,0)|^2 |H(\omega,x)|^2 d\omega \\
&= \sqrt{\frac{\alpha}{\pi(\alpha^2+\beta^2)}} C^2 \int \omega e^{-\alpha\frac{(\omega-\omega_0)^2}{(\alpha^2+\beta^2)}-2A\omega x} d\omega \\
&= \frac{1}{\sqrt{2\pi}\sqrt{\frac{\alpha^2+\beta^2}{2\alpha}}^2} \int \omega e^{-\frac{[\omega-(\omega_0-\frac{\alpha^2+\beta^2}{\alpha}Ax)]^2}{2[\sqrt{\frac{\alpha^2+\beta^2}{2\alpha}}]^2}} d\omega \\
&\qquad \left(\text{where } C^2 = e^{2\omega_0 Ax - \frac{\alpha^2+\beta^2}{\alpha}A^2 x^2}\right) \\
&= \omega_0 - \frac{\alpha^2+\beta^2}{\alpha}Ax \\
&= \omega_0 - \delta\omega \qquad\qquad\qquad\qquad\qquad (6.15)
\end{aligned}
$$

The frequency offset $\delta\omega$ is proportional to the frequency bandwidth of the reference signal, attenuation function and propagation distance. Therefore, the estimated frequency center will be deviated from the center frequency of the reference signal. In other words, the estimated frequency offset $\delta\omega$ from the reflected signal can be utilized for finding the propagation distance x. However, measuring the center frequency of the signal $\omega_{u(x)}$ accurately is not a simple task; because the attenuation which is linearly increasing with frequency will

result in decrease in SNR of the received signal. Similarly, the time center $(t_{u(x)})$ of the signal $u(x,t)$ with the propagation distance x can be evaluated as shown as follows:

$$
\begin{aligned}
t_{u(x)} &= \int t|u(x,t)|^2 dt \\
&= Re\{\int S^*(\omega,x)(-\frac{1}{j}\frac{\partial}{\partial\omega}S(\omega,x))d\omega\} \\
&= Re\{\int S^*(\omega,x)(j\frac{\partial}{\partial\omega}S(\omega,x))d\omega\} \\
&= Re[\int S^*(\omega,0)H^*(\omega,x)(j\frac{\partial}{\partial\omega}S(\omega,0)H(\omega,x) + jS(\omega,0)\frac{\partial}{\partial\omega}H(\omega,x))d\omega] \\
&= Re[j\int S^*(\omega,0)S'(\omega,0)H^*(\omega,x)H(\omega,x)d\omega + \\
&\quad j\int S^*(\omega,0)S(\omega,0)H*(\omega,x)H'(\omega,x)d\omega] \\
&= Re[j\int S^*(\omega,0)S(\omega,0)H^*(\omega,x)H(\omega,x)\frac{\alpha + j\beta(\omega-\omega_0)}{\alpha^2+\beta^2}d\omega \\
&\quad +j\int S^*(\omega,0)S(\omega,0)H^*(\omega,x)H(\omega,x)(-\alpha'(\omega) + jk'(\omega))xd\omega] \\
&= -\frac{\beta C^2}{\alpha^2+\beta^2}\int(\omega-\omega_0)\exp\left(-\alpha\frac{(\omega-\omega_0)^2}{(\alpha^2+\beta^2)} + 2A\omega x\right)d\omega \\
&\quad +Kx\cdot C^2\sqrt{\frac{\alpha}{\pi(\alpha^2+\beta^2)}}\int\exp\left(-\alpha\frac{(\omega-\omega_0)^2}{(\alpha^2+\beta^2)} + 2A\omega x\right)d\omega \\
&= -\frac{\beta}{\alpha^2+\beta^2}\left[\int\omega\frac{1}{\sqrt{2\pi}\left(\sqrt{\frac{\alpha^2+\beta^2}{2\alpha}}\right)^2}\exp\left(-\frac{\left(\omega-(\omega_0+\frac{\alpha^2+\beta^2}{\alpha}Ax)\right)^2}{2\left(\sqrt{\frac{\alpha^2+\beta^2}{2\alpha}}\right)^2}\right)d\omega\right. \\
&\quad \left. -\omega_0\cdot\frac{\beta}{\alpha^2+\beta^2}\int\frac{1}{\sqrt{2\pi}\left(\sqrt{\frac{\alpha^2+\beta^2}{2\alpha}}\right)^2}\exp\left(-\frac{\left(\omega-(\omega_0+\frac{\alpha^2+\beta^2}{\alpha}Ax)\right)^2}{2\left(\sqrt{\frac{\alpha^2+\beta^2}{2\alpha}}\right)^2}\right)d\omega\right] \\
&\quad +Kx\int\frac{1}{\sqrt{2\pi}\left(\sqrt{\frac{\alpha^2+\beta^2}{2\alpha}}\right)^2}\exp\left(-\frac{\left(\omega-(\omega_0+\frac{\alpha^2+\beta^2}{\alpha}Ax)\right)^2}{2\left(\sqrt{\frac{\alpha^2+\beta^2}{2\alpha}}\right)^2}\right)d\omega
\end{aligned}
$$

$$= -\frac{\beta}{\alpha^2 + \beta^2}\left(\omega_0 + \frac{\alpha^2 + \beta^2}{\alpha}Ax - \omega_0\right) + Kx$$

$$\text{(because } C^2 = e^{2\omega_0 Ax - \frac{\alpha^2 + \beta^2}{\alpha}A^2 x^2})$$

$$= -\frac{\beta}{\alpha^2 + \beta^2} \cdot \delta\omega + Kx \tag{6.16}$$

Therefore, the estimated time center $t_{u(x)}$ is the propagation delay of the frequency center $\omega_{u(x)}$. For an accurate measure of the propagation delay, the actual estimation of the delay of the waveform is to be compensated by δt which is determined by chirp rate parameter β and frequency deviation $\delta\omega$ such that:

$$t_{delay} = t_{u(x)} - t_s + \frac{\delta\omega}{\beta} = \Delta t + \delta t \tag{6.17}$$

where t_s is the time center of $u(x = 0)$. Then the actual propagation distance can be evaluated with knowledge of the velocity of propagation, v. Now consider the classical cross correlation to resolve the fault location problem. For the detection of the fault, the correlation of the time-frequency distribution of the the reference signal and reflected signal is utilized. Denote the reflected signal as $r(t)$ and its Wigner distribution as $W_r(t, \omega)$, and $W_s(t, \omega)$ as the Wigner distribution of the reference signal $s(t)$. Then one can evaluate a time-frequency cross correlation function $C_{sr}(t)$ as follows:

$$C_{sr}(t) = \frac{2\pi}{E_s E_r} \int \int W_r(t', \omega) W_s(t' - t, \omega) d\omega dt' \tag{6.18}$$

where

$$E_r = \int \int W_r(t', \omega) d\omega dt'$$

$$E_s = \int \int W_s(t, \omega) dt d\omega$$

where the time integrals are carried out over the duration of the reference signal or reflected signal, as appropriate. The denominators E_r and E_s play

the role of normalization factors so that the time-frequency cross correlation function is bounded between 0 and 1.

Considering the transfer function of the coaxial cable, the time-frequency distribution of the reference signal is given by (6.6) and that of the reflected signal $W_r(t, \omega)$ can be obtained as follows:

$$W_r(t, \omega) = \frac{1}{\pi} e^{-\alpha(t-x/v)^2 - (\omega - \beta(t-x/v) - \omega_0)^2/\alpha} \cdot e^{-2Ax\omega} \tag{6.19}$$

The last term of the equation, $e^{-2Ax\omega}$, is the time-frequency distribution of the transfer function of the coaxial cable. Also, assign the time index, t_{M_x}, of the local maximum of $C_{sr}(t)$ at distance x, such that

$$
\begin{aligned}
C_{sr}(t) &= \frac{2\pi}{E_r(t)E_s} \int_{t'=t-T_s}^{t'=t+T_s} \int_{-\infty}^{\infty} W_r(t', w) W_s(t' - t, \omega) d\omega dt' \\
&= \frac{2\pi}{E_r(t)E_s} \int_{t'=t-T_s}^{t'=t+T_s} \int_{-\infty}^{\infty} \left(e^{-2Ax\omega} \frac{1}{\pi} e^{-\alpha(t'-kx)^2 - (\omega - \beta(t'-kx) - \omega_0)^2/\alpha} \right) \\
&\quad \cdot \left(\frac{1}{\pi} e^{-\alpha(t'-t)^2 - (w - \beta(t'-t) - w_0)^2/\alpha} \right) dw dt'
\end{aligned} \tag{6.20}
$$

where

$$
\begin{aligned}
E_r(t) &= \int_{t'=t-T_s}^{t'=t+T_s} \int_{-\infty}^{\infty} W_{s*h}(t', \omega) d\omega dt' \\
&= \int_{t'=t-T_s}^{t'=t+T_s} \int_{-\infty}^{\infty} \left(e^{-2Ax\omega} \frac{1}{\pi} e^{-\alpha(t'-kx)^2 - (\omega - \beta(t'-kx) - \omega_0)^2/\alpha} \right) d\omega dt' \\
&= \frac{1}{\pi} \int_{t'=t-T_s}^{t'=t+T_s} e^{-\alpha(t'-kx)^2} \int_{-\infty}^{\infty} e^{-(\omega - \beta(t'-kx) - \omega_0)^2/\alpha - 2Ax\omega} d\omega dt' \\
&= e^{\frac{(\alpha^2 + \beta^2)}{\alpha} A^2 x^2 - 2Ax\omega_0} \\
&= e^{-2Ax(\omega_0 - \delta\omega/2)}
\end{aligned} \tag{6.21}
$$

$$
\begin{aligned}
E_s &= \int_{-\infty}^{\infty}\int_{-\infty}^{\infty} W_s(t,\omega)\,d\omega dt \\
&= \int_{-\infty}^{\infty}\int_{-\infty}^{\infty}\left(\frac{1}{\pi}e^{-\alpha t^2-(\omega-\beta t-\omega_0)^2/\alpha}\right)d\omega dt \\
&= \frac{1}{\pi}\int_{-\infty}^{\infty}e^{-\alpha t^2}\int_{-\infty}^{\infty}\left(e^{-(\omega-\beta t-\omega_0)^2/\alpha}\right)d\omega dt \\
&= \sqrt{\frac{\alpha}{\pi}}\int_{-\infty}^{\infty}e^{-\alpha t^2}\,dt \\
&= 1 \tag{6.22}
\end{aligned}
$$

$$
\begin{aligned}
C_{sr}(t) &= \frac{2\pi}{e^{\frac{(\alpha^2+\beta^2)}{\alpha}A^2x^2-2Ax\omega_0}}\frac{1}{\pi^2}\int_{t'=t-T_s}^{t'=t+T_s}e^{-\alpha[(t'-kx)^2+(t'-t)^2]} \\
&\quad \cdot\int_{-\infty}^{\infty}e^{-[(\omega-\beta(t'-kx)-\omega_0)^2+(\omega-\beta(t'-t)-\omega_0)^2]/\alpha-2Ax\omega}d\omega dt' \\
&= \frac{2\pi}{e^{\frac{(\alpha^2+\beta^2)}{\alpha}A^2x^2-2Ax\omega_0}}\frac{1}{\pi^2}\int_{t'=t-T_s}^{t'=t+T_s}e^{-\alpha[(t'-kx)^2+(t'-t)^2]} \\
&\quad \cdot\left(\sqrt{\frac{\alpha\pi}{2}}e^{-\frac{\beta^2(t-kx)^2}{2\alpha}}e^{\frac{\alpha A^2x^2}{2}}e^{Ax(\beta(2t'-kx-t)+2\omega_0)}\right)dt' \\
&= 2\pi e^{-\frac{(\alpha^2+\beta^2)}{\alpha}A^2x^2+2Ax\omega_0}\frac{1}{\pi^2}\left(\sqrt{\frac{\alpha\pi}{2}}e^{-\frac{\beta^2(t-kx)^2}{2\alpha}}e^{\frac{\alpha A^2x^2}{2}}e^{-2Ax\omega_0}\right) \\
&\quad \cdot\int_{-\infty}^{\infty}e^{-\alpha[(t'-kx)^2+(t'-t)^2]-Ax\beta(2t'-kx-t)}dt' \\
&= 2\pi e^{-\frac{(\alpha^2+\beta^2)}{\alpha}A^2x^2+2Ax\omega_0}\frac{1}{\pi^2}\left(\sqrt{\frac{\alpha\pi}{2}}e^{-\frac{\beta^2(t-kx)^2}{2\alpha}}e^{\frac{\alpha A^2x^2}{2}}e^{-2Ax\omega_0}\right) \\
&\quad \cdot\left(\sqrt{\frac{\pi}{2\alpha}}e^{\frac{A^2x^2\beta^2}{2\alpha}}e^{-\frac{\alpha(t-kx)^2}{2}}\right) \\
&= e^{-\frac{(\alpha^2+\beta^2)(A^2x^2+(t-kx)^2)}{2\alpha}} \\
&= e^{-\frac{\alpha^2+\beta^2}{2\alpha}(t-kx)^2-Ax(\frac{\alpha^2+\beta^2}{2\alpha}Ax)} \\
&= e^{-Ax\cdot\delta\omega}\cdot e^{-\frac{\alpha^2+\beta^2}{2\alpha}(t-Kx)^2} \tag{6.23}
\end{aligned}
$$

Then the time-frequency cross correlation function of the reflected signal $C_{sr}(t)$ is,

$$C_{sr}(t) = e^{-\frac{\alpha^2+\beta^2}{2\alpha}(Ax)^2} \cdot e^{-\frac{\alpha^2+\beta^2}{2\alpha}(t-x/v)^2} \qquad (6.24)$$

Therefore, the existence of the reflected signal is to be detected by a quantitative number between 0 and 1. From examination of the time-frequency cross correlation function $C_{sr}(t)$ in (6.24), it is clear that it will be a maximum (local peak time) at $t = x/v$, as expected. The first term on the RHS decreases because, as the reflected signal travels farther, its high frequency content will be attenuated more, and thus the reflected signal will be less correlated with the reference signal.

In later sections, the local peak time of the time-frequency cross correlation function will be utilized to accurately measure the propagation delay of the reflected signal, which is then to be converted into the fault location with knowledge of the velocity of propagation.

6.3 Experimental Setup

To demonstrate the ability of TFDR to detect and locate various types of faults in RG 142 and RG 400 type coaxial cables, an experimental TFDR system is organized as shown in Fig. 6.4. The system consists of a circulator, an arbitrary waveform generator (Tektronix, AWG610) and an oscilloscope (Agilent Infinium) which are connected to a computer with GPIB cable for automatic control of the instruments. The computer controls the arbitrary waveform generator (AWG) to produce the Gaussian envelope chirp signal which propagates into the target cable via the circulator. This reference signal is reflected at the fault location and back to the circulator. The circulator redirects the reflected signal to the digital oscilloscope. The computer controls

124
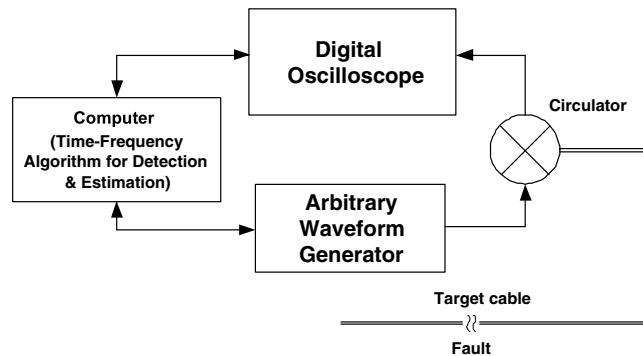
Figure 6.4: Experimental setup for time-frequency domain reflectometry.

and synchronizes the arbitrary waveform generator and digital oscilloscope, calculates the time-frequency distribution of the reference signal and reflected signals, and executes the time-frequency cross correlation algorithm.

The purpose of the experiment is to verify the feasibility of time-frequency domain reflectometry. Furthermore, the performance is to be compared with a commercial TDR. The experiment is carried out for two types of coaxial cables, i.e., RG 142 and RG 400 types. Various distances and types of faults are considered. The actual location of the faults varies from 10m, 20m, 30m and 40m while the types of faults are classified as "open", "short" and "damage". The "damage" of the coaxial cable is emulated by a failure of the external shields so that the internal dielectric material is exposed over 1cm. Thus a total of 24 experiments (2 types of cables × 4 fault distances × 3 types of faults) are carried out. To evaluate the performance of TFDR in fault detection and localization, the same 24 experiments are repeated using a commercial TDR system which has a rise time of 300ps.

125
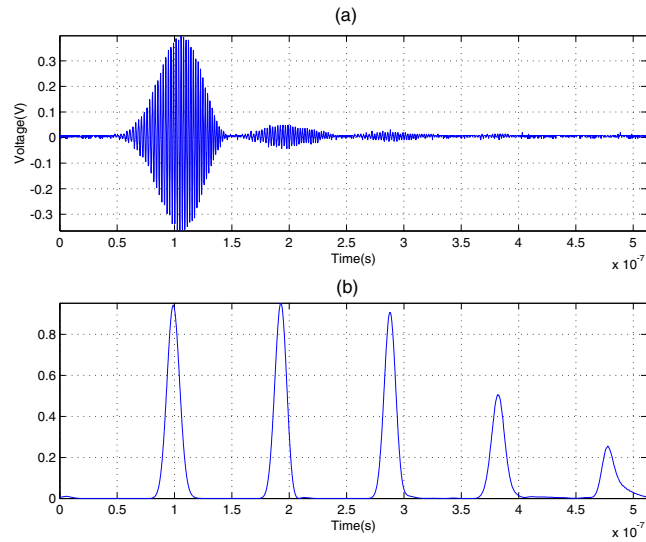
Figure 6.5: Time series of the reflected signal in (a) and corresponding time-frequency cross correlation function for detection and estimation of the "damage" fault in (b) for a fault at 10m in RG 142 type coaxial cable. (The first peak of correlation is at 96.5 ns. and the second one is at 191.0 ns.)

6.4   Result and Analysis

We have carried out several experiments in which we compare the ability of TFDR and TDR to locate various types of faults at various distances in coaxial cable. For a fair comparison between TFDR and TDR, we use the same velocity of propagation, $v{=}2.10{\times}10^8$ m/sec., which was obtained experimentally for both types of cables. Also note that the sampling rates for reflected signal acquisition of the TFDR is 4GHz while that of the TDR is 12 GHz in this experiment.

6.4.1   Experimental Result

In Fig. 6.5, we consider the case of RG 142 type coaxial cable which has a damage-type fault located 10 meters away from the source of the ref-

erence signal. Fig 6.5-(a) is the acquired time series of the reflected signal at a 4 GHz sampling rate while Fig. 6.5-(b) is the time-frequency cross correlation between the time-frequency distributions of the reference signal and the reflected signal. In Fig. 6.5-(a) and (b), the reference signal and the first reflected signal from the fault are observed around 100 ns. and 190 ns, respectively. The remaining peaks in the time-frequency cross correlation are caused by multiple reflections. Note, however, as shown in Fig. 6.5, the waveform caused by multiple reflections can be accurately detected and localized by the time-frequency cross correlation function, while such multiple reflections are a potential problem in TDR. The time-frequency cross correlation provided in Fig. 6.5-(b) can be interpreted via (6.24): with increasing propagation distance x, the peak value of the time-frequency correlation function exponentially decays for the reason described previously, while the time spread of the time-frequency correlation function is inversely proportional to the frequency bandwidth squared of the reference signal as indicated in (6.4) and (6.24). The second local peak of the time-frequency cross correlation function indicates the presence of the reflected signal which enables one to determine the round-trip propagation time. The estimated time of the first peak, which is the reference signal itself is 96.5 ns, while the estimated time of the second peak is 191.0 ns. With the obtained v of the RG 142 coaxial cable (2.10×10^8 m/sec.), the location of the fault can be estimated to be 9.92 m.

The example provided in Fig. 6.6 presents a sample case for RG 400 type coaxial cable which has a damage-type fault located 30 meters away from the source of the reference signal. In Fig. 6.6-(a), the signal that occupies the time duration between 50ns and 150ns is the reference signal, and the signal component located in the time interval between 350ns and 400ns (which is difficult to see in the time domain) is the reflected signal from the damage
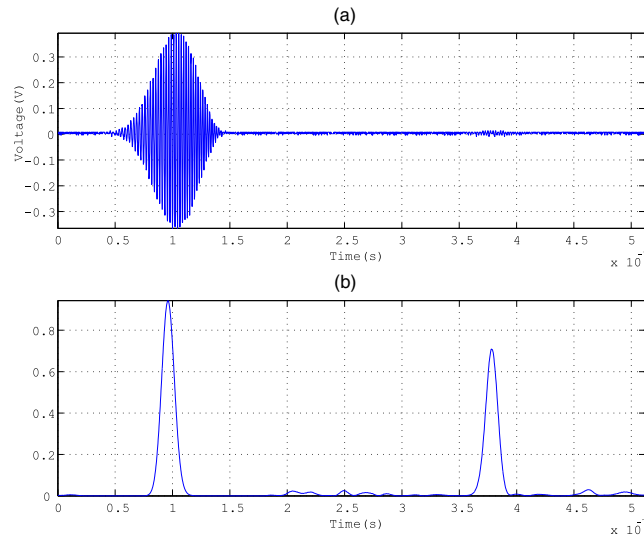
Figure 6.6: Time series of the reflected signal in (a) and corresponding time-frequency cross correlation function for detection and estimation of the "damage" fault in (b) for a fault at 30m in RG 400 type coaxial cable. (The first peak of correlation is at 96.3 ns. and the second one is at 379.7 ns.)

to the cable. Fig. 6.6-(b) is the time-frequency cross correlation between the reference signal and the reflected signal time-frequency distributions: the first peak (estimated time : 96.3 ns) of the correlation function in Fig. 6.6-(b) reveals the existence of the reference signal itself, and the second peak (estimated time : 379.7 ns.) indicates the presence of a fault. The location of the fault is evaluated to be 29.76 m.

In order to compare the performance in accuracy between TDR and TFDR, the same coaxial cable with the same fault is tested using a commercial TDR instrument. Fig. 6.7 is acquired by the TDR instrument under the same conditions as the experiment corresponding to Fig. 6.6. TDR detects the fault through a step change of the reflected signal, and estimates the time of arrival from the time the step-change occurs. However, as shown in Fig. 6.7, the ideal
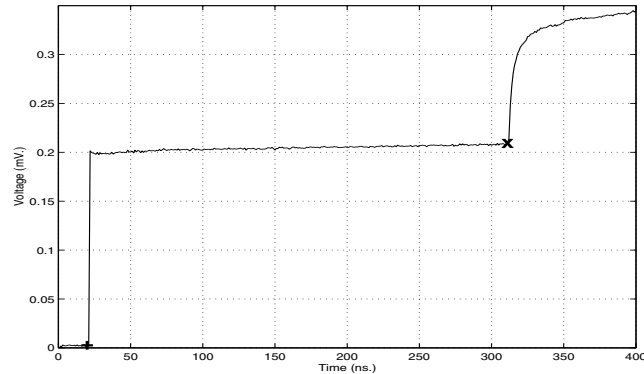
Figure 6.7: A screen snapshot of the TDR for the detection and estimation of the fault location for a fault at 30m in RG 400 type coaxial cable. (The first marker is at 23.5 ns. and the second one is at 304.5 ns.)

step of the reference signal is smeared in the reflected signal so that it is not always easy to measure accurately the arrival time of the reflected step. The location of the fault is measured to be 29.51 m.

6.4.2   Analysis and Discussion of Results

To compare the fault location accuracy of TFDR and TDR, the location of the faults vary from 10m, 20m, 30m to 40m. In each location, three types of faults are considered: "open", "short" and "damage" as described in Sec. 8.3. The overall experimental results are summarized in Table 6.1 and Table 6.2 for the RG 142 and RG 400 type coaxial cables, respectively. Note that the experimental results provided in the tables are obtained from several trials for each case. The TFDR experimental determination of propagation time was repeatable within to $\pm$ 2 sample periods, which corresponds to $\pm$ 0.105 m. As one can see in Table 6.1 and Table 6.2, TFDR yields a smaller error than TDR for all types and locations of the faults. The errors for TDR vary from 0.31 m to 0.74 m while the errors of TFDR range from 0.08 m to

129

		RG142 (TFDR)	Error (m)	RG142 (TDR)	Error (m)
	damage	39.80	0.20	39.61	0.39
40m	open	39.78	0.22	39.47	0.53
	short	39.77	0.23	39.47	0.53
	damage	29.80	0.20	29.55	0.45
30m	open	29.78	0.22	29.55	0.45
	short	29.78	0.22	29.32	0.68
	damage	19.84	0.16	19.27	0.73
20m	open	19.84	0.16	19.56	0.44
	short	19.86	0.14	19.56	0.44
	damage	9.92	0.08	9.69	0.31
10m	open	9.88	0.12	9.67	0.33
	short	9.89	0.11	9.67	0.33

Table 6.1: Comparison of TDR and TFDR estimates of fault location for four fault locations, and three types of faults for RG 142 Type Coaxial Cable

0.28m, for all cases. Note that in TFDR, the detection and localization process is completely automated based on identifying the peaks of the time-frequency correlation function; however, the operation of the TDR involves adjusting markers on the smeared edges in the reflected signal as shown in Fig. 6.7, and is thus subject to human judgement.

For a more graphical comparison of the results, the corresponding percentage error for each cable type is evaluated and plotted in Figs. 6.8 and 6.9. As one can see in these figures, TFDR yields a smaller percentage error than TDR for all locations of the fault: the errors for TDR are between 0.3% and 0.8% while the errors of TFDR are under 0.4% for all cases. Both TDR and TFDR show a tendency for the error rate to increase with distance. As the length of the cable increases, the energy of the reflected signal will decrease exponentially, which results in a lower SNR for both TDR and TFDR.

		RG400 (TFDR)	Error (m)	RG400 (TDR)	Error (m)
	damage	39.74	0.26	39.37	0.63
40m	open	39.64	0.26	39.26	0.74
	short	39.85	0.15	39.37	0.63
	damage	29.76	0.24	29.51	0.49
30m	open	29.72	0.28	29.41	0.59
	short	29.77	0.23	29.48	0.52
	damage	19.90	0.10	19.58	0.42
20m	open	19.87	0.13	19.47	0.53
	short	19.87	0.13	19.58	0.42
	damage	9.91	0.09	9.51	0.49
10m	open	9.89	0.11	9.62	0.38
	short	9.90	0.10	9.62	0.38

Table 6.2: Comparison of TDR and TFDR estimates of fault location for four fault locations, and three types of faults for RG 400 Type Coaxial Cable

In Fig. 6.10, a time-frequency distribution of the reflected signal from the "damage" fault located at 30 m in a RG 400 type coaxial cable is provided along with its time series and frequency spectrum. The reflected signal in Fig. 6.10 is the same as the barely visible reflected signal at 379.7 ns. in Fig. 6.6-(a). Due to the low energy level of the reflected signal, it is difficult to detect and localize the reflected signal in the time domain as shown in the top of Fig. 6.10. In the frequency domain, the reflected signal has suffered relatively severe distortion, as shown in the left side of Fig. 6.10, in comparison with the frequency spectrum of the reference signal provided in Fig. 6.3. However, in the time-frequency domain, the time-frequency localization of the reference signal is still vivid so that the existence of the signal and the location of the fault can be evaluated accurately by the time-frequency cross correlation function provided in Fig. 6.6-(a). Therefore, one can obtain accurate localization
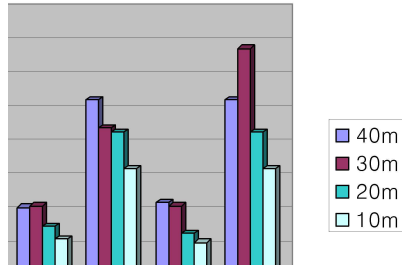
Figure 6.8: Comparison of the fault location percentage error for TFDR and TDR for RG-142 coaxial cable for four different fault locations. (10, 20, 30, and 40m) and for three different faults (damage, open, and short)

of the fault by use of TFDR reference signal and the associated time-frequency cross correlation function in relatively low signal-to-noise ratio conditions.

The experimental results suggest that time-frequency domain reflectometry is capable of fault detection with a performance comparable to that of TDR. Yet the ability to design the reference signal for a particular cable or system being tested is a powerful advantage. To put it another way, time-frequency domain reflectometry possesses many of the advantages of TDR, while at the same time permitting one to consider the frequency-domain properties of the system under test. Thus, one possibility is to consider TFDR as being complementary to TDR in that TFDR is relatively easy to implement by adding an arbitrary waveform generator and digital signal processing unit to calculate the time-frequency cross correlation function of the sampled reference and reflected waveforms.
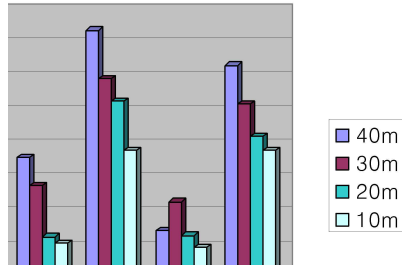
Figure 6.9: Comparison of the fault location percentage error for TFDR and TDR for RG-400 coaxial cable for four different fault locations (10, 20, 30, and 40m) and for three different faults (damage, open, and short).

6.5 Conclusion

In this chapter, we introduce joint time-frequency domain reflectometry which incorporates may of the advantages of time domain and frequency domain reflectometry. Faults on wires and cables are located from knowledge of the propagation time and velocity of propagation as in TDR. However, the use of a chirp signal with a Gaussian envelope enables one to effectively use a swept frequency reference signal as in FDR. This later capability is very important when testing wires/cables used for communication purposes. The use of time-frequency cross correlation function of the respective time-frequency distributions of the reference and reflected signals has proven to be a sensitive detector of weak reflected signals (see Fig. 6.6, for example). The experimental work involving two types of coaxial cable, three types of faults, and four fault lengths, indicates that the new time-frequency domain reflectometry locates faults with an accuracy comparable (actually, slightly better in our experiments) to TDR and, therefore, suggests that joint time-frequency

133
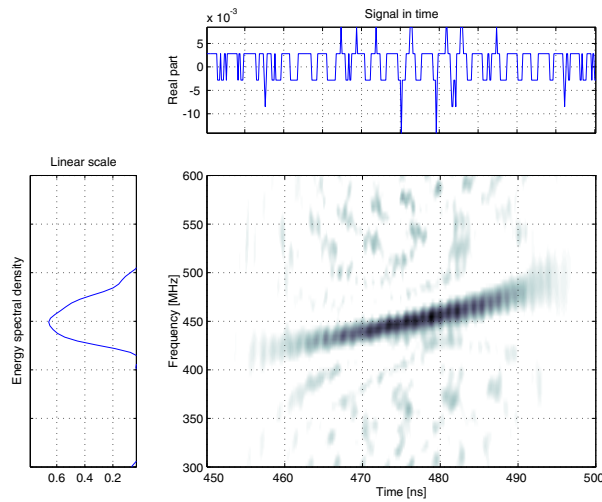
Figure 6.10: Zoomed time-frequency distribution for the reflected signal in Fig. 6.6-(a) at 379.7 ns. (Note the time origin has been translated for this magnified illustration.)

domain reflectometry offers much promise as a new wire and cable diagnostic tool, especially in the communications area.

The contribution of the TFDR to the existing reflectometry field can be summarized as follows:

1. Accurate and sensitive detection and localization of the reflected signal via time-frequency cross correlation.

2. Flexibility of reference signal design depending on the physical characteristics of system under test. For example, one can place the RF energy in the frequency band of interest.

3. Successful detection and localization of multiple reflections, even very weak reflections.

4. Minimization of the distortion of the reference signal by limiting the frequency bandwidth, where necessary.

Clearly, additional work must be done to explore the promise of TFDR including: application of TFDR to faults in wiring other than coaxial cable; consideration of noise, particularly in the case of very weak reflected signals; consideration of the effects of dispersion where appropriate; the identification of those factors affecting the accuracy of fault location; and a detailed comparison of TFDR with TDR, FDR and SWR in order to fully elucidate the advantages and limitations of TFDR.

Chapter 7

Application of Cross Time-Frequency Analysis to Dispersive Wave Propagation

7.1   Introduction

Classical Fourier-based cross-power spectra analysis [69] has been successfully utilized to estimate dispersion relations [70] in terms of phase and group velocities. The general approach is to monitor the wave field in the direction of propagation with two probes spaced a fraction of a wavelength apart. The phase of the cross-power spectrum measures the phase shift (i.e., the phase difference) that each spectral component undergoes in traveling from the first to the second probe. Since this phase shift is equal to product of the wave number times the distance of separation, the wave number as a function of frequency can be estimated by dividing the phase shift by the distance of separation.

On the other hand, time-frequency distributions provide simultaneous time and frequency information, in that they indicate how the "power" of a signal is distributed over time and frequency [1]. Due to the advantageous capability of signal's localization, it has also been applied to the fields of ocean engineering where the observed signal's time-frequency localization is required in various applications : underwater acoustics [71], signal localization [72] [73] and analysis [74] [75] etc.

Specifically, time-frequency analysis contributes to some application

fields like quantum electronics where the transient wave information is required [76] [77]. This raises the question (which is also the objective of this chapter) as to whether such distributions might be able to provide time-localized measurements of phase and group velocity for dispersive ocean wave propagation, given the same type of two wave time series used in the Fourier approach. There have been interesting application trials of wavelets [78] [79] [80] for dispersion analysis of ultrasonic signals [81] in order to calculate localized frequency-dependent phase and group velocity. Then, alternatively, time-frequency analysis also can be a good methodology to deal with dispersion analysis. However, unfortunately, the common class of time-frequency distributions known as Cohen's class [2] [34] apply to only a single time series (not two) and, furthermore, no phase information is preserved [4]. This is similar to the Fourier-based auto-power spectrum where no phase information is available.

To address the phase issue, we propose a new type of time-frequency distribution, *"cross time-frequency distribution"*. This distribution is complex, and is calculated using two time series of the wave field measured at two spatial points in the direction of wave propagation. The phase of the cross time-frequency distribution is equal to the phase shift between the two signals as a function of frequency and time [41]. Once this time-localized phase shift is obtained, time-localized measurements of the phase and group velocities can be made in principle [82].

In this chapter, we discuss the application of the cross time-frequency analysis for the time-localized analysis of the dispersive wave propagation. For the localized analysis, selection of time and frequency is a key problem to obtain reasonable estimation of phase and group velocities. Utilizing the advantageous aspects of the cross time-frequency analysis (e.g., phase difference spectrum and instantaneous joint frequency, etc.), a careful treatment of

real-world data will be demonstrated in this chapter. The numerical features of the localized analysis will be compared to other classical methodologies like Fourier analysis and wave theory in order to verify and compare the validity of the new techniques.

7.2   Experimental Setup

The experimental random wave data were collected at the Offshore Technology Research Center's Model Basin located at Texas A&M University. A schematic diagram is shown in Fig. 7.1. The basin is 30.5 meters wide, 45.7 meters long, and 5.8 meters deep. Both uni-directional and multi-directional waves may be generated by an array of 48 hinged wave boards at one end of the basin. At the opposite end, the waves are absorbed by a series of expanded metal screens of decreasing porosity. Typical reflection coefficients are of the order of a few (say, 2-5) percent.

The input to the wave maker corresponds to a JONSWAP spectrum. The model scale is 1:54.5. The unidirectional random wave elevation is measured with an array of capacitive probes. In this chapter we are concerned with the output of only two probes in the array as indicated in Fig. 7.1. Note the two probes are separated by 1.0 meter in the direction of wave propagation, with the first probe located 12.8 meters from the wave maker. The wave data was originally sampled at 40Hz, but was subsampled, to yield an effective sampling rate of 4Hz.

The wave elevation time series measured at probes 1 and 2 are shown (a) and (b) in Fig. 7.2, respectively. From a qualitative point of view, examination of Fig. 7.2 suggest the presence of some amplitude modulation, associated with wave groups, and possible frequency modulation, although
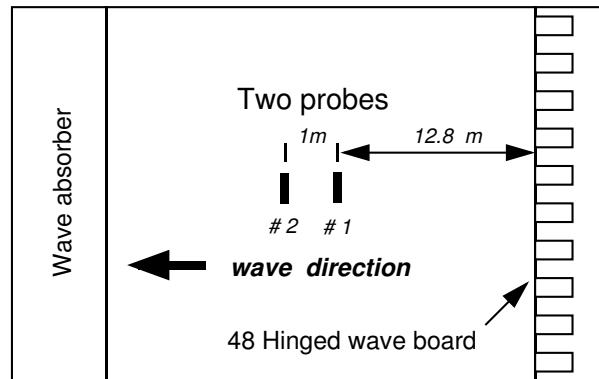
Figure 7.1: Schematic of wave basin

the latter is difficult to discern with any certainty. However, this and other time-frequency properties will become clear in the next section.

7.3 Localized Time-Frequency Information of The Waves

In this section, we employ the real-world data set described in Sec. 7.2 to demonstrate the application of the cross time-frequency distribution. The main objective of the application is to estimate localized phase and group velocities from the two propagating wave time series provided in Fig. 7.2.

In Fig. 7.4, the Fourier power spectrum of the same data is provided. The Fourier power spectrum can be regarded as the frequency marginal density of the time-frequency distribution provided in Fig. 7.3. As we can see in Fig. 7.4, the main energy of the wave time series is concentrated in neighborhood of 0.5 Hz. To begin with, the time-frequency distribution, specifically the reduced interference distribution, of the time series in Fig. 7.2-(b) is provided in Fig. 7.3. The RID contour plot in Fig. 7.3 shows time-varying spectral characteristics of the time series. The contour plot of the RID dis-
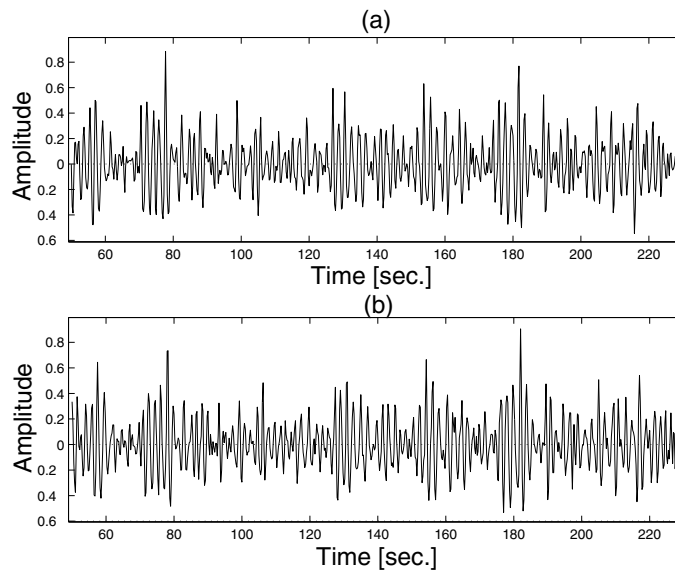
Figure 7.2: Time series data collected from probe 1 (a) and 2 (b)
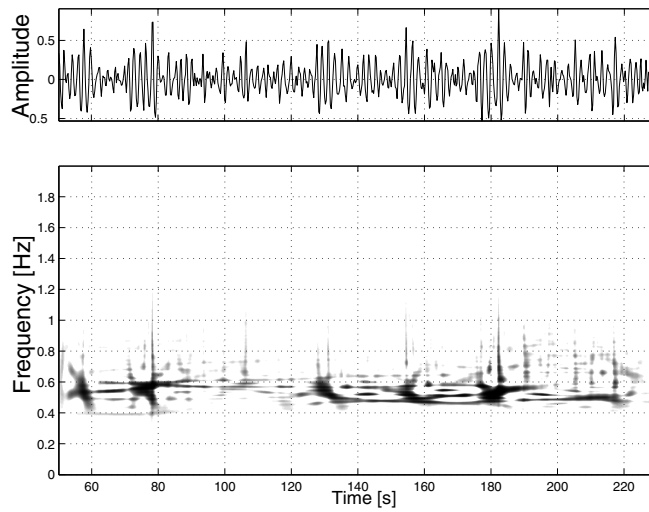
Figure 7.3: Reduced interference distribution of the wave time series

140
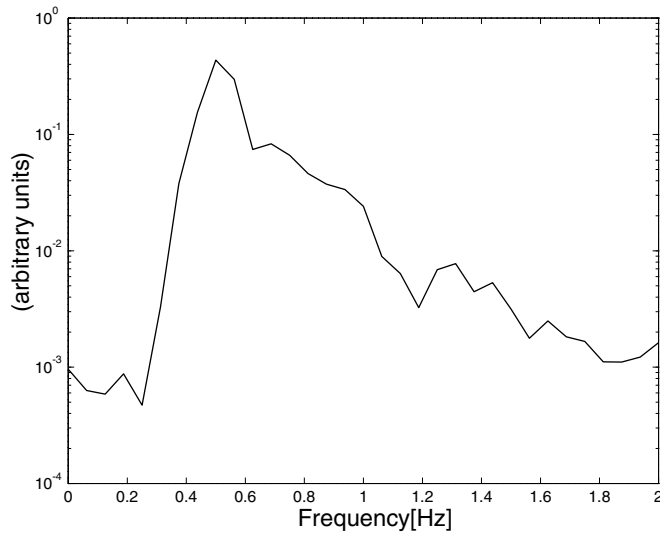
Figure 7.4: Power spectrum of the wave time series in Fig. 7.2-(b)

tribution clearly shows the amplitude modulation and frequency modulation associated with the "groups" or "packets" of the large amplitude waves. Six major wave groups are observed, roughly speaking, around 60 sec., 75 sec., 130 sec., 155 sec., 180 sec., and 210 sec. At the time of passage of these large-amplitude groups, the time-frequency distribution takes on an approximate U-shape, indicating that the frequency drops then rises. Note also that when the largest amplitude wave occurs at 180 sec. in the group, there is a vertical peak in the time-frequency distribution indicating the presence of high frequency components necessary to synthesize the rather sudden jump in wave elevation. However, unfortunately, the phase information of the time-series is lost in the RID in Fig. 7.3. In addition, it is difficult to find a way to relate two individual time-frequency distribution functions for two individual time series provided in Fig. 7.2-(a) and (b).

To treat the two time series together, let us employ the cross time-

141
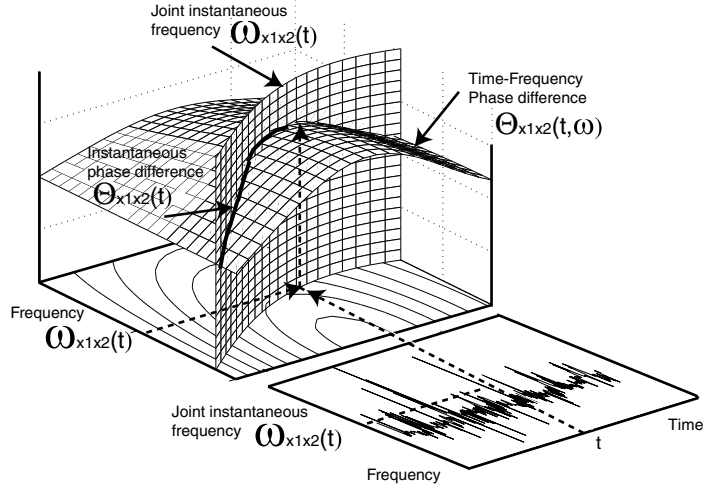
Figure 7.5: Determination of localized cross time-frequency phase difference spectrum

frequency distribution in (2.19). The cross time-frequency distribution can be characterized by the time-frequency phase difference spectrum which is not available via classical instantaneous auto-correlation based time-frequency distributions. Fortunately, for a given cross time-frequency distribution $J_{x_1 x_2}(t, \omega; \phi)$, the instantaneous frequency and group delay can be treated as a joint moment. Therefore, the joint instantaneous frequency provides local joint mean frequency for two time series for a given time instant t.

As the cross time-frequency distribution is complex, we can rewrite the distribution the time-frequency phase spectrum $\Theta_{x_1 x_2}(t, \omega; \phi)$ is defined as follows:

$$\Theta_{x_1 x_2}(t, \omega; \phi) = \tan^{-1}[\frac{\text{Im}\{J_{x_1 x_2}(t, \omega; \phi)\}}{\text{Re}\{J_{x_1 x_2}(t, \omega; \phi)\}}] \qquad (7.1)$$

The time-frequency phase spectrum will provide the phase difference information between a pair of signals as a function of time and frequency. For

142
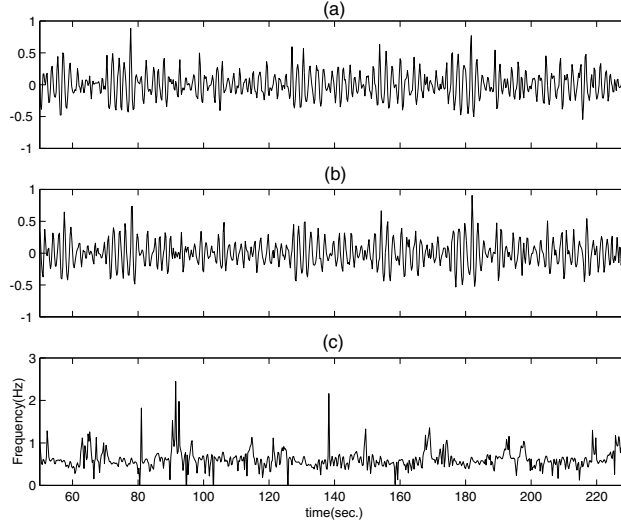
Figure 7.6: Time series, (a)(b), joint instantaneous frequency via cross time-frequency distribution (c)

the proper application of the time-frequency phase difference spectrum, it is very important to choose reasonable time or frequency index. For example, in order to obtain time-varying phase difference spectrum, one can define *"instantaneous phase difference"*, $\Theta_{x_1 x_2}(t; \phi)$, by using joint instantaneous frequency $\omega_{x_1 x_2}(t)$

$$\Theta_{x_1 x_2}(t; \phi) = \Theta_{x_1 x_2}(t, \omega = \omega_{x_1 x_2}(t); \phi) \qquad (7.2)$$

As shown in Fig. 7.5, the instantaneous phase difference $(\Theta_{x_1 x_2}(t; \phi))$ is obtained by the tracking the time-frequency phase difference spectrum $(\Theta_{x_1 x_2}(t, \omega; \phi))$ with the joint instantaneous frequency $(\omega_{x_1 x_2}(t))$. Therefore, the instantaneous phase difference is a reasonable estimate of transient phase difference information. In Fig. 7.6, the time series from the wave basin probes are shown in (a) and (b), and the joint instantaneous frequency $\omega_{x_1 x_2}(t)$, defined in P6 of Chapter. 2, of the two time series is presented in Fig. 7.2-(c). The joint

143
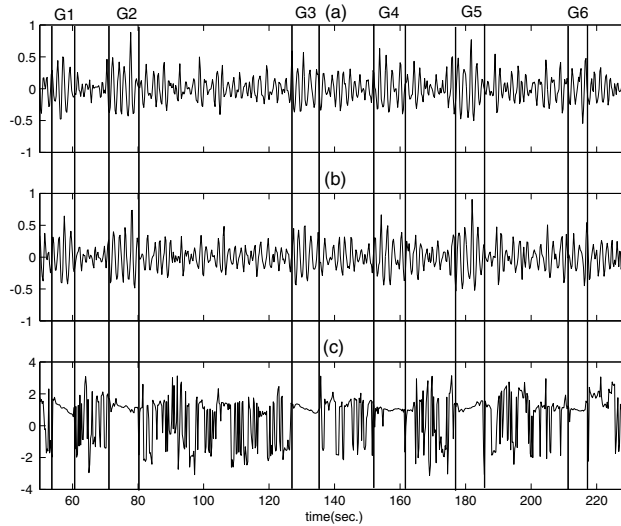
Figure 7.7: (Time series in (a) and (b), corresponding instantaneous phase difference spectrum in (c)

instantaneous frequency plot in Fig. 7.6-(c) can be regarded as an average of the instantaneous frequency for individual time series in Fig. 7.6-(a),(b). The joint instantaneous frequency deviates from a center frequency of around 0.5 Hz as time goes on; some extreme peaks of the joint instantaneous frequency are observed at the points of abrupt phase change at 80 sec., 90 sec., 138 sec., and 170 sec. etc. Joint instantaneous frequency plot is a good manifestation of the non-stationary, time-varying spectral characteristics of the wave time series.

In Fig. 7.7, the time series in (a) and (b), and instantaneous phase difference phase spectrum is provided in (c). Note that the time-varying phase difference spectrum in Fig. 7.7-(c) is a cross section of the time-frequency phase difference spectrum in (2.26) by joint instantaneous frequency in Fig. 7.6-(c).

144

In Fig. 7.6-(c), some time intervals show coherent phase difference, while the other portions are rapidly varying. Each coherent phase time interval has been matched to the time series in Fig. 7.6-(a),(b). Each time interval is assigned as $G_1 \sim G_6$, which corresponds to the wave groups. Note the fact that the phase coherent time interval is coincident with the dominant energy wave groups observed in the reduced interference distribution in Fig. 7.3. It shows that the dominant wave group is characterized by not only high amplitude, but also by a coherent phase difference.

Consider the calculation of the phase velocity v_{ph} by phase difference $\Theta(t, \omega; \phi)$. If a specific wave group is selected (say G_i) with local frequency ω_i, then we can determine the wave number of wave group of G_i by $k_i(\omega)$, from $k_i(\omega) = \Theta_{G_i}(\omega; \phi)/\Delta z$, where Δz is fixed geometric separation between the probes. Therefore, the phase velocity for a specific wave group G_i can be calculated as follows:

$$v_{ph}|_i = \frac{\omega}{k_i(\omega)}|_{\omega=\omega_i} = \frac{\omega_i}{\Theta_{G_i}(\omega_i; \phi)} \cdot \Delta z \qquad (7.3)$$

Similarly, the group velocity also can be derived in terms of the phase difference $\Theta_{G_i}(\omega)$ as follows:

$$v_g|_i = \frac{\partial \omega}{\partial k_i(\omega)}|_{\omega=\omega_i} = \frac{\partial \omega_i}{\partial \Theta_{G_i}(\omega_i; \phi)} \cdot \Delta z \qquad (7.4)$$

As one can see in (7.3) and (7.4), the selection of time and frequency is important for localized analysis. Note that the selection of time interval is based on the instantaneous phase difference spectrum in Fig. 7.7 while the local frequency selection is based on the joint instantaneous frequency in Fig. 7.6, which is reasonable and consistent.

Depending on the local phase difference spectrum as shown in Fig.

145
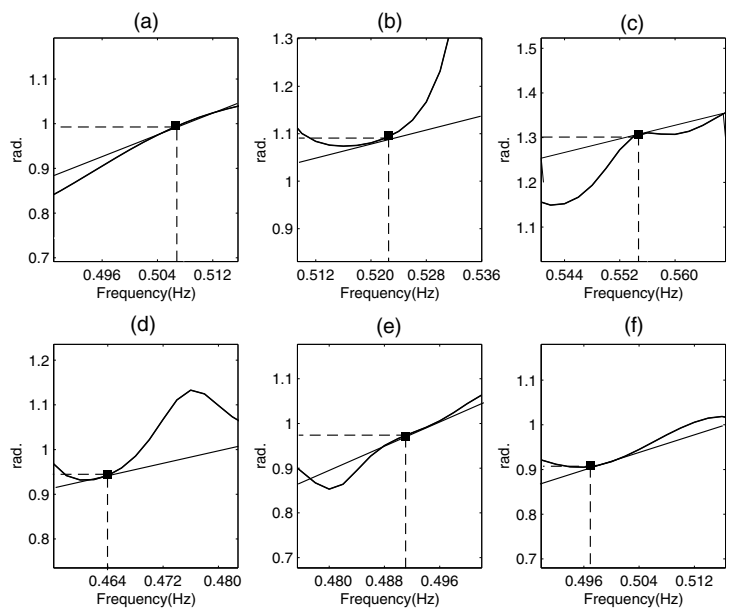
Figure 7.8: Time-localized phase difference spectrum of each wave group:(a)-
G_1, (b)-G_2 (c)-G_3, (d)-G_4, (e)-G_5 and (f)-G_6

Table 7.1: Comparison of the estimation of phase velocity and group velocity
for individual wave groups

	G_1	G_2	G_3	G_4	G_5	G_6	Mean
phase velocity (m/sec.)	3.25	3.04	2.68	3.10	3.22	3.46	3.12
group velocity (m/sec.)	1.05	1.62	1.79	1.88	0.94	1.28	1.32
local frequency (Hz)	0.508	0.524	0.556	0.464	0.492	0.496	0.503
fraction of energy (%)	12.80	9.18	15.0	13.8	35.2	6.86	92.8

146

7.8, each wave group shows somewhat different phase velocity, group velocity, and local frequency. In Table 7.1, estimated phase velocity, group velocity, local frequency and fraction of energy are provided for individual wave groups. Among the wave groups, G_5 which is called "extreme-like" wave shows greatest fraction of energy and it is the focus for the localized analysis. The fraction of energy is the ratio of energy of a specific wave group to the energy of whole time series. The wave group, G_5 shows slightly lower (than average) local frequency, but higher (than average) phase velocity. In addition, the difference between the phase and group velocity is the largest, which implies dispersive wave propagation. Therefore, based on the cross time-frequency distribution and with corresponding localization techniques, one can obtain localized information of individual wave groups. However, it is necessary for one to verify the validity of the localized parameter estimations described in this section. Therefore, with exactly same data, we will compare and analyze the obtained result with other types of techniques in Sec. 7.4.

7.4 Other Methodologies for the Analysis of Dispersion Effect

In this section, we will discuss alternative methodologies to calculate phase and group velocities to validate the estimations discussed in Sec. 7.3. First of all, we employ classical Cohen's class time-frequency distribution for an individual wave group analysis. In addition, classical Fourier based cross power spectrum and wave equations are employed to verify the result. However, note that the analysis discussed in Sec. 7.3 is localized analysis, while the traditional methodologies like classical Fourier based cross power spectrum and wave equations are not. Therefore, in a strict sense, it might not be a fair

comparison. However, if the weighted average value of the localized analysis is somewhat close to the traditional methodologies, it is a valuable verification for the cross time-frequency based analysis.

7.4.1 Classical Time-Frequency Analysis (RID)

The physical meaning of group velocity is the velocity with which the energy or information of a signal propagates [83]. The group delay of signal implies mean arrival time of a specific frequency component that conveys energy or information. Group delay of a signal is defined in terms of time-frequency distribution as follows [2]:

$$\{\frac{\int tC_x(t,\omega;\phi)dt}{\int C_x(t,\omega;\phi)dt}\} = -t_x(\omega) \tag{7.5}$$

On the basis of this relationship, we develop an approach to estimate group velocity from estimates of group delay at two spatial points in the direction of wave propagation. Note that the reduced interference distribution that we are using in this chapter has been shown to yield reasonable estimates of group delay [6].

In signal processing, if a phase of envelope is provided as $\Theta(\omega)$, the group delay is defined as follows [84]:

$$t_g(\omega) = -\frac{d\Theta(\omega)}{d\omega} \tag{7.6}$$

Define the phase of the envelope at $z = z_1$ and $z = z_2$ as $\Theta_{z_1}(\omega)$ and $\Theta_{z_2}(\omega)$, respectively, where

$$\Theta_{z_1}(\omega) = t\Delta\omega - z_1\Delta k \tag{7.7}$$

$$\Theta_{z_2}(\omega) = t\Delta\omega - z_2\Delta k \tag{7.8}$$

Taking the derivative with respect to ω and following the definition of group delay in Eq. (7.6), we get

$$t_g|_{z_1} = -\frac{d\Theta_{z_1}(\omega)}{d\omega} \cong -t + \frac{\Delta k}{\Delta\omega} z_1 \qquad (7.9)$$

$$t_g|_{z_2} = -\frac{d\Theta_{z_2}(\omega)}{d\omega} \cong -t + \frac{\Delta k}{\Delta\omega} z_2 \qquad (7.10)$$

Subtracting the Eqs. (7.9) and (7.10) yields,

$$t_g|_{z_2} - t_g|_{z_1} = \frac{\Delta k}{\Delta\omega} z_2 - \frac{\Delta k}{\Delta\omega} z_1 \qquad (7.11)$$

Therefore, the group velocity is expressed in terms of spatial separation and difference of group delay as follows:

$$v_g = \frac{\Delta\omega}{\Delta k} = \frac{z_2 - z_1}{t_g|_{z_2} - t_g|_{z_1}} = \frac{\Delta z}{\Delta t_g} \qquad (7.12)$$

In other words, if observations of wave elevation at two spatially separated points are available, the estimation of the difference of group delay allows one to estimate the group velocity. However, in the case of real wave signals, the presence of time-varying frequency and time-varying amplitude makes the problem more difficult. However, time-frequency analysis enables one to calculate reasonable estimates of group delay, and thus group velocity for a non-stationary wave group.

We are especially interested in the *"extreme wave"* group G_5 that occurs around 180 sec. in Fig. 7.2 and 7.7. In addition, because that wave group is characterized by the highest energy fraction, the calculation is more reliable than other wave groups. Therefore, we localize the wave group around 180 sec., to calculate group velocity. The group delay difference is plotted in Fig. 7.9. Before we discuss the result of group delay difference, we must recall that the local joint instantaneous frequency of the wave group is 0.492 Hz. To

149
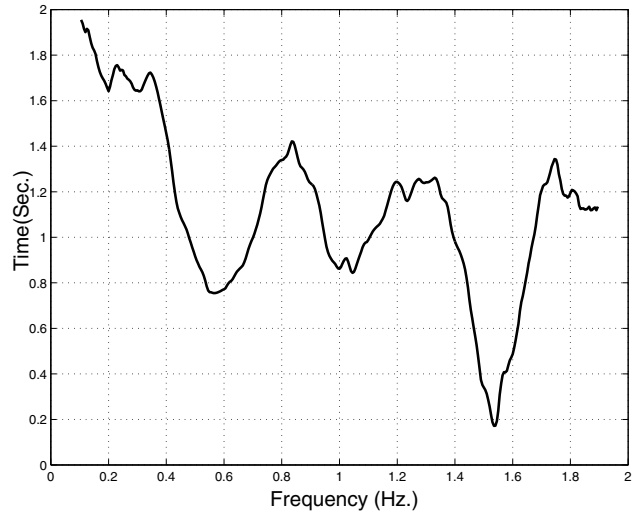
Figure 7.9: Difference of probe 2 and probe 1 group delay estimation
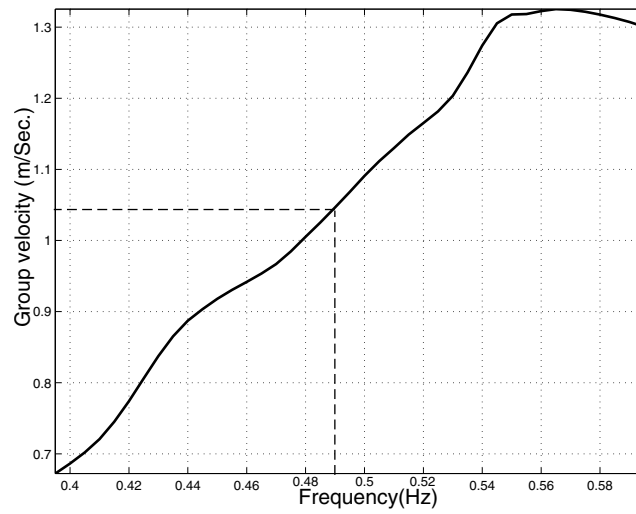
Figure 7.10: Localized group velocity estimation via RID

150

estimate the group velocity, we utilize Eq. (7.12), where $\Delta z = 1$ meter, and Δt_g is plotted in Fig 7.9. The resultant group velocity is shown in Fig. 7.10. Note that group velocity at 0.492 Hz is 1.03 (m/sec.) which is entered into Table 7.2.

7.4.2 Fourier Analysis

In this section we will employ classical Fourier analysis to calculate phase and group velocities based on the cross power spectrum of the ocean wave time series provided in Fig. 7.2. The frequency of interest can be obtained by the power spectrum of the time series provided in Fig. 7.4 such that $\omega = 2\pi \times 0.5$ Hz. Recall that the phase of the cross power spectrum preserves phase information in the form of phase difference [69]. If the phase difference is denoted by $\phi(\omega)$, then we can determine the wave number $k(\omega)$, from $k(\omega) = \phi(\omega)/\Delta z$. The dispersion relation is provided in Fig. 7.11, we find that the phase and group velocity estimates are given by:

$$v_{ph} = \frac{\omega}{k} = \frac{3.14(\text{rad./sec.})}{1(\text{rad./m})} = 3.14(\text{meter/sec.}) \tag{7.13}$$

$$v_g = \frac{\partial \omega}{\partial k} = \frac{4.46(\text{rad./sec.})}{3(\text{rad./m})} = 1.48(\text{m/sec.}) \tag{7.14}$$

In calculating the Fourier-based cross-power spectrum, we utilize the entire time series records shown in Fig. 7.2. The Fourier-based results for phase and group velocity are tabulated in Table 7.2, which will be discussed later.

7.4.3 Wave Theory

In addition to using the Fourier based approach to check our time-frequency estimates of phase and group velocity [85], we calculate phase and
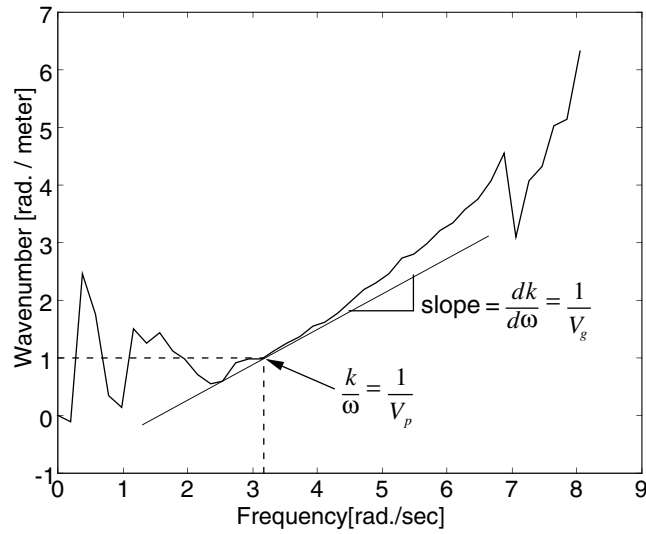
Figure 7.11: Phase difference of two wave time series by Fourier cross power transform

group velocities from wave theory [86]. For a deep water model, the following approximation of the wave length is defined:

$$\lambda = \frac{gT^2}{2\pi}\tanh(kh) \tag{7.15}$$

In this expression, h is the depth of the water, and g is the gravitational acceralation constant and T is the wave period. In our case, $k \cong 1$ at 0.5 Hz, $h = 5.8$ meters, and $\tanh(kh) = 0.999$. Thus,

$$\lambda \cong g\frac{T^2}{2\pi} = 9.80(\text{m/sec.}^2) \cdot \frac{2^2(\text{sec.}^2)}{2\pi} = 6.24(\text{m}) \tag{7.16}$$

In our analysis, 0.5Hz is the peak frequency component, $T = 2(\text{sec.})$. Therefore, the corresponding wave number is

$$k = \frac{2\pi}{\lambda} = 1.01(\text{rad./m}) \tag{7.17}$$

152

Table 7.2: Comparison of the estimation of phase velocity and group velocity with different methods

	Localized analysis(G_5)		Entire time series		
method	RID	Cross TFD	Fourier analysis	Wave theory	Weighted average Cross TFD
phase velocity	N/A (m/sec.)	3.22 (m/sec.)	3.14 (m/sec.)	3.11 (m/sec.)	3.12 (m/sec.)
group velocity	1.03 (m/sec.)	0.94 (m/sec.)	1.48 (m/sec.)	1.55 (m/sec.)	1.32 (m/sec.)

The phase velocity is determined from

$$v_{ph} = [\frac{g}{k}\tanh(kh)]^{\frac{1}{2}} \cong [\frac{g}{k}]^{\frac{1}{2}} \tag{7.18}$$

$$v_{ph} \approx [\frac{9.8 \text{ (m/sec.}^2)}{1.01 \text{ (rad./m)}}]^{\frac{1}{2}} = 3.11(\text{m/sec.}) \tag{7.19}$$

The group velocity is defined as follows:

$$v_g = \frac{1}{2}v_{ph}[1 + \frac{2k \cdot h}{\sinh(2k \cdot h)}] \simeq \frac{1}{2}v_{ph} = 1.55(\text{m/sec.}) \tag{7.20}$$

7.4.4 Summary and Comparison

In Table 7.2, results of phase and group velocity calculations with different techniques discussed in previous sections are provided. By and large, the techniques are divided into localized analysis and entire time series analysis. The objective of comparing the classical RID and cross time-frequency distribution is to find consistency in time-frequency techniques for localized analysis. Even though phase velocity is not available via RID, the results for group velocity by cross time-frequency (0.94 m/sec.) and by RID (1.03 m/sec.) are reasonably close. This implies that the group delay of a non-stationary

153

signal can be alternatively obtained from the cross time-frequency distribution, if the signal pair is available. Note that for the localized wave group G_5, we applied the same local frequency of 0.492 Hz and RID kernel for both the auto and cross time-frequency distribution.

To compare the results from Fourier analysis and wave theory, it is not reasonable to select a specific wave group result. Instead, the weighted average values of phase and group velocities by energy fraction in Table 7.1 are used in Table 7.2. The Fourier analysis and wave theory results are based on different approaches, however, they show fairly close values. In addition, those results are also close to the result of weighted average. Reflecting on the marginal properties of time-frequency distributions, we conclude that the consistency is reasonable. The analysis of dispersive wave propagation via cross time-frequency distribution discussed in Sec. 7.4 shows consistent result with traditional time-frequency distributions and also with traditional Fourier-based cross-power analysis and wave theory when we take a weighted average using local energy fraction.

7.5   Conclusion

The goal of this chapter is to investigate the feasibility of using cross time-frequency techniques to make time-localized measurements of phase and group velocities. A most encouraging result, in our opinion, is the cross time-frequency distribution which we presented in Sec. 7.3. The cross time-frequency distribution is capable of preserving phase difference information as a function of frequency and time. Using time localization via the instantaneous phase difference, the local phase difference spectrum is obtained, then the local

frequency is utilized to calculate phase and group velocities for that frequency. The local analysis shows results consistent with classical time-frequency distribution that utilizes group delay estimation. In addition, the weighted average of the localized analysis also shows consistency with classical Fourier analysis and wave theory. These consistencies between the cross time-frequency analysis and other alternatives indicates that the localized dispersion analysis via cross time-frequency analysis is a reasonable treatment. Therefore, cross time-frequency analysis can be utilized for the transient phase difference estimation for non-stationary signals. It is clear that time-frequency dependent phase difference information is advantageous aspect, however, as shown in Sec. 7.4, the selection of the proper time and frequency for the evaluation is critical.

In conclusion, we have presented what we believe to be the first attempt to utilize time-frequency techniques to estimate time-localized phase and group velocities. We introduced the new cross time-frequency distribution whose phase and group velocity results, although not in "perfect" agreement with Fourier-based and theoretical values, are sufficiently encouraging to warrant further investigation.

Chapter 8

Application of Cross Time-Frequency Analysis to Postural Sway Behavior: the Effects of Aging and Visual Systems

8.1 Introduction

Posture control is an essential part of life which is associated with all aspects of daily activities. Malfunction of postural control can cause many problems and accidents such as falls. The rate of accidents or mortality from traumatic falls is a manifestation of such problems. Statistical evidence indicates that a third of elderly Americans over 65 years old experience injury from falls annually, while 32% of aged Americans over 85 years old die from traumatic falls [87][88]. Annual health care costs related to falls are about $37 billion, which is somewhat close to the $47 billion cost of motor vehicle injuries [89]. So there is a need to investigate and quantify elderly postural control to find early indicators of these deficits; hence, various work is ongoing relating to modelling of posture control and developing appropriate analysis techniques for postural sway [90].

The effects of aging and the feedback from sensory systems can be modelled with control system and signal processing techniques. In order to describe and represent the human postural sway control mechanism as a control system, various types of modelling have been carried out using feedback control systems models [91], stochastic models [92] and biomechanical models [93]. It

156

is not a simple task to characterize postural sway signals in either the time domain or frequency domain due to the fact that the postural sway signals are highly transient and non–stationary. Therefore, time-frequency analysis has recently been utilized to analyze postural sway [94]-[95]. The classical time-frequency distribution can successfully provide time- and frequency- localized information of postural sway signals [96]-[95]; however, the classical time-frequency distribution is usually limited to a single nonstationary time series of interest so that it cannot analyze multiple related signals in terms of phase difference, for example.

Therefore, the purpose of this chapter is to investigate the effects of visual feedback and aging on postural sway systems and signals by analyzing the transient phase difference between "input" and "output" which correspond to center of pressure (COP) and center of mass (COM), respectively. In this chapter, the investigation of postural sway signals mainly relies upon a relatively new cross time-frequency analysis technique that provides time- and frequency-localized phase difference information [41]. The localized (in time and frequency) phase difference patterns of postural sway signals are compared in the experiments under different aging and sensory conditions.

8.2   System Modelling of Postural Sway and Sensory Feedback

Consider a block diagram model of the sensory feedback system for postural coordination provided in Fig. 8.1. This is a modified version of Nashner's Model of postural control [97]. Unlike his model, we have added a divided response system to central nervous system (CNS) activation. The postural sway control process is represented in terms of input (an ankle moment

u) and output (COM) between a posture dynamic system with a compensator. The dashed portion of the block diagram is not directly accessible to obtain time series data, however, it determines the control process of posture.

The input of the posture dynamic system is COP and the output Θ, the sway angle of the body. The sway angle of the body, Θ, yields the COM signal as an output of the body system. The posture dynamic system is frequently modelled as an inverted pendulum [91] which is unstable in nature. For the stabilization of the posture dynamic system, a posture controller is required [98]. The muscles play a role as a compensator to stabilize the posture dynamic system by a command from CNS. Note that the parameters of the posture controller adaptively change depending on the command from CNS for stabilization. In addition, as depicted in Fig. 8.1, the input to the posture dynamic system COP is determined by the ankle moment u and command from CNS, which is affected by the sensory system. Comparing the instantaneous COM and the desired position (equilibrium state in this chapter), the sensory system affects the command from CNS. Note that the operation of the CNS commands is to stabilize the posture dynamic systems by minimizing the displacement of position, i.e., COM.

For the stabilization of the posture dynamic system, various sensory systems are activated. It is known that visual, somatosensory and vestibular sensory components are the influencing factors in the stabilization process or for the control of balance. We suggest that the existence of a posture controller which can be interpreted as a lead compensator; a lead compensator model has been employed in the modelling of the human postural dynamics [91], [99]. Based on the fundamental feedback system design theory, a lead compensator provides an enhanced transient damping in the time domain and increased phase margin in the frequency domain so that the closed-loop feed-

158
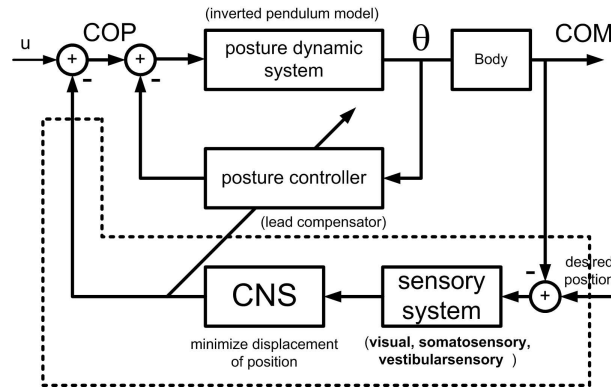
Figure 8.1: Simplified proposed model of the sensory feedback system for postural coordination.

back system's transient response is stabilized [100], [101]. In addition, a lead compensator results in an increased frequency bandwidth compared to the inertial responses of the body to gravity, i.e., COM, which gives rise to faster response times. Therefore, the status of the feedback posture control process is well reflected by the COP and COM signals.

However, the postural signals are highly transient, hence the investigation of the phase difference via classical Fourier-based analysis is not appropriate. Fourier-based spectral analysis has been frequently used for analyzing postural sway signals or systems, because Fourier-based spectral analysis is sufficient to describe most dynamic systems in the frequency domain. However, this analysis technique has not always proven acceptable because it assumes that the postural signals are stationary. Thus in the next section, we will overview classical time-frequency analysis which will be later used to identify the principal time interval and frequency ranges of interest. Next we will introduce our new analysis approach using cross time-frequency distributions which will be used later to determine the estimates of phase difference.

159

8.3 Experimental Setup and Data Measurement

In this section, the physical experimental setup to investigate the effects of aging and sensory (especially visual) conditions on the postural sway feedback control systems is described. Previous work by others [102]-[103] analyzed COP signals via random-walk analysis for the effects of age and visual sensory system, while our study differs in that it investigates the input-output relation by measuring time-localized phase difference between COP and COM via cross time-frequency analysis.

Two groups of 15 volunteer participants per group are used for the experiments: 15 elderly individuals (65–75 years old) and 15 young individuals (20–30 years old). The postural sway data are collected for the following four experimental conditions:

- Case 1: Young person with eyes open,

- Case 2: Young person with eyes closed,

- Case 3: Elderly person with eyes open,

- Case 4: Elderly person with eyes closed.

The standard of analysis used biomechanical constructs such as COP and COM to describe the oscillations or postural sway of the body over its base of support. COP is the kinetic summary of all ground reaction forces of the feet in contact with the support surface while COM is the kinematic summary of all the body mass in response to gravity. It is well established that postural sway can be represented using a summary pressure point for the ground reaction forces on a force platform [87] [88]. While each participant stood on a split

160
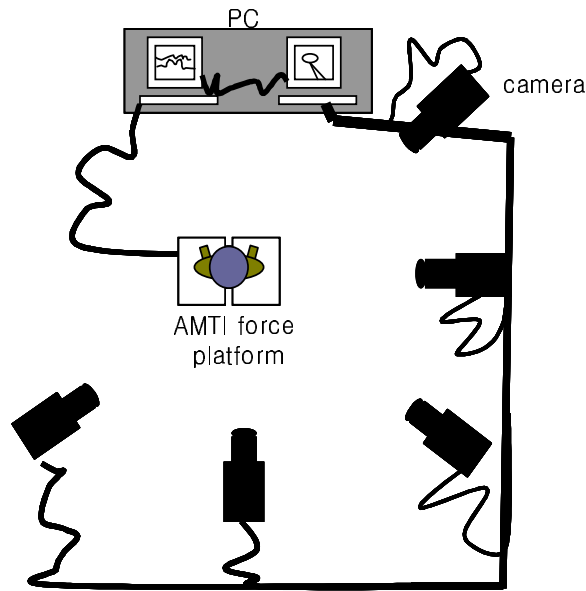
Figure 8.2: Laboratory setup of postural sway data acquisition (Aerial View).

force platform, the COP was used to represent the body's sway. In addition, a reflective marker on the sacral region of the back was used as a kinematic summary point representing the movement of the body in 3–D Cartesian space and was used to calculate movement patterns of the COM.

Fig.8.2 describes the experimental setup for the postural signal acquisitions. COP and COM signals were collected using two AMTI force platforms and a 3-D video motion analysis system with a 5-camera setup [93], respectively. The left force platform measured left COP (COP_L), the right force platform measured right COP (COP_R), while the COM is calculated with the use of a seven segment anthropometric model. The 5-camera system was set up at visual angles so that the location of 12 passive markers could be easily tracked over time. The COM was calculated from these spatial coordinates. These data were collected for 60 second trials with a sampling rate of 60Hz.

The collected data time series was down sampled during post-processing to 30 samples/sec. Data from only 1 sec. to 59 sec. was used in this experiment to reduce the noise artifacts from data initiation and cessation.

Either COP_L or COP_R could be investigated with the COM because COP_L and COP_R have out-of-phase characteristics with respect to each other. Research indicates that the COP_L and COP_R behave in anti-phase patterns representing a postural strategy of "load-unload" on each lower limb. According to Winter [104] this strategy provides a timed, equal and opposite activation of motor systems in response to the body's reaction to medial-lateral sway. The degree to which the COP_L and COP_R behave in relationship to each other can indicate changes in motor responses due to factors such as aging or available sensory feedback such as vision. For the purpose of this chapter, we took the combined movement of COP, i.e., the differential COP to compare with COM movement to represent control of posture during quiet standing. Therefore, we define a differential COP, COP_d as follows:

$$COP_d = (COP_R - COP_L)/2 \qquad (8.1)$$

So COP_d is used in this chapter to minimize the error or any bias in the data.

8.4   Results

In this section, the effects of aging and available visual sensory feedback are demonstrated using the transient phase difference spectrum which is obtained using cross time–frequency analysis. Therefore, we will first discuss time-frequency localization via classical time-frequency distribution.

8.4.1 Time and Frequency Localization of the Postural Signals via Reduced Interference Distribution (RID)

In this section, classical time-frequency distributions of the postural sway signals are discussed. Among the various types of time-frequency distributions in Cohen's class, the reduced interference distribution (RID) [6], which is used in this chapter, achieves high-resolution with highly reduced cross terms or interference activity, and preserves many desirable properties of the time–frequency distribution function. This is the reason why RID is frequently employed in the application to and interpretation of biological signals [105]. In Figs.8.3–8.6, the RID time-frequency distributions (TFDs) of COP_d and COM for the most typical representative samples from the experiments discussed in Sec. 8.3 are provided.

Fig.8.3(a) and Fig.8.3(b) show COP_d and COM of a young person with eyes open (Case 1). The figures indicate that the energy density of COP_d and COM is clustered at around 10 sec. in time and below 0.2Hz. Fig.8.4(a) and Fig.8.4(b) illustrate the COP_d and COM of a typical young person with eyes closed (Case 2). The figures show the local energy density is concentrated at around 16 sec. for COP_d and at around 10 sec. for COM in time, and below 0.07 Hz in frequency. Comparing the TFDs in Fig. 8.3 and Fig. 8.4, one can observe significant difference of patterns in the time-frequency plane: more higher frequency components are observed in Fig. 8.3 than Fig. 8.4. In addition, the TFDs of COP_d and COM in Fig. 8.3 exhibit good pattern agreement on time-frequency plane, however, this is not the case for the TFD's in Fig. 8.4.

Fig.8.5(a) and Fig.8.5(b) show the TFDs of COP_d and COM of a typical elderly person subject sample with eyes open (Case 3). The maximum local energy densities are located at around 11 sec. in time and below about

0.1 Hz in frequency. Fig.8.6(a) and Fig.8.6(b) illustrate the time-frequency distributions of COP_d and COM, respectively, of a typical elderly person with eyes closed (Case 4). The TFDs in Fig.8.6 show that the local energy density of COP_d and COM is concentrated at around 10 sec. in time and below 0.10 Hz in frequency. The TFDs in Fig. 8.5 show slightly more time-frequency components than the TFDs in Fig. 8.6, however, the dominant patterns located at approximately 10 sec. on the time-frequency plane are quite similar.

Table 8.1 provides the RMS value of displacement and localized characteristics of the postural sway signals in terms of the time center, time duration, frequency center and frequency bandwidth from the TFDs provided in Figs.8.3–8.6. The time center and time duration are obtained from the first and second order moments of the time-frequency distribution in time domain, respectively. Likewise, the frequency center and bandwidth are obtained from first and second order moments of the time-frequency distribution in the frequency domain [2]. The ability to calculate various moments and conditional moments from knowledge of the TFD is an important advantage of time-frequency analysis. The time and frequency parameters provided in Table 8.1 are calculated using standard equations in [96], [2]. Observation of the TFDs in Fig.8.3–Fig.8.6, irrespective of the different cases, reveals the fact that the postural sway signals are highly transient and thus non-stationary and have a low-frequency dominance.

The RMS value of displacement provided in Table 8.1 shows a clear distinction between young and elderly participant samples. The RMS values of displacement for the young participant are approximately 3-5 times less than those of the elderly participant. In addition, open eye conditions for both young and elderly samples exhibit smaller RMS values of displacement.

On the other hand, frequency center and frequency bandwidth show

164
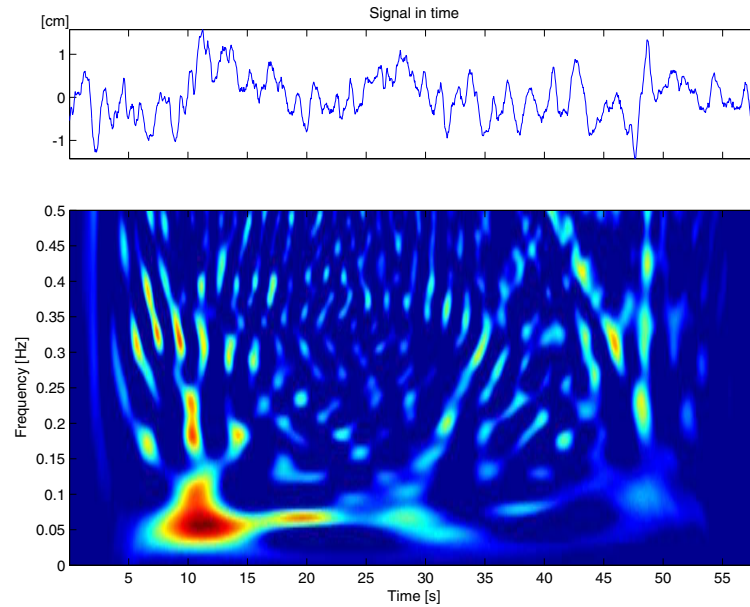
(a) Center of pressure
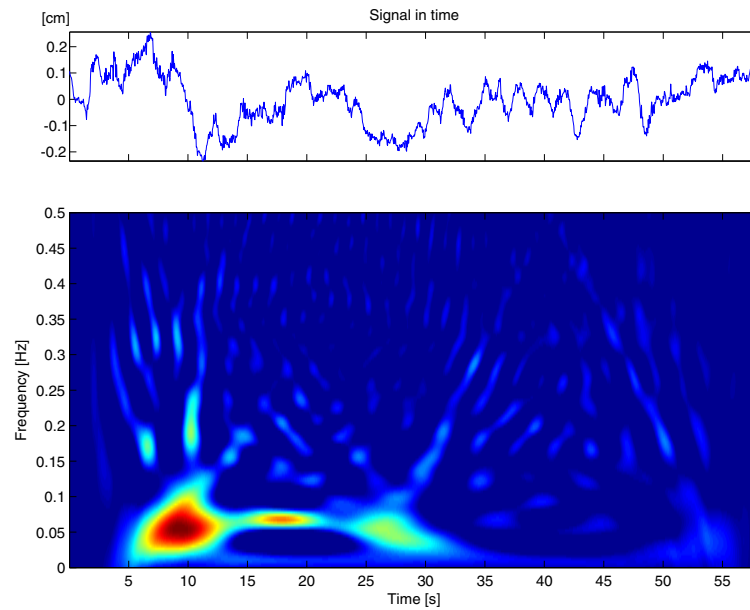
(b) Center of mass

Figure 8.3: Young person with eyes open (Case 1), time series and time-frequency distribution for (a) COP_d, and (b) COM.

165
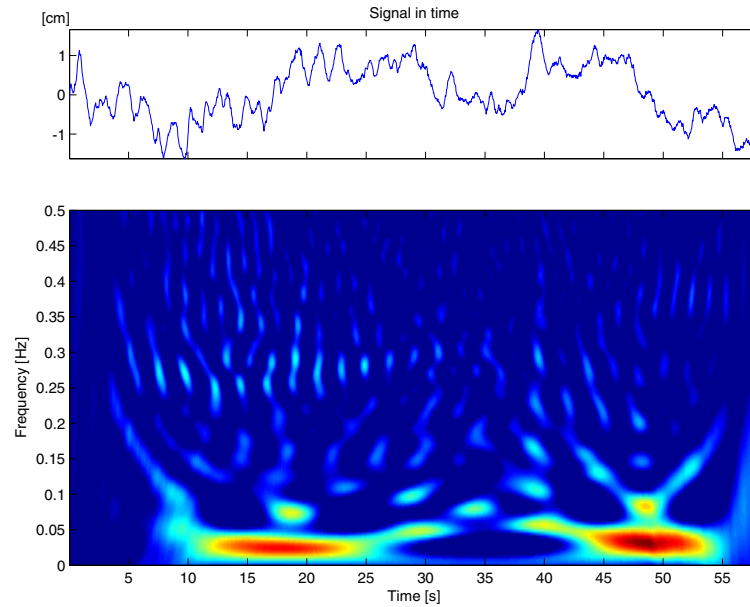
(a) Center of pressure

(b) Center of mass

Figure 8.4: Young person with eyes closed (Case 2), time series and time-frequency distribution for (a) COP$_d$, and (b) COM.
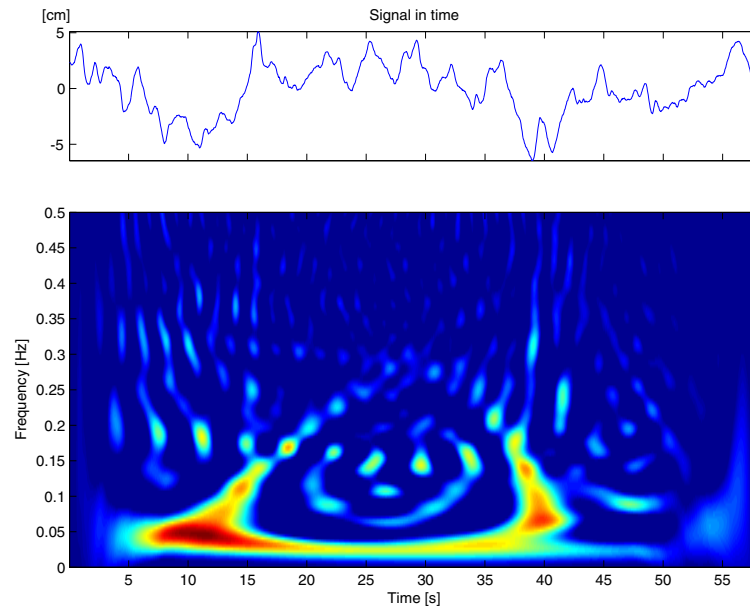
(a) Center of pressure
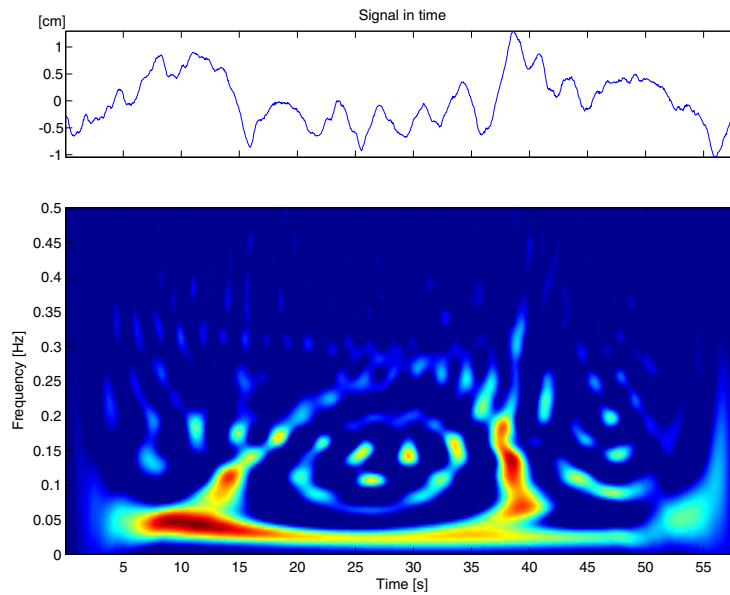
(b) Center of mass

Figure 8.5: Elderly person with eyes open (Case 3), time series and time-frequency distribution for (a) COP_d, and (b) COM.

167
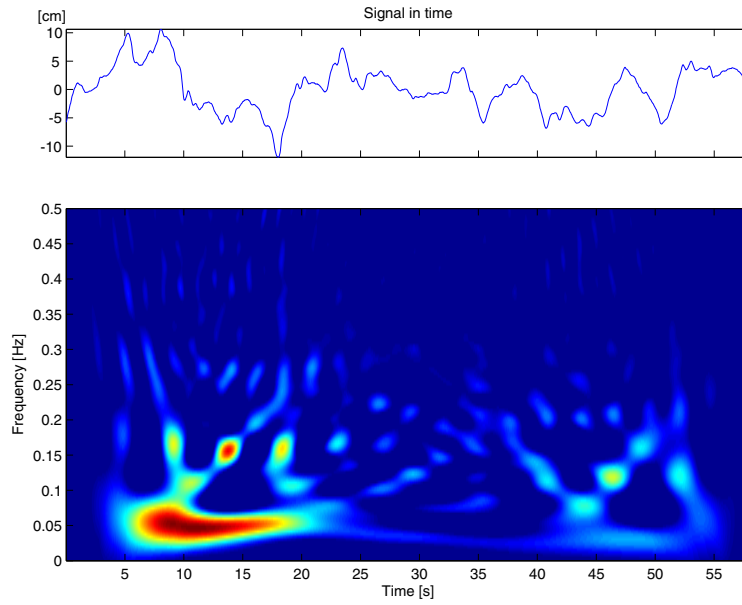
(a) Center of pressure
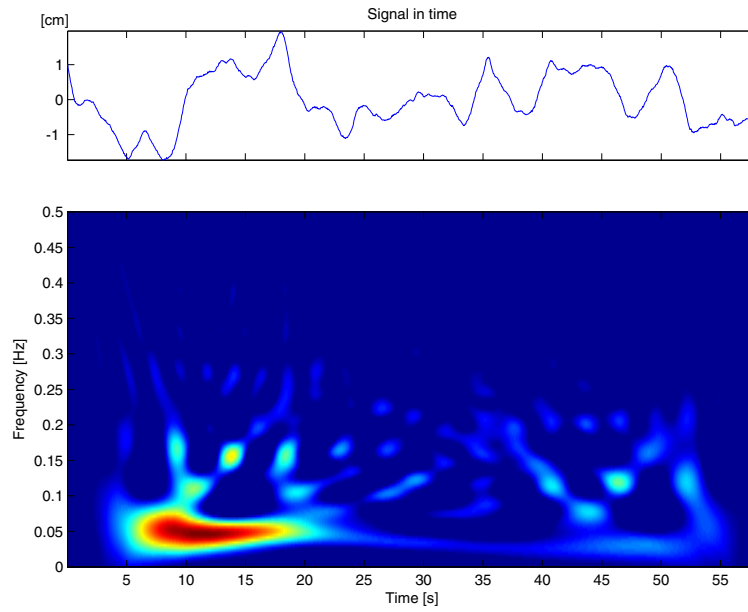
(b) Center of mass

Figure 8.6: Elderly person with eyes closed (Case 4), time series and time-frequency distribution for (a) COP_d, and (b) COM.

168

Table 8.1: Sample participant data indicating RMS displacement characteristics for COP and COM signals and localized time center, time duration, frequency center and frequency bandwidth of the time-frequency distributions provided in Fig.8.3 – Fig.8.6 (Dimensions of displacement, time and frequency are cm., sec., and Hz., respectively.)

Experiment Condition	Young Participants				Elderly Participants			
	Open Eyes		Closed Eyes		Open Eyes		Closed Eyes	
	COP_d	COM	COP_d	COM	COP_d	COM	COP_d	COM
RMS Displacement	0.53	0.09	0.76	0.36	2.3466	0.47	4.26	0.81
Time Center	10.41	9.55	15.77	9.60	10.83	10.98	9.40	9.54
Time Duration	1.96	2.08	2.76	2.65	2.67	2.76	2.14	2.15
Freq. Center	0.18	0.13	0.06	0.02	0.06	0.04	0.08	0.06
Freq. B.W	0.14	0.14	0.08	0.06	0.06	0.04	0.08	0.06

an opposite pattern: the young participant with open eye sample has higher center frequency and frequency bandwidth than the elderly participant with open eye sample. The pattern does not directly hold for the closed eyes samples of young and elderly participant, since both of them have very small and somewhat comparable values of center frequency and frequency bandwidth. Typically, the localized time duration of a signal is inversely proportional to the localized frequency bandwidth. Hence, a distinctively smallest localized time duration is obtained for young participant sample with open eyes compared to all the other samples.

The information provided in Table 8.1 provides a good synopsis of the features of the transient nature of postural signals. Also the quantitative pattern of RMS values, time duration, center frequency and frequency band-

169

width show distinctive differences between young vs. elderly, and open eyes vs. closed eyes. However, the analysis based on classical time-frequency analysis is not enough to analyze the internal postural sway control process discussed in Sec. 8.2 in terms of COM and COP_d in an associated manner. Therefore, we will discuss the time-frequency localized phase difference relation between the COP_d and COM via cross time-frequency analysis in next section. Note that the time and frequency localization discussed in this section is a basis for the localized phase difference discussed in next section.

8.4.2 Calculation Process for Time-Frequency Localized Phase Difference

In this section, the calculation process for the time-frequency localized phase difference is discussed. In Fig. 8.7, an algorithmic flow chart of the calculation process of the time-frequency localized phase difference is provided. The process depicted in Fig. 8.7 is divided into the (auto) time-frequency analysis depicted on the left side of Fig. 8.7 and cross time-frequency analysis depicted on the right side of Fig. 8.7. The parameters obtained by the (auto) time-frequency analysis determine the time and frequency localization of the time-frequency phase difference. In Fig. 8.7, the COP_d signal corresponds to the signal x_1 in Eq. (2.19) while the COM signal corresponds to the signal x_2 as indicated in Fig. 8.7. In order to relate COP_d and COM signals, refer to the cross time-frequency distribution in Eq. (2.19) and its time-frequency phase difference spectrum, which measures phase difference between the COP_d and COM as a function of time and frequency. As discussed in Sec. 8.2, the phase difference is important information since it provides insight into the characteristics of the feedback control process in postural sway.

However, as the time-frequency phase difference spectrum, $\Theta_{x_1 x_2}(t, \omega; \phi)$

170

is function of time and frequency simultaneously, it is necessary to localize the time and frequency of interest. For the time and frequency localization, the classical time-frequency distributions of COP_d and COM signals are calculated, as depicted on the LHS of Fig. 8.7. For the time localization, a specific time interval of interest, denoted as $([t_0 - T_0/2, t_0 + T_0/2])$, is selected considering the time localized energy with fixed duration T_0, in which the local energy of the signal is maximum such that:

$$t_0 = \arg \max_{t \in [0,T]} \left\{ \int_{t-T_0/2}^{t+T_0/2} \int C_x(t,\omega) d\omega dt \right\} \tag{8.2}$$

Strictly speaking, t_0 is different from the time center provided in Table 8.1; however, numerically the values are quite close. Note that the fixed duration T_0 is selected as 10 sec. to accommodate the localized time durations of the COM and COP_d signals. Also, the selection of t_0 is determined by the COP_d signal which corresponds to the input to the postural sway control process in Fig. 8.1.

Then, the extracted time–localized average phase difference is obtained as a function of frequency over the specific time-interval of interest, $(t_0 - T_0/2, t_0 + T_0/2)$,

$$\varphi_{x_1 x_2}(\omega) = \frac{1}{T_0} \int_{t_0 - T_0/2}^{t_0 + T_0/2} \Theta_{x_1 x_2}(t, \omega; \phi) \ dt \tag{8.3}$$

where t_0 is from (8.2) and T_0 is 10 secs. As each experimental condition has 15 individuals, the mean and standard deviation of the phase difference spectrum is evaluated at each frequency of interest. After determining the time instance of interest t_0, one can similarly evaluate the frequency center ω_{x_1} of interest

171
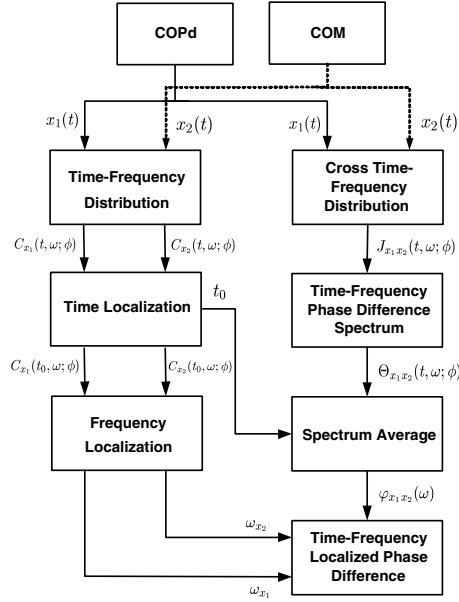
Figure 8.7: An algorithmic flow chart of time-frequency localized phase difference evaluation

at this time as follows:

$$\omega_{x_1} = \frac{\displaystyle\int \omega C_{x_1}(t_0, \omega) d\omega}{\displaystyle\int C_{x_1}(t_0, \omega) d\omega} \tag{8.4}$$

The frequencies of interest are evaluated for the COM and COP_d signals individually for the localization of the time-frequency phase difference spectrum. Finally, the time-frequency localized phase difference can be evaluated for the frequency of interest. The calculation process described in this section will be applied to the four different cases in next section.

8.4.3 Results and Discussion of the Time-Frequency Localized Phase difference

In this section, we discuss the time and frequency localized phase difference of the postural sway experiments. Figs. 8.8 –8.10 show the mean values (for 15 subjects) and the standard deviation of the time-localized phase difference spectrum obtained by Eq. (8.3) from 15 individual subjects for Cases 1 - 4. In each figure, the center frequency of COP_d and COM are indicated where the indicated center frequency corresponds to the mean value corresponding to the fifteen subjects. Consider the time-localized phase difference for Case 1 (young persons with eyes open) in Fig. 8.8. The mean values for the center frequency are 0.1844 Hz for COP_d, and 0.1368 Hz for COM, respectively. (These and other values for subsequent cases are tabulated in Table 8.2 for convenience and later discussion.) The values for the phase difference at the center frequency of COM and COP_d are 1.7436 rad., 1.2708 rad., respectively. In order to see the effects of visual feedback on the postural sway control process, compare the localized phase difference spectrum of Case 1 in Fig. 8.8 with Case 2 in Fig. 8.9. In Fig. 8.9, the time-localized phase difference for Case 2 (young persons with eyes closed) is provided. The mean values for the center frequency COM and COP_d show comparatively larger discrepancy (0.1298 Hz for COP_d and 0.0552 Hz for COM) than Case 1. The average phase difference for the frequency range from 0 Hz to 0.5 Hz shows a random-like pattern with a large standard deviation. All the estimated phase differences at the center frequencies of COM and COP_d are close to zero, -0.2275, 0.0350 radians, respectively. Comparisons of the phase difference spectra in Figs. 8.8 and 8.9 indicates that the influence of visual feedback (Case 1) results in a larger value of phase difference than without vision available (Case 2).

173
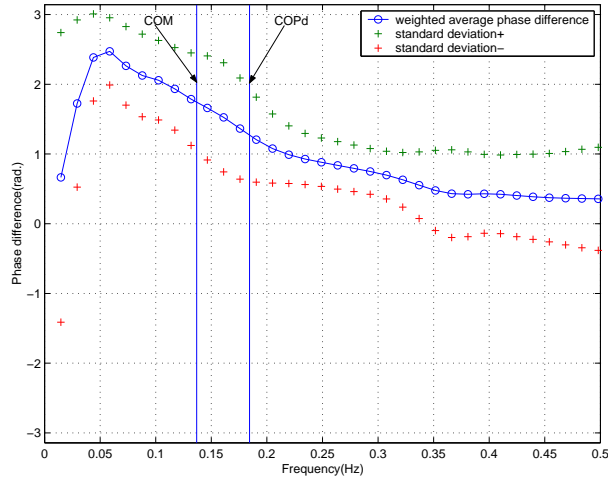
Figure 8.8: Mean and standard deviation of time-localized phase difference for Case 1 (young persons with eyes open).
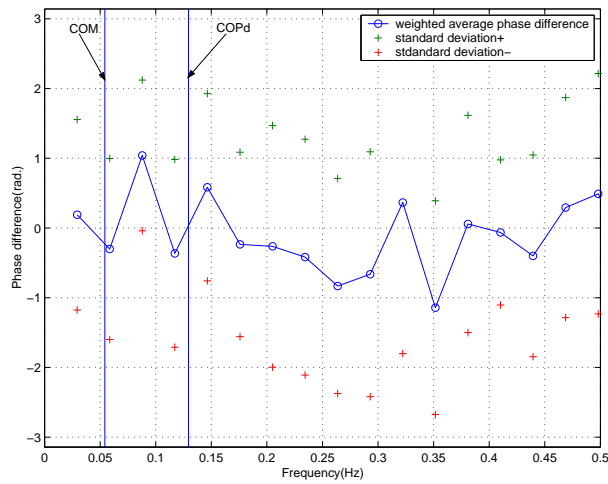
Figure 8.9: Mean and standard deviation of time-localized phase difference for Case 2 (young persons with eyes closed).

174
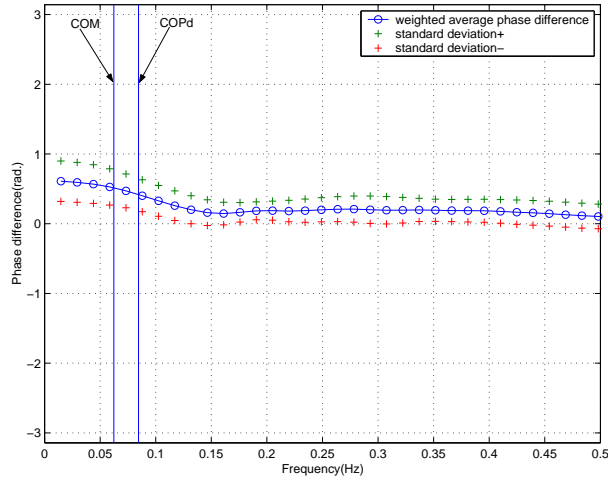
Figure 8.10: Mean and standard deviation of time-localized phase difference for Case 3 (elderly persons with eyes open).
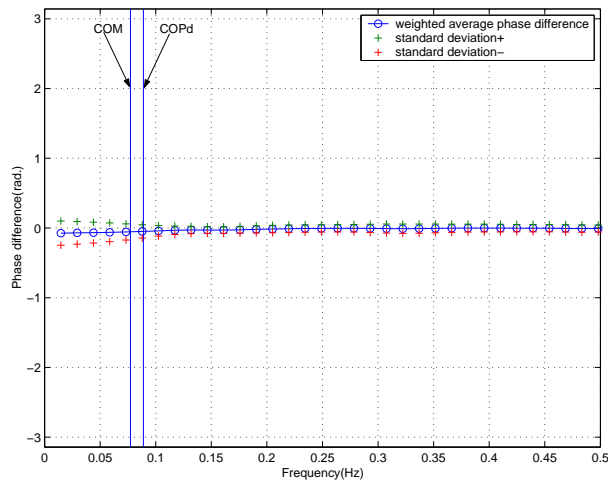
Figure 8.11: Mean and standard deviation of time-localized phase difference for Case 4 (elderly persons with eyes closed).

175

The different patterns for the phase difference spectra between Fig. 8.8 and Fig. 8.9 can be interpreted by the operation of the feedback control process discussed in Sec. 8.2: a proper sensory (vision in this chapter) feedback process for postural sway results in a time delay which results in an increased phase difference with a lead compensator [99]. As discussed in Sec. 8.2, the role of the lead compensator is to improve damping of the transients by increasing the phase margin. It is a notable fact that the frequency range of operations of the of visual sensory system is known to be 0.1-0.2 Hz where the center frequency of COM, COP_d are located, as indicated in Fig. 8.8.

Another distinctive different pattern for the phase difference spectra between Fig. 8.8 and Fig. 8.9 is the random-like phase difference with a large standard deviation in Fig. 8.9. Refer to the representative example of the RID time-frequency distributions of COP_d and COM for Case 2, provided in Fig. 8.4 and the corresponding parameters provided in Table 8.1; the time-frequency distributions of COP_d and COM are not matched in comparison with the other Cases 1,3 and 4. The time and frequency index of the peak value of the time-frequency distributions in COP and COM are different. Comparing the time-frequency distributions of COP_d and COM in Fig. 8.4, one immediately observes that the TFDs are quite different and thus there is little common signal at any given time and frequency point. Thus, the calculation of the phase difference at each time-frequency point exhibits a large variance as shown in Fig. 8.8.

Now, consider the effects of visual sensory feedback in elderly participants, i.e., Cases 3 and 4. In Fig. 8.10, the time-localized phase difference for Case 3 (elderly persons with eyes open) is provided. The phase difference shows relatively small values below 0.1 Hz; moreover, the value of phase difference decays to zero above 0.1 Hz with very small standard deviations.

176

The phase differences at the center frequency of COM (0.0623 Hz) and COP_d (0.0845 Hz) are 0.5132 radian and 0.4178 radian, respectively. In Fig. 8.11, the time-localized phase difference for Case 4 (elderly persons with eyes closed) is provided. The plotted phase difference is very close to zero with a very small standard deviation over the entire frequency range. The phase differences at the center frequency of COM (0.0773 Hz) and COP_d (0.0889 Hz) are very close to zero (-0.0554 radian and -0.0486 radian, respectively). Both of the phase difference spectra of elderly participants with and without visual sensory provided in Fig. 8.10 and Fig. 8.11, respectively, exhibit very small values compared to the young participants. The existence of the visual sensory in Fig. 8.10 results in a comparatively larger phase difference values than without the visual sensory in Fig. 8.11. This pattern also corresponds to the observations of the localized phase difference in young participants (Case 1 and Case 2).

In the case of elderly individuals in this experiment, both Case 3 and Case 4 show a week feedback control process with the measured phase differences with open eyes (Case 3) being slightly higher than those with closed eyes (Case 4). These small values of phase difference indicate that there exists no significant time delay in Case 4. This can be interpreted as a "drifting" state or constant slow movement from an initial position, which implies decreased use of feedback control process. Persons with decreased feedback control of the postural system are more susceptible to external forces (gravity, stiffness of system, etc.) due to limited resources (sensory information, strength etc.). These individuals produce less of a counteracting, correcting force to control posture and are, therefore, less variable and more in-phase in all inertial biological behaviors in response to gravity.

In order to compare the effects of aging and visual sensory on postural

177
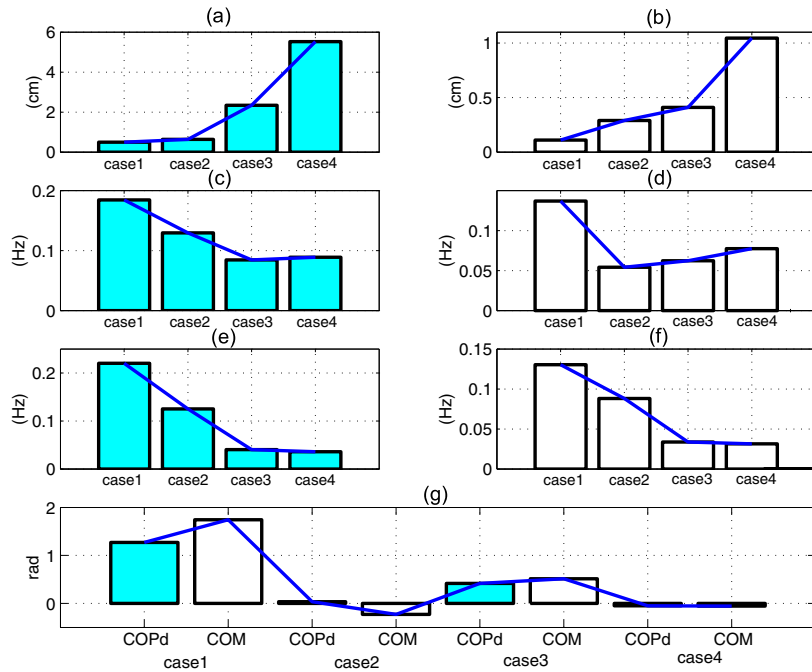
Figure 8.12: Amplitude and phase difference analysis for case 1,2,3 and 4 with mean: (a) RMS values of COP_d data, (b)RMS values of COM data, (c) Center frequency of COP_d, (d) Center frequency of COM, (e) Frequency bandwidth of COP_d, (f) Frequency bandwidth of COM and (g) Phase difference measured at COP_d and COM

sway control, a summary analysis is provided in in Table 8.2. The experimental results in Table 8.2 are assorted in terms of amplitude, frequency and phase difference for the four different conditions (Case 1- 4) of aging and visual sensory. Note that the numbers in Table 8.2 are the group mean and standard deviations for 15 young and 15 elderly subjects, while the numbers in Table 8.1 are the values for single representative participant. In order to visualize the patterns of the items in Table 8.2 and their dependence on the experimental conditions, a set of bar graphs is provided in Fig. 8.12.

The RMS values for both COP_d and COM signals in Table 8.2 and

Table 8.2: Group mean values and standard deviations for case 1,2,3 and 4 with regard to amplitude, frequency and phase difference analysis

Experimental condition			Amplitude		Frequency		Phase
Age	Eyes	Signal	Mean RMS	Std. Dev.	Center Freq.	Freq. B.W.	Phase (radian)
Young	Open (Case 1)	COP_d	0.49	0.02	0.18	0.22	1.27
		COM	0.11	0.04	0.13	0.13	1.74
	Closed (Case 2)	COP_d	0.63	0.01	0.12	0.12	0.03
(N=15)		COM	0.28	0.01	0.05	0.08	-0.22
Elderly	Open (Case 3)	COP_d	2.34	0.07	0.08	0.04	0.41
		COM	0.40	0.02	0.06	0.03	0.51
	Closed (Case 4)	COP_d	5.52	0.04	0.08	0.03	-0.04
(N=15)		COM	1.04	0.09	0.07	0.03	-0.05

Fig. 8.12-(a), (b) show a clear distinction depending on age, i.e. smaller RMS value of displacement for young (Case 1 and 2) than elderly cases (Case 3 and 4). The RMS values of displacement are a strong indicator of stability in postural sway which is to be minimized as much as possible via the operational commands from CNS. In accordance with this concept, the young group (Case 1 and 2) demonstrated a more stabilized postural sway than the elderly group (Case 3 and 4). Also, the patterns of center frequency and frequency bandwidth in Table 8.2 and Fig. 8.12-(c) ∼ (f) show another clear distinction depending on age in terms of frequency. Larger center frequencies and frequency bandwidths are obtained for young (Case 1 and 2) than elderly cases (Case 3 and 4). Younger persons were able to monitor posture more frequently (with higher frequency and with higher frequency bandwidth) while the elderly participants make less frequent postural adjustments with a lower center frequency and smaller frequency bandwidth.

The effects of visual feedback is more distinctive in the phase difference results in Table 8.2 and Fig. 8.12-(g). The existence of visual sensory (Case

1 and Case 3) results in relatively high phase difference (a significant faction of a radian) while the phase difference without visual sensory (Case 2 and Case 4) are small (except for COM in Case 2, which is characterized by a very high variance and a negative value.) Therefore, the young subjects with visual sensory aids show the most stable postural control with the highest positive phase difference. It is thought that younger persons use more of an anti-phase behavior in postural control to provide a timely equal and opposite force to counteract the body's sway. Elderly persons and those with balance problems are less able to counteract postural sway forces and therefore are more in-phase with the sway behavior. Postural control mechanisms are more stable with visual feedback because control mechanisms interact earlier to adjust the body before it deviates far from a state of equilibrium. The enhancement of postural control via visual sensory feedback, which manifests in itself an increased phase difference between COP_d and COM signals, is quite clear for both the young and elderly cases.

However, it is ambiguous to interpret the result for the young group under the closed eyes condition (Case 2) which shows small RMS displacement with a small phase difference. It is assumed that when visual feedback is absent, that the somatosensory and vestibular systems dominate [106]. With the control model from Figure 1 in mind, the experimental results suggests that when visual feedback is absent there is less available information about the state of posture therefore there is a greater need for frequent adjustments using feedback from the other two systems (vestibular and somatosensory systems). Vestibular control is optimal at 0.3 Hz while somatosensory control is in the higher ranges of 0.6Hz. Younger persons may alternate more between these two systems than elders because they have more information available. Elders (depending on age) have less reliable information from both systems

therefore may rely more on one system instead of alternating as much [103].

The values for time-frequency localized phase difference provide additional information to distinguish experimental conditions of aging and sensory systems on postural sway control. The existence of feedback control and its operational status are reflected in the both the time-frequency localized phase difference spectra and the corresponding phase difference values, all of which clearly indicate the status of the postural sway feedback control system. These demonstrated results have been made evident using the higher resolution possible with the cross time-frequency analysis techniques which enable one to reveal the time-frequency localized phase difference information for the paired transient postural sway signals such as COP_d and COM.

8.5 Conclusion

We applied time-frequency analysis to differentiate COP_d data and COM displacement data postural sway signals and to suggest a possible control model used by the postural control system. The differential COP data and COM displacement data are employed to investigate postural sway under different conditions of aging and visual systems. The time-localized average phase difference spectrum produced in our analysis distinguished the effects of both aging and visual sensory feedback on the stability of postural sway control. The investigation of the time-localized phase difference indicated that the visual sensory feedback could be likened to a lead compensator provided in Fig. 8.1 which stabilizes the transient damping in the postural sway. The experimental results for phase difference values revealed that the use of visual feedback dominates postural control more in the young participants than in the elderly participants. Therefore, the time-localized phase difference values

with corresponding frequencies of interests can be utilized to characterize the parameters of the posture controller in Fig. 8.1 for elderly/young and eyes open/closed conditions.

As shown and discussed in this chapter, the phase difference spectrum provides useful information about the postural control system in terms of stability. The analytical analysis of stability is not covered in this chapter, however, it is a potential extension of this work. For a given model of the postural control feedback system with knowledge of the gain characteristics in the frequency domain, the transient phase difference information obtained by cross time-frequency analysis can be utilized to ascertain the phase margin and thus assess the degree of stability. The application of the cross time-frequency analysis can be extended to other types of problems in biomedical engineering where time-localized phase difference information would prove helpful.

An attractive idea, within the paradigms of motor control, is the concept of identifying the level at which the postural control systems participate with control of the body during various sensory conditions. The results of this project indicate the frequency at which elders monitor posture (perhaps at a slower rate) is sometimes insufficient to correct posture when it deviates from equilibrium. The control model provides a possible systematic view of postural control indicating possible points of intervention for rehabilitation programs. Theoretical aspects of system comparison or system response to specific stimuli as suggested by the model could aid in understanding how clinical programs might augment aging postural control to delay the onset of decreased balance skills or functional frailty.

The use of the cross time-frequency analysis resulted in new time-frequency insights into the postural sway behavior. For this reason, it has great potential as a diagnostic clinical tool for balance assessments. Of course,

the caution for rehabilitation specialists is that if elders are already delayed in monitoring posture, when sensory systems are further altered by pathology, the elderly are even at greater risk of maintaining a stable postural control system. Perhaps if we further investigate the control of posture at this level of analysis using advanced time-frequency analysis we might also address the question as to whether we might be able to detect and perhaps modify deficits in postural monitoring by the elderly. Current methods rely primarily on subjective or observational clinical measurements of balance or postural control. These methods challenge clinicians in trying to document early deterioration of balance in high risk populations such as the frail elderly or during early stages a specific disease processes i.e., Alzheimer's disease, Parkinson's disease or even transient ischemic attacks or "mini-strokes". All continue as clinical challenges due sub-clinical changes with obscure changes in postural control. Better measurement of postural control would be helpful to assist in structuring rehabilitation programs or in providing modifications to a patient's environment to ensure safety during activities of daily living. In addition, a more sensitive measure of deteriorations in balance skills or responses to rehabilitative efforts could facilitate earlier implementation of preventive measures prior to traumatic falls.

Chapter 9

Conclusion

This dissertation is devoted to the development of a new theoretical scheme of signal processing, cross time-frequency analysis. The feasibility and applicability of the proposed theory have been verified by applications to various types of real-world signals and systems. The assessment and localization of transient disturbances in electric power systems have been investigated by use of classical and cross time-frequency analysis.

In this dissertation, a new definition of cross time-frequency distribution and its properties are investigated. Compared with the traditional Cohen's class, the cross time-frequency distribution enables one to consider phase difference information for a pair of signals. In addition, the properties of the cross time-frequency distribution and corresponding kernel requirements are compared with the traditional Cohen's class. The relation between Cohen's distributions and cross time-frequency distributions is clarified by modification of Moyal's formula. Based on numerical simulations, the cross time-frequency phase spectrum provides a more robust estimate of the phase difference than classical cross power spectral analysis, under transient conditions.

Based on the time-frequency distribution of a transient disturbance, a set of time-frequency based power quality indices are developed; the instantaneous disturbance energy ratio, normalized instantaneous disturbance energy ratio, instantaneous frequency, and instantaneous K-factor are suggested for

transient power quality assessment. The limitations of the traditional Fourier series coefficient based power quality indices, which inherently require periodicity of the disturbance signal, has been resolved by use of time-frequency analysis. Also, interharmonic disturbances are investigated by use of time-frequency based power quality indices.

As an application of cross time-frequency analysis to power systems, an analytic solution to locate transient capacitor switching disturbance has been discussed. The flow of transient disturbance energy caused by the capacitor switching is determined by the time and frequency localized phase difference. The cross time-frequency analysis provides time and frequency localized phase difference between transient voltage and current which determine the direction of transient disturbance flow. The time and frequency localization properties of the proposed scheme allows one to expand the application to complicated power distribution systems without knowledge of system parameters, capacitor size and configuration. In this dissertation, the discussion and application of the the time-frequency based solution for the direction of the transient disturbance energy flow is limited to the capacitor switching events only; however, the localization of the other types of transient disturbances in power distribution systems and faults in power transmission systems deserves to be investigated by the proposed methodology.

In this dissertation, a practical and systematic procedure for determining the optimal wavelet basis has been investigated by employing the concept of an instantaneous SNR (i.e., a transient resolution index (dB/sec)) under the constraint of the uncertainty principle. Two parameter values (i.e., time duration T and frequency bandwidth F) are estimated along with their product (i.e., TF product) from the local properties of a wavelet basis and a voltage sag signal, and, then, a transient resolution index (dB/sec), named the "instan-

taneous SNR", is proposed to quantitatively measure the degree of similarity and mismatch between the signal and the wavelet basis within the time frame of the basis function. For a typical case of voltage sag, the optimal Daubechies wavelet basis turns out to be Daubechies 4, although Daubechies 5 will work almost as well. This algorithm is not restricted to voltage sag detection cases and Daubechies' wavelet basis, i.e., it may be applied to other transient disturbances and other wavelet bases.

In this dissertation, a new high-resolution reflectometry technique has been proposed. which operates simultaneously in both the time and frequency domains. The approach rests upon time-frequency signal analysis and utilizes a chirp signal multiplied by a Gaussian time envelope. The Gaussian envelope provides time localization, while the chirp allows one to excite the system under test with a swept sinusoid covering a frequency band of interest. Sensitivity in detecting the reflected signal is provided by a time-frequency cross correlation function. The use of time-frequency cross correlation function of the respective time-frequency distributions of the reference and reflected signals has proven to be a sensitive detector of weak reflected signals in RG 142 and RG 400 coaxial cables. The experimental work involving two types of coaxial cable, three types of faults, and four fault lengths, indicates that the new time-frequency domain reflectometry locates faults with an accuracy comparable to TDR.

The feasibility of cross time-frequency distributions has been investigated in order to measure time-localized phase and group velocities given wave elevation time series measured at two points spatially separated in the direction of wave propagation. The cross time-frequency analysis and its time-frequency phase difference spectrum has been utilized for the measurement of the localized phase difference spectrum. The results based on the cross time-frequency

186

analysis are compared to those obtained experimentally from classical Fourier-based cross-power spectra, which of course provide no time localization, and to theoretical estimates of phase and group velocity. It is found that the weighted average of the local phase and group velocities closely collapse to those measured using classical Fourier-based methods and those predicted by ocean wave theory.

The effects of visual feedback and aging on postural sway systems and signals can be investigated by analyzing the transient phase difference between "input" and "output" which correspond to center of pressure (COP) and center of mass (COM), respectively. The feedback control process in the postural sway is interpreted in terms of a feedback compensator which is characterized in terms of a phase difference. Using the experimental results of the transient phase difference obtained from the cross time-frequency distribution, it is demonstrated that the postural control of young persons are more stable and rely more on visual sensory feedback to stabilize postural control compared to that of the elderly persons.

In the future, a set of customized power quality indices can be developed for the power quality assessment of SiC based next-generation power electronic devices. Also, the joint time-frequency domain reflectometry offers much promise as a new wire and cable diagnostic tool, especially in the communications and power engineering area.

The theory and applications of cross time-frequency analysis presented in this dissertation are expected to be useful for the analysis of the nonstationary signals and physical systems.

Bibliography

[1] L. Cohen, "Time-frequency distributions - a review," *Proceedings of IEEE*, vol. 77, pp. 941–981, 1989.

[2] ——, *Time-Frequency Signal Analysis.* Prentice Hall, 1995.

[3] W. J. Williams, "Uncertainty, information, and time-frequency distributions," in *Advanced Signal Processing Algorithms, Architectures and Implementations II, SPIE.*, vol. 1566, 1991, pp. 144–156.

[4] P. Flandrin, *Time-Frequency/ Time-Scale Analysis.* Academic Press, 1998.

[5] H. I. Choi and W. J. Williams, "Improved time-frequency representation of multicomponent signals using exponential kernels," *IEEE Transactions on Acoustics, Speech and Signal Processing*, vol. 37, pp. 862–871, 1989.

[6] J. Jeong and W. Williams, "Kernel design for reduced interference distributions," *IEEE Transactions on Signal Processing*, vol. 40, pp. 402–412, 1992.

[7] G. Cunnuningham, "Analysis, synthesis and implementation of time-frequency distributions using spectrogram decomposition," Ph.D. dissertation, The University of Michigan, Ann Arbor, 1992.

[8] W. Williams, "Cross Hilbert time-frequency distribution," in *Advanced Signal Processing Algorithms, Architectures and Implementations VIII, SPIE.*, vol. 3461, 1998, pp. 120–129.

[9] P. Flandrin, R. Baraniuk, and O. Michel, "Time-frequency complexity and information," in *IEEE Proceedings of ICASSP*, Adelaide, Australia, May 1994.

[10] L. White and B. Boashash, "Cross spectral analysis of nonstationary processes," *IEEE Transactions on Information Theory*, vol. 36, pp. 830–835, July 1990.

[11] B. Boashash and P. O'Shea, "Use of the cross Wigner-Ville distribution for estimation of instantaneous frequency," *IEEE Transactions on Signal Processing*, vol. 41, pp. 1439–1445, Mar. 1993.

[12] W. Mecklenbrauker, *The Wigner distribution: theory and applications in signal processing.* Elsevier, 1997.

[13] J. Jeong and W. Williams, "Mechanism of the cross-terms in spectrograms," *IEEE Transactions on Signal Processing*, vol. 40, pp. 2608–2613, Oct. 1992.

[14] W. J. Williams, "Reduced interference distributions: biological applications and interpretations," *Proceedings of the IEEE*, vol. 84, no. 9, pp. 1264–1280, Sept. 1996.

[15] P. Loughlin, J. Pitton, and L. E. Atlas, "Bilinear time-frequency representations: new insights and properties," *IEEE Transactions on Signal Processing*, vol. 41, pp. 750–767, 1993.

[16] L. Cohen, "Quantization problem and variational principle in the phase space formulation of quantum mechanics," *Jour. Math. Phys*, vol. 17, pp. 1863–1866, 1976.

[17] J. Arrillaga, M. Bollen, and N. Watson, "Power quality following deregulation," in *Proceedings of IEEE*, vol. 88, no. 2, Feb. 2000.

[18] G. T. Heydt, "Power quality engineering," pp. 5–7, Sept. 2001.

[19] R. Dugan, M. McGrannaghan, S. Santoso, and H. Beaty, *Electrical Power Systems Quality*. McGraw-Hill, 2002.

[20] "ITIC curve application note," Information Technology Industry Counsil.

[21] "IEEE 519," IEEE Recommended Practices and Requirements for Harmonic Control in Power Systems (ANSI), 1992.

[22] G. T. Heydt and W. T. Jewell, "Pitfalls of electric power quality indices," *IEEE Transactions on Power Delivery*, vol. 13, no. 2, pp. 570–578, Apr. 1998.

[23] R. Thallam and G. Heydt, "Power acceptability and voltage sag indices in the three phase sense," in *IEEE Power Engineering Society Summer Meeting*, vol. 2, 2000, pp. 905–910.

[24] A. M. Gaouda, M. Salama, M. R. Sultan, and A. Y. Chikhani, "Application of multiresolution signal decomposition for monitoring short-duration variations in distribution systems," *IEEE Transactions on Power Delivery*, vol. 15, no. 2, pp. 478–485, 2000.

[25] O. Poisson, P. Rioual, and M. Meunier, "Detection and measurement of power quality disturbances using wavelet transform," *IEEE Transactions on Power Delivery*, vol. 15, no. 3, pp. 1039–1044, 2000.

[26] C. Parameswariah and M. Cox, "Frequency characteristics of wavelets," *IEEE Transactions on Power Delivery*, vol. 17, no. 3, pp. 800–804, 2000.

[27] G. T. Heydt and A. W. Galli, "Transient power quality problems analyzed using wavelet," *IEEE Transactions on Power Delivery*, vol. 12, no. 2, pp. 908–915, 1997.

[28] S. Santoso, E. J. Powers, W. M. Grady, and P. Hofmann, "Power quality assessment via wavelet transform analysis," *IEEE Transactions on Power Delivery*, vol. 11, pp. 924–930, 1996.

[29] S. Santoso, E. J. Powers, W. M. Grady, J. Lamoree, and S. C. Bhatt, "Characterization of distribution power quality events with Fourier and wavelet transforms," *IEEE Transactions on Power Delivery*, vol. 15, pp. 247–253, 2000.

[30] G. Heydt, P. Fjeld, C. Liu, D. Pierce, L. Tu, and G.Hensley, "Applications of the windowed FFT to electric power quality assessment," *IEEE Transactions on Power Delivery*, vol. 14, no. 4, pp. 1411–1416, 1999.

[31] S. Herraiz, G. Heydt, and E. O'Neill-Carrillo, "Power quality indices for aperiodic voltages and currents," *IEEE Transactions on Power Delivery*, vol. 15, no. 2, pp. 784–790, 2000.

[32] A. Mariscotti, "Discussion on "Power quality indices for aperiodic voltage and currents"," *IEEE Transactions on Power Delivery*, vol. 15, no. 4, pp. 1333–1334, 2000.

191

[33] S. H. Jaramillo, G. T. Heydt, and E. ONeill-Carrillo, "Closure to discussion of "Power quality indices for aperiodic voltage and currents"," *IEEE Transactions on Power Delivery*, vol. 15, no. 4, pp. 1334–1334, 2000.

[34] Y. Shin, C. P. Antony, E. J. Powers, and W. Grady, "Time-frequency analysis of power system fault signals for power quality," in *Proceedings of IEEE Power Engineering Society Summer Meeting*, Edmonton, Alberta, Canada, 1999, pp. 402–407.

[35] E. J. Powers, Y. Shin, and W. M. Grady, "Time-frequency analysis of electric power disturbances," in *Time-Frequency Signal Analysis and Processing: a Comprehensive Reference*, B. Boashash, Ed. Oxford, UK: Elsevier, 2003, ch. 15.1, pp. 628–634.

[36] M. McGranaghan, R. Zavadil, G. Hensley, T. Singh, and M. Samotyj, "Impact of utility switched capacitors on customer systems-magnification at low voltage capacitors," *IEEE Transactions on Power Delivery*, vol. 7, no. 2, pp. 862–868, 1992.

[37] D. Sochuliakova, D. Niebur, C. O. Nwankpa, R. Fischl, and D. Richardson, "Identification of capacitor position in a radial system," *IEEE Transactions on Power Delivery*, vol. 14, no. 4, pp. 1368–1373, 1999.

[38] A. Parsons, W. Grady, E. Powers, and J. Soward, "A direction finder for power quality disturbances based upon disturbance power and energy," *IEEE Transactions on Power Delivery*, vol. 15, no. 3, pp. 1081–1086, 2000.

[39] S. Santoso, J. Lamoree, and M. F. McGranaghan, "Signature analysis to track capacitor switching performance," in *Proceedings of the IEEE/PES Transmission and Distribution Conference and Exposition*, vol. 1, no. 6, Oct. 2001, pp. 259–263.

[40] J. Kim, W. Grady, A. Arapostathis, J. C. Soward, and S. C. Bhatt, "A time-domain procedure for locating switched capacitors in power distribution systems," *IEEE Transactions on Power Delivery*, vol. 17, no. 4, pp. 1044–1049, 2002.

[41] Y. Shin, E. Powers, and W. Grady, "On cross time-frequency distribution function," in *Advanced Signal Processing Algorithms, Architectures and Implementations VIII, SPIE*, vol. 4116, 2000, pp. 9–16.

[42] J. Arrillaga, M. Bollen, and N. Watson, "Power quality following deregulation," *Proceedings of the IEEE*, vol. 88, no. 2, pp. 246–261, 2000.

[43] H.-S. Song and K. Nam, "Instantaneous phase-angle estimation algorithm under unbalanced voltage-sag conditions," in *IEE Proceedings: Generation, Transmission and Distribution*, vol. 147, no. 6, Nov. 2000, pp. 409–415.

[44] J. de Carvalho, H. Arango, J. de Abreu, and J. Noronha, "Electric power system under voltage sag - a tool for achieving compatibility," in *Proc. of 9th Int. Conf. on Harmonics and Quality of Power*, vol. 3, 2000, pp. 784–789.

[45] S. Santoso, E. Powers, W. Grady, and A. Parsons, "Power quality disturbance waveform recognition using wavelet-based neural classifier. I.

Theoretical foundation," *IEEE Transactions on Power Delivery*, vol. 15, no. 1, pp. 222–228, 2000.

[46] ——, "Power quality disturbance waveform recognition using wavelet-based neural classifier. II. Application," *IEEE Transactions on Power Delivery*, vol. 15, no. 1, pp. 229–235, 2000.

[47] B. Boashash, *Time-Frequency Signal Analysis.* Melborne: Longman Cheshire/ Wiley-Halstead, 1992.

[48] P. Flandlin, "Time-frequency toolbox manual." [Online]. Available: http://iut-saint-nazaire.univ-nantes.fr/~auger/tftb.html

[49] G. Heydt, *Electrical Power Quality.* West Lafayette, IN: Stars in a Circle, 1991.

[50] R. R. Coifman and M. V. Wickerhauser, "Entropy-based algorithms for best basis selection," *IEEE Transactions on Information Theory*, vol. 38, pp. 713–718, 1992.

[51] P. J. Green, "Radar astronomy measurement techniques," MIT Lincoln Laboratory, Lexington, MA., Tech. Rep. 282, Dec. 1962.

[52] C. Furse and R. Haupt, "Down to the wire: The hidden hazard of aging aircraft wiring," *IEEE Spectrum*, pp. 35–39, Feb. 2001.

[53] National Science and Technology Council Committee on Technology, Wire System Safety Interagency Working Group, "Review of federal programs for wire system safety-final report," National Science and Technology Council Committee on Technology, Nov. 2000.

[54] C. P. Nemarich, "Time domain reflectometry liquid level sensors," IEEE Instrumentation and Measurement Magazine, pp. 40–44, Dec. 2001.

[55] M. Yoshida, K. Nakamura, and H. Ito, "A new method for measurement of group velocity dispersion of optical fibers by using a frequency-shifted feedback fiber laser," *IEEE Photonics Technology Letters*, vol. 13, no. 3, pp. 227–229, 2001.

[56] N. Kamdor and C. Furse, "An inexpensive distance measuring system for location of robotic vehicles," in *Antennas and Propagation Society, 1999. IEEE International Symposium 1999*, vol. 3, 1999, pp. 1498–1501.

[57] H. Packard, "Time domain reflectometry," Hewlett Packard, 1998.

[58] "Application guide," Riser Bond, Inc. [Online]. Available: http://www.riserbond.com/assets/downloads/Appguide.pdf

[59] H. Yamada, M. Ohmiya, Y. Ogawa, and K. Itoh, "Superresolution techniques for time-domain measurements with a network analyzer," *IEEE Transactions on Antennas and Propagation*, vol. 39, no. 2, pp. 177–183, Feb. 1991.

[60] N. G. Paulter, "An assessment on the accuracy of time-domain reflectometry for meausring the characteristic impedance of transmission line," *IEEE Transactions on Instrumentation and Measurement*, vol. 50, no. 5, pp. 1381–1388, Oct. 2001.

[61] "Agilent technologies impedance measurement handbook, 2nd edition," Agilent Technologies Co. Ltd., 2002.

[62] W. Kim, M. Swaminathan, and Y. Li, "Extraction of the frequency-dependent characteristic impedance of transmission lines using TDR measurements," in *IEEE Proceedings of Electronics Packaging Technology Conference*, 2000, pp. 191–197.

[63] H. Zhu, J. Allen R. Hefner, and J.-S. J. Lai, "Characterization of power electronics system interconnect parasitics using time domain reflectometry," *IEEE Transactions on Power Electronics*, vol. 14, no. 5, pp. 622–628, July 1999.

[64] K. Park and J. Park, "Time-to-digital converter of very high pulse stretching ratio for digital storage oscilloscopes," *Review of Scientific Instruments*, vol. 70, no. 2, pp. 1568–1574, Feb. 1999.

[65] V. Biesen, "High accuracy location of faults on electrical lines using digital signal processing," *IEEE Transactions on Instrumentation and Measurement*, vol. 39, no. 1, pp. 175–179, Feb. 1990.

[66] H. Vanhamme, "High resolution frequency-domain reflectometry," *IEEE Transactions on Instrumentation and Measurement*, vol. 39, no. 2, pp. 369–375, Apr. 1990.

[67] D. Agrez, "Approximation of the skin effect to improve cable-fault location by TDR," in *Proceedings of IEEE Instrumentation and Measurement Conference*, May 2003, pp. 50–53.

[68] L. Cohen, "Pulse propagation in dispersive media," in *Proceedings of the Tenth IEEE Workshop Statistical Signal and Array Processing*, 2000, pp. 485–489.

196

[69] J. Beall, Y. Kim, and E. Powers, "Estimation of wavenumber and frequency spectra using fixed probe pairs," *Journal of Applied Physics*, vol. 53, pp. 3933–3940, 1988.

[70] A. Bers., "Note on group velocity and energy propagation," *American Journal of Physics*, vol. 68, no. 5, p. 482, May 2000.

[71] B. Ferguson and K. Lo, "Transiting aircraft parameter estimation using underwater acoustic sensor data," *IEEE Journal of Oceanic Engineering*, vol. 24, no. 4, pp. 424–435, Oct. 1999.

[72] H.-Y. Chen and I.-T. Lu, "Localization of a broadband source using a matched-mode procedure in the time-frequency domain," *IEEE Journal of Oceanic Engineering*, vol. 19, no. 2, pp. 166–174, Apr. 1994.

[73] S. Chandran and M. Ibrahim, "DOA estimation of wide-band signals based on time-frequency analysis," *IEEE Journal of Oceanic Engineering*, vol. 24, no. 1, pp. 116–121, Jan. 1999.

[74] B. Ferguson, "Time-frequency signal analysis of hydrophone data," *IEEE Journal of Oceanic Engineering*, vol. 21, no. 4, pp. 537–544, Oct. 1996.

[75] R. Imai, Y. Hashimoto, K. Kikuchi, and S. Fujii, "High-resolution beamforming by the Wigner-Ville distribution method," *IEEE Journal of Oceanic Engineering*, vol. 25, no. 1, pp. 105–110, 2000.

[76] P. Delfyett, G. H. Shi, I. Nitta, , J. C. Connolly, and G. Alphonse, "Joint time-frequency measurements of modelocked semiconductor diode lasers and dynamics using frequency-resolved optical gating," *IEEE Journal of Quantum Electronics*, vol. 15, no. 4, pp. 487–500, Apr. 1999.

[77] H. Jeoung and Y.-S. Jang, "Fracture source location in thin plates using the wavelet transform of dispersive waves," *IEEE Transactions on Ultrasonics, Ferroelectrics and Frequency Control*, vol. 47, no. 3, pp. 612–619, May 2000.

[78] A. Quinquis and D. Boulinguez, "Multipath channel identification with wavelet packets," *IEEE Journal of Oceanic Engineering*, vol. 22, no. 2, pp. 342–346, Apr. 1997.

[79] A. Liu, C. Y. Peng, and S. Y. Chang, "Wavelet analysis of satellite images for coastal watch," *IEEE Journal of Oceanic Engineering*, vol. 22, no. 1, pp. 9–17, Jan. 1997.

[80] D. F. Hoag, V. K. Ingle, and R. J. Gaudette, "Low-bit-rate coding of underwater video using wavelet-based compression algorithms," *IEEE Journal of Oceanic Engineering*, vol. 22, no. 2, pp. 393–400, Apr. 1997.

[81] A. Abbate, J. Frankel, and P. Das, "Wavelet transform signal processing for dispersion analysis of ultrasonic signals," in *IEEE Proceedings of Ultrasonics Symposium*, vol. 1, 1995, pp. 751–755.

[82] Y. Shin, A. Chao, and E. J. Powers, "Time-frequency analysis of dispersive wave phenomena," in *Proceedings of The Tenth (2000) International Offshore and Polar Engineering*, vol. 3, 2000, pp. 38–42.

[83] Staelin, Morgenthaler, and Kong, *Electromagnetic Waves*. Eaglewood Cliffs, New Jersey: Prentice-Hall, 1989.

[84] Proakis and Manolakis, *Digital Signal Processing-Principles, Algorithms, and Applications*. Prentice Hall, 1996.

[85] McCormick, *Ocean Engineering Wave Mechanics.* John Wiley & Sons, 1973.

[86] Main, *Vibrations and Waves in Physics.* Cambridge University Press., 1993.

[87] L. Gilchrist, "Age-related changes in the ability to side step during gait," *Clinical Biomechanics*, vol. 132, pp. 91–97, 1998.

[88] B. Maki, P. Holliday, and A. Topper, "A prospective study of postural balance and risk of falling in an ambulatory and independent elderly population," *Journal of Gerontology. Medical Sciences*, vol. 49, pp. 72–84, 1994.

[89] D. Rice, "Cost of injury in the US: A report to congress," Institute for Health and Aging, University of California and Johns Hopkins University, San Francisco, CA, Tech. Rep., 1989.

[90] B. Myklebust, J. Myklebust, and T. Prieto, "Characterization and modeling of postural steadiness in the elderly: a review," *IEEE Transactions on Rehabilitation Engineering*, vol. 1, pp. 26–34, 1993.

[91] M. Akesson, R. Johansson, and M. Magnusson, "Identification of human postural dynamics," *IEEE Transactions on Biomedical Engineering*, vol. 35, pp. 858–869, 1988.

[92] A. Sabatini, "A statistical mechanical analysis of postural sway using non-Gaussian FARIMA stochastic models," *IEEE Transactions on Biomedical Engineering*, vol. 47, pp. 1219–1227, 2000.

[93] D. Gobert, "Multivariate analysis of frontal plane postural sway: postural coordination as modified by sensory condition and aging," Ph.D. dissertation, The University of Texas at Austin, Austin, TX, U.S.A., 2000.

[94] P. Loughlin and M. Redfern, "Spectral characteristics of visually induced postural sway in healthy elderly and healthy young subjects," *IEEE Transactions on Neural Systems and Rehabilitation Engineering*, vol. 9, pp. 24–30, 2001.

[95] L. Chaparro, A. El-Jaroudi, J. Furman, P. Loughlin, and T. S. M. Redfern, "Time-frequency analysis of postural sway," in *Conference Record of the Twenty-Eighth Asilomar Conference on Signals, Systems and Computers*, vol. 1, 1994, pp. 378–382.

[96] J. Furman, P. Loughlin, and M. Redfern, "Time-varying characteristics of visually induced postural sway," *IEEE Transactions on Neural Systems and Rehabilitation*, vol. 4, pp. 416–424, 1996.

[97] L. Nashner, "A model describing vestibular detection of body sway motion," *Acta Otolaryngoloy*, vol. 72, pp. 429–436, 1971.

[98] R. Fitzpatrick, D. Burke, and S. Gandevia, "Loop gain of reflexes controlling human standing measured with the use of postural and vestibular disturbances," *Journal of Neurophysiology*, vol. 76, pp. 3994–4008, 1996.

[99] Y. Fukuoka, S. Imai, and A. Ishida, "Analysis of the posture control system under fixed and sway-referenced support conditions," *IEEE Transactions on Biomedical Engineering*, vol. 44, pp. 331–336, 1997.

[100] A. Oppenheim, A. Willsky, H. Nawad, and S. Hamid, *Signals and Systems*. Prentice-Hall, Aug. 1996.

[101] B. Kuo and F. Golnaraghi, *Automatic Control Systems, 8th Edition*. Wiley, John & Sons, Sept. 2002.

[102] J. Collins and C. D. Luca, "Open-loop and closed-loop control of posture: a random-walk analysis of center-of-pressure trajectories," *Experimental Brain Research*, vol. 95, pp. 308–318, 1993.

[103] ——, "Age-related changes in open-loop and closed-loop postural control mechanisms," *Experimental Brain Research*, vol. 104, pp. 480–492, 1995.

[104] D. Winter, A. Patla, M. Ishac, and W. Gage, "Motor mechanisms of balance during quiet standing," *Journal of Electromyography and Kinesiology*, pp. 49–56, Feb. 2003.

[105] W. J. Williams, "Reduced interference distributions:biological applications and interpretations," in *Proceedings of the IEEE*, vol. 84, 1996, pp. 1264–1280.

[106] J. Collins and C. D. Luca, "The effects of visual input on open-loop and closed-loop postural control mechanisms," *Experimental Brain Research*, vol. 103, pp. 151–163, 1995.

Vita

Yong June Shin was born in Seoul, Korea on 29 May 1973, the son of Hong-Kyou Shin and Jung-Ae Park. He is graduated from the Seoul Science High School in 1992. He received the Bachelor of Science degree from Yonsei University, Seoul, Korea in 1996 with early completion honors and the Master of Science degree from the Department of Electrical Engineering and Computer Science, The University of Michigan, Ann Arbor in 1997 under the supervision of Professor W. J. Williams. He was accepted and started doctoral studies in the Department of Electrical and Computer Engineering under supervision of Professors E. J Powers and W. Mack Grady at The University of Texas at Austin in January 1998. From May 2001 to January 2003, he took a leave of absence to fulfill the military service obligation in Republic of Korea. Upon graduation, he will join the Department of Electrical Engineering, The University of South Carolina, Columbia, SC as an assistant professor.

Permanent address: Dae-Gyo Apartment #201, Youido-dong,
Youngdeungpo-gu, Seoul, Korea, 150-010

This dissertation was typeset with LaTeX† by the author.

---

†LaTeX is a document preparation system developed by Leslie Lamport as a special version of Donald Knuth's TeX Program.